

Bangor University

DOCTOR OF PHILOSOPHY

Devices and techniques for the dielectrophoretic characterisation and manipulation of cells

MENACHERY, ANOOP

Award date:
2009

Awarding institution:
Bangor University

[Link to publication](#)

General rights

Copyright and moral rights for the publications made accessible in the public portal are retained by the authors and/or other copyright owners and it is a condition of accessing publications that users recognise and abide by the legal requirements associated with these rights.

- Users may download and print one copy of any publication from the public portal for the purpose of private study or research.
- You may not further distribute the material or use it for any profit-making activity or commercial gain
- You may freely distribute the URL identifying the publication in the public portal ?

Take down policy

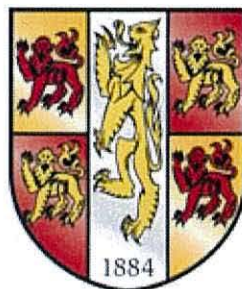
If you believe that this document breaches copyright please contact us providing details, and we will remove access to the work immediately and investigate your claim.

**DEVICES AND TECHNIQUES FOR THE
DIELECTROPHORETIC CHARACTERISATION AND
MANIPULATION OF CELLS**

BY ANOOP MENACHERY

**A thesis submitted in candidature for the degree of
DOCTOR OF PHILOSOPHY
IN
ELECTRONIC ENGINEERING**

PRIFYSGOL
BANGOR
UNIVERSITY



2009



Abstract

The main objectives of this work were to develop efficient Dielectrophoresis (DEP) processes for utilization in the biological realm. The work presented in this thesis concerns the refinement and development of integrated microfluidic and microelectrode technologies with design parameter optimization carried out using the assistance of finite element simulations.

A detailed examination of cell membrane rupture during DEP experiments has been carried out to study the influence of AC Electric field parameters on cell destruction. Detailed analysis is provided on how the stresses induced across the membrane by strong electric fields, lead to the rupture of the plasma membrane.

The use of DEP for the separation of Small Cell Lung Cancer (SCLC) cell phenotypic variants has also been demonstrated. Cell phenotypes with subtle differences in membrane morphology were successfully sorted using DEP processes.

To address the need to separate individual cells of interest, work to design and develop DEP tweezers was undertaken. A cell over expressing a protein of interest that was tagged with a green fluorescent protein (GFP) was isolated for the purpose of establishing a stable cell line.

The final part of the work optimizes a 3D DEP electrode system for engineering three dimensional cell constructs, to better understand the effects of cell-cell interactions and intercellular transport events. Using the 3D DEP electrode system, suspensions of BETA-TC-6 and INS-1 cells were condensed into three-dimensional cell constructs of roughly the same size and cell density as insulin secreting pancreatic structures known as the islet of Langerhans.

Acknowledgements

My most sincere gratitude to my Mother, Father and Sister for the encouragement and support provided every minute of every day for all these years.

A special debt of gratitude to my supervisor Prof. Ronald Pethig for introducing me to this fascinating research area and for providing me with a healthy combination of freedom, inspiration, direction, support and encouragement during the last 4 years.

I have benefitted from useful discussions and encouragement provided by Dr. Julian Burt.

Special thanks go to Dr. Peter Smith for the hospitality, strong support and supervision during my stay at the MBL.

Special thanks go to Prof. Paul Smith and Dr. Rachel Errington for the hospitality, strong support and supervision during my work at Cardiff University.

I have benefited from the support of Dr. Andrew Goater, Mrs. Sally Chapell, Mr. John Cambridge, Dr. Nadeem Rizvi, Mr. Rob Lewis, Dr. Leon Collis, Dr. Mark Messerli, Dr. Shanta Messerli, Prof. Martin Taylor, Mr. Louis Kerr, Dr. Emma Heart and Dr. Paul Sayers.

Very special thanks to all my friends for tolerating me and providing a shoulder of support and care through good and bad times.

Finally, I would like to acknowledge the School of Electronic Engineering and the MBL for providing me with financial support.

Contents

1 Introduction

1.1 Conventional Laboratory systems vs. Lab-on-chip Systems	1
1.2 Manipulation Methods	3
1.2.1 Magnetic Manipulation	4
1.2.2 Acoustic Manipulation	4
1.2.3 Fluidic Manipulation	5
1.2.4 Electrical Manipulation	5
1.2.4.1 Electrophoresis	5
1.2.4.2 Electroosmosis	5
1.2.4.3 Dielectrophoresis (DEP)	6
1.3 Dielectric Spectroscopy	7
1.3.1 Impedance Measurements	8
1.3.2 DEP Spectroscopy	8
1.3.3 Electrorotation	8
1.4 Thesis Format and Content	9
1.5 References	11

2 Theory

2.1 Dielectrics in Electric Fields	14
2.2 Force on an Infinitesimal Dipole and Effective Dipole Moment of a Sphere	16
2.2.1 DEP Force in an AC Field	19
2.2.2 Electrorotation	22
2.3 Multi shelled model	22
2.4 Dipolar Interactions and Chaining in Cell suspensions Undergoing DEP	27
2.5 Fluid Flow in Microchannels	31
2.5.1 Navier-Stokes Equation	31
2.5.2 Fluid Effect on a Moving Particle	33
2.6 Surface Tension Effects	34
2.7 AC Electrokinetic Fluid Effects	35
2.7.1 Electrothermal Heating Leading to Fluid Flow	35
2.7.2 AC Electroosmosis	36
2.8 Finite Element Analysis	37

2.9 References	44
----------------------	----

3 Controlling Cell Destruction using Dielectrophoretic Forces

3.1 Introduction	46
3.2 Theory	48
3.3 Experimental	51
3.3.1 Cell Samples	51
3.3.2 Cell Bursting Observations and Electric Field Simulations	51
3.4 Results	55
3.5 Discussions and Conclusions	58
3.6 References	62

4 Dielectrophoretic characterization and separation of metastatic variants of small cell lung cancer cells

4.1 Introduction	64
4.2 Theory	66
4.3 Experimental	68
4.3.1 Cell Preparation	68
4.3.2 Devices and Methods	68
4.4 Results and Discussion	71
4.4.1 Simulations	71
4.4.2 DEP Experiments	72
4.5 Conclusion	78
4.6 References	79

5 Fabrication and Testing of Dielectrophoretic Tweezers

5.1 Introduction	80
5.2 Experimental Design and Methods	85
5.3 Results and Discussion	89
5.3.1 Simulation	89
5.3.2 Experimental	93
5.4 Conclusion	98
5.5 References	100

6 Assembly of 3-D Cell Structures using Dielectrophoresis

6.1 Introduction.....	102
6.2 Simulations.....	105
6.3 Devices and Methods	111
6.3.1 Device Manufacture.....	111
6.3.2 Cell Preparation.....	112
6.3.3 Nanosensor Preparation.....	113
6.3.3.1 PEBBLEs Preparation.....	113
6.3.3.2 Functionalised Silica Nanoparticles.....	114
6.4 Results and Discussion	115
6. 5 Conclusions.....	125
6.6 References.....	128

7 Conclusions and Future Work..... 131

7.1 Conclusions.....	131
7.2 Future Work.....	133

List of Publications 135

Chapter 1

Introduction

The work reported in this thesis concerns the application of dielectrophoresis (DEP), for characterising and manipulating biological cells. The hope is that such work can lead to useful applications in the biomedical sciences. The experiments were performed on devices that contained small volumes (20~200 microlitres) of cell suspensions in fluidic channels and/or chambers. AC electrical fields were imposed on these samples using microfabricated electrodes. These devices can be considered to fall under the general category of lab-on-chip systems.

1.1 Conventional Laboratory Systems vs. Lab-on-chip Systems

Handling and testing of biological specimens in a medical laboratory requires large and expensive testing instruments that are not easily available to every laboratory. In most cases the biological samples are collected and transported from the collection point to analysis centres and this leads to a delay in diagnosis. Large sample volumes are required in a medical laboratory using conventional apparatus and hence miniaturization of biological apparatus reduces sample volumes and reagents to microlitres, and also, the ability to process and analyse the samples on site offers a distinct advantage of reduced processing time.

These distinct advantages led to the interest and development of Lab-on-chip systems which integrate microfluidic systems with several laboratory processes scaled down to the chip format. Lab-on-chip has risen to be the interests of many because of technologies such as microfluidics, integrated electronics and micromechanics. Many of the fabrication methods used for the development of lab-on-chip systems arose from the microelectronics industry. The primary method, namely photolithography, which is

still used in the microelectronics industry, was applied to build microstructures such as microfluidic channels and microactuators. Using this method, it allows the transfer of a pattern from a mask to a photoresist using radiation such as UV radiation. The various other factors which have contributed to its development include the development of new materials and better imaging techniques. One of the major breakthroughs in microstructure related material sciences, was, the development of a highly versatile polymer called polydimethylsiloxane (PDMS) [1]. This made the fabrication of microfluidic components extremely affordable and its unique properties such as optical transparency, chemical inertness and gas permeability makes it a very attractive candidate for working with biological materials.

Miniaturization of standard chemical and biological lab-on-chip procedures takes advantage of physics at the microscale. For example, scaling down chemical reactions leads to increased reaction rates because of increased surface to volume ratio. Thermal processes like heating/cooling is also speeded up, thereby enabling efficient DNA amplification by polymerase chain reaction. STMicroelectronics has exploited this technology to produce a chip that incorporates microfluidic handling, a miniaturized PCR reactor and a custom microarray. This company claims a 100% yield and a speed of operation 3-times faster than conventional thermocyclers. Micronit offers several microreactor chips for chemical synthesis which reduces reagent consumption and ensures efficient mass and heat-transfer. Caliper Life Sciences exploits the use of microfluidics technology for eletrophoretic separations of nucleic acids and proteins. Translume has developed a microfluidic soot detection system for lubricating oils, enabling the real-time, on-line monitoring of oil characteristics at one site. Other lab-on-chip devices which are being used commercially are glucose monitoring devices. SILOAM biosciences manufacture a point of care metabolic monitoring device which includes a direct venous blood sampling capability.

Protein kits incorporating lab-on-chip technology have been developed by Agilent technologies for analyzing cell lysates and antibodies. Other lab-on-chip testing capabilities includes monitoring of pH, blood salts and dissolved gases.

1.2 Manipulation Methods

A fundamental issue of any chemical or biological analysis is the sample preparation which includes the separation of components into homogeneous fractions. In the case of biological analysis it is important to be able to obtain a homogeneous population of cells from a mixture. Some of the numerous applications for effective cell sorting are mentioned below:

- 1) In the Food and Water industry it is critical to monitor bacterial activity and this is only possible with effective detection and isolation of bacteria.
- 2) Capture of stem cells from peripheral blood, bone marrow or tissue requires the ability to isolate these rare cell types from a mixture of numerous other cells.
- 3) Early diagnosis of cancer such as leukemia requires effective isolation and detection of cancerous cells. A major challenge in the detection of leukemia is that there are only 10 cancerous cells among 5×10^9 cells in 1 ml of blood and therefore a highly selective method is required.

The focus on effective cell manipulation is also driven by the need to be able to precisely control their position and layout for purposes such as tissue engineering. There is a wide variety of manipulation methods based on different components that need to be sorted, like DNA, proteins, microbes and cells.

Some of the lab-on-chip methods utilized for cell manipulation are listed below

1.2.1 Magnetic Manipulation

The use of Magnetic fields is considered to be a competent method for cell sorting. For biological cell separation two methods are normally used. In the first one the intrinsic paramagnetic property of the cells is utilized. This method is only suitable to separate strongly paramagnetic cells such as red blood cells; a more common method is to label cells using magnetic beads. The magnetic force is a function of the magnitude and the gradient of the magnetic field. The magnetic field is normally produced by permanent magnets [2] or electromagnets, but due to the bulky nature of these devices it is not very suitable for incorporation into a lab-on-chip device. More recently, micro inductors that can be easily incorporated into microfluidic systems have been employed [3].

1.2.2 Acoustic Manipulation

Particle manipulation based on acoustic methods utilizes ultrasonic frequencies. Acoustic manipulation of particles is based on acoustic pressure gradients whereas DEP is based on the electric field gradients. The ultrasonic acoustic waves are generated using a piezo-actuator. The acoustic force that is generated requires a specific fluidic channel design in order to establish a standing wave. The sites at which particles aggregate correspond to the nodes and antinodes of the standing wave [4]. The critical factors involved are the particle properties such as size, density and compressibility. The cells that flow in the separation chamber are subjected to an acoustic force and migrate either towards the nodes or towards the antinodes. The separation of lipid particles from red blood cells has been reported using this method [5], where the width of the channel was chosen to be half the ultrasonic wavelength. This resulted in the red blood cells accumulating in the pressure nodes, whereas the lipid particles collected at the side walls of the channel.

1.2.3 Fluidic Manipulation

With the ability to precisely control microfluidic flow it is possible to exert variable hydrodynamic drag forces on particles suspended in the fluid [6]. Separation in these devices is generally based on the particle size and shape and it avoids the needs for any active external forces such as electrical forces and extensive sample preparation. The separation of white blood cells from red blood cells has been demonstrated in [7], the smaller erythrocytes continue along the faster flow regions but the white blood cells are pushed towards the nearest side walls due to collisions with erythrocytes. This results in separation of the two cell types.

Fluidic sorting methods based on specific adhesion between the flowing cells and channel surfaces also holds strong potential for cell sorting. A functionalized microfluidic substrate surface can be used to slow down selective cells while allowing other cells to flow without any disruption. This method allows us to mimic physiological phenomena occurring in blood vessels which are based on adhesive interactions [8].

1.2.4 Electrical Manipulation

1.2.4.1 Electrophoresis

Electrophoresis can be defined as the motion of charged particles in fluids by an electric field. The electrophoretic approach utilizes the fact that most cells carry a net negative surface charge at physiological pH. The charge density varies from one cell type to another and this can be utilized for separation of different cell types. A highly efficient separation of microbes has been demonstrated using this method [9].

1.2.4.2 Electroosmosis

Electroosmosis can be defined as the fluid flow induced by a charged surface, and can be achieved by using both AC and DC voltages. DC electroosmosis is widely used to

drive fluid through micro channels with very good control. This effect can also be used to manipulate suspended matter in the fluid. Using this method, the aggregation of suspended particulate matter has been demonstrated [10].

1.2.4.3 Dielectrophoresis (DEP)

The term dielectrophoresis is defined as the effect where a particle undergoes movement as a result of its dielectric properties and the influence of a non-uniform electric field. A neutral particle exhibits DEP in a direct current or alternating current generated electric field. H. A. Pohl introduced the term dielectrophoresis [11], and he also laid out the methods and theories for the DEP characterization and separation of biological particles. The emergence of lab-on-chip microfluidic technologies has led to a steep increase in the amount of work in the area of DEP. A primary driver for DEP technologies has been the ability to manipulate biological particles for purposes of separation, tissue engineering, and electrical characterization. DEP is the most versatile and controllable manipulation method of the methods mentioned above, as it taps into the unique dielectric signature of each particle. Some of the previous work done in the area of DEP in biological and non biological realms is detailed below.

DEP has been used extensively to enrich position and characterize mammalian cells. A few examples are described here: Dielectrophoretic fractionation of human breast carcinoma cells based on the cell cycle phase was demonstrated in [12]. The patterning of liver cells and endothelial cells was achieved using DEP traps in a microfluidic chip [13]. The enrichment of putative stem cells from adipose tissue was carried out using DEP [14]. Evaluation of multi-drug resistance in lukeukemic cells using dielectrophoresis [15]. Continuous dielectrophoretic separation of blood cells using a lateral DEP force [16]. DEP has been useful in detecting infections such as malaria infected blood cells from normal erythrocytes using DEP characterization [17].

A neuron-based sensor for detecting a mixture of chemical analytes in diesel has been used by Shalini et al.[18].

DEP is a useful method for food and water testing for the detection of yeast, algal cells, bacteria and submicron biological particles such as viruses [19-24].

DEP also possesses the ability to manipulate molecular biopolymers such as proteins and DNA. DEP has been shown to be an effective technique for stretching and positioning of DNA [25] and the separation of DNA molecules based on their length dependant polarisabilities [26]. Identification, purification and manipulation of proteins are critical to many pharmaceutical purposes and DEP provides a viable alternative to answer some of the separation problems of existing methods [27-30].

Recently, DEP has been shown to be an efficient method for the assembly of carbon nanotubes and zinc oxide nanowires for building electronic circuits such as field effect transistors [31-34]. Assembly of GaN nanowires using DEP was also recently applied to UV sensor applications [35], providing very fast response times.

1.3 Dielectric Spectroscopy

Dielectric spectroscopy enables the investigation of intermolecular interactions and other critical processes. Investigation of the dielectric properties of particles, especially biological particles, has led to various scientific discoveries - such as thickness of the plasma membrane of an erythrocyte [36] and the electrical determination of the fertilization of an egg [37]. The various methods which are currently being used to study the bio-dielectric properties are summarised below

1.3.1 Impedance Measurements

Dielectric properties of particles are most commonly measured using direct impedance measurements over a large frequency range. Using this method we can study the impedance of particles suspended in a known buffer medium can be studied using direct measurements. The common approach is to characterise a large number of particles suspended in fluid [38]. More recently, work has also been performed on a single particle level [39]. The effect of AC Voltage frequencies on a biological cell suspended in a buffer, different types of cells can be identified because of their characteristic impedance signatures.

1.3.2 DEP Spectroscopy

For a fixed suspending solution and set of positions in an electrode array, the DEP forces depend only on the intrinsic cell characteristics such as size, membrane capacitance, internal conductivity and membrane conductivity. By subjecting cells to non-uniform electric fields and by observing and characterizing their motion it is possible to deduce minute physiological changes from one cell type to another. It is also possible to measure subtle changes that occur after treatment with measured amounts of drugs [15].

1.3.3 Electrorotation

Electrorotation is a result of a torque that is induced on a particle when subjected to a rotating electric field. The particle can be induced to rotate in the same or in the opposite sense to that of the imposed rotating electric field. The direction and magnitude of the rotation is determined by the phase difference between the field and the polarity of the induced dipole moment in the particle. The rotation rate provides useful information on dielectric characteristics of particles. This method was first applied to biological materials by W. M. Arnold and U. Zimmermann [40]. Different

biological particle such as lymphocytes, plant protoplasts and erythrocytes have since been investigated. Using this method it is possible to monitor subtle changes of membrane capacitance and conductivity, and also changes occurring in the dielectric properties of the cytoplasm [41].

1.4 Thesis Format and Content

The subject matter of the research reported in this thesis was directed towards certain applications of DEP, for the development of lab-on-chip technologies for biological applications. The second chapter provides the theory of cell manipulation using DEP, and discusses aspects such as interfacial polarisation, forces on dipoles and multipoles in an inhomogeneous field. The underlying theory involved in incorporating microfluidics with DEP devices is also described, together with a brief introduction to other AC electrokinetic fluid effects such as electrothermal and electroosmotic forces. An analysis is also given of the simulation method used in this work, namely the Finite Element Method, and is demonstrated using a COMSOL Multiphysics example.

Chapter 3 discusses how the AC Electric field frequency and magnitude can be controlled to either minimise or enhance the number of cells destroyed during DEP experiments. This chapter explains how the stress induced across the plasma membrane by the applied electric field leads to cell destruction. Details of the effects of frequency are mentioned especially around the DEP cross-over frequency, where the induced membrane field has yet to fall off significantly in magnitude thereby causing increased stress across the membrane. The work in this chapter has been published in the Journal of IET Nanobiotechnology in 2005.

In Chapter 4, the use of DEP for the separation of Small Cell Lung Cancer Cell (SCLC) phenotypic variants has been explained. DEP was found to possess the ability to selectively sort SCLC phenotypes with subtle differences in membrane morphology.

Prior to sorting, DEP characterization studies were performed and the results indicate that phenotype differences can be identified leading to the possibility of cytometric devices for analysis, identification and monitoring of tumor metastaticity. The work in this chapter was published in the NSTI Nanotechnology conference proceedings in 2008.

Chapter 5 outlines the design and development of dielectrophoretic tweezers to separate individual cells of interest, such as the cells over expressing a protein of interest that is tagged to the green fluorescent protein (GFP). Simulations were performed to understand the influence of the design parameters and the AC voltage. It was found that this method is capable of achieving very high selectivity and a distinct cost advantage over more conventional methods. The work in this chapter was presented in a poster at the Gordon conference in 2008 and will shortly be submitted for journal publication.

Chapter 6 discusses the optimization of a 3D DEP electrode system for engineering three dimensional cell constructs in order to better understand the effects of cell-cell interactions and intercellular transport events in three dimensional cell aggregations. Using the 3-D DEP electrode system, suspensions of BETA-TC-6 and INS-1 cells were condensed into three-dimensional cell constructs of roughly the same size and cell density as the insulin secreting pancreatic structures known as islet of Langerhans. Alternative electrode geometries were also used in order to establish a comparative study of aggregation efficiency. The work in this chapter has been published in the Journal of IET Nanobiotechnology in 2008 and a poster was presented at a conference of the biophysical society.

In Chapter 7, contributions of the work presented in this thesis are summed up. A discussion of the possible areas of refinement and future work has been outlined.

1.5 References

- 1) Duffy, D., McDonald, J., Schueller, O., and Whitesides, G., Rapid prototyping of microfluidic systems in poly(dimethylsiloxane), *Analytical Chemistry*, 1998, 70, pp. 4974–4984.
- 2) Nakamura M., Decker K, Chosy J, Comella K., Melnik K., Moore L., Lasky L.C., Zborowski M., and Chalmers J. J., 'Separation of a breast cancer cell line from human blood using a quadrupole magnetic flow sorter', *Biotechnol. Prog.*, 2001, 17, pp. 1145–1155
- 3) Rong, R., Choi, J.W. and Ahn C.H., 'An on-chip magnetic bead separator for biocell sorting', *J. Micromech. Microeng.*, 2006, 16, pp. 2783–2790
- 4) Nilsson, A., Petersson, F., Jönsson, H., and Laurell, T., 'Acoustic control of suspended particles in micro fluidic chips' *Lab Chip*, 2004, 4, pp. 131–135
- 5) Laurell, T., Petersson, F., and Nilsson, A., 'Chip integrated strategies for acoustic separation and manipulation of cells and particles', *Chem. Soc. Rev.*, 2007, 36, pp. 492–506
- 6) Zheng, S., Liu, J.Q., and Chong, Y., 'Streamline-Based Microfluidic Devices for Erythrocytes and Leukocytes Separation', *Journal of microelectromechanical systems*, 2008, 17, pp. 1029-1038
- 7) Shevkoplyas, S.S., Yoshida, T., Munn, L.L., and Bitensky, M.W., 'Biomimetic Autoseparation of Leukocytes from Whole Blood in a Microfluidic Device', *Anal. Chem.*, 2005, 77, pp. 933-937
- 8) Chang, W.C., Lee, L.P., and Liepmann, D., 'Biomimetic technique for adhesion-based collection and separation of cells in a microfluidic channel', *Lab Chip*, 2005, 5, pp. 64–73
- 9) Desai, M.J., and Armstrong, D.W., 'Separation, Identification, and Characterization of Microorganisms by Capillary Electrophoresis', *Microbiology and Molecular Biology Reviews*, 2003, 67, pp. 38–51
- 10) Wu, J., 'Biased AC Electro-Osmosis for on-Chip Bioparticle Processing', 2006, 5, pp. 84-89
- 11) Pohl, H.A., 'Dielectrophoresis'. , Cambridge Univ. Press, Cambridge, 1978
- 12) Kim, U., Shu, C.W., Dane, K.Y., Daugherty, P.S., Wang, J.Y.J., and Soh, H.T. , ' Selection of mammalian cells based on their cell-cycle phase using dielectrophoresis', *P.N.A.S.*, 2007, 104, pp. 20708–20712
- 13) Ho, C.T., Lin, R.Z., Chang, W.Y. , Chang, H.Y., and Liu, C.H., 'Rapid heterogeneous liver-cell on-chip patterning via the enhanced field-induced dielectrophoresis trap', *Lab Chip*, 2006, 6, pp. 724–734
- 14) Vykoukal, J., Vykoukal, D.M., Freyberg, S., Alt, E.U. and Gascoyne, P.R.C., 'Enrichment of putative stem cells from adipose tissue using dielectrophoretic field-flow fractionation', *Lab Chip*, 2008, 8, pp. 1386–1393

- 15) Labeed, F.H., Coley, H. M., Thomas, H., Hughes, M.P., 'Assessment of Multidrug Resistance Reversal Using Dielectrophoresis and Flow Cytometry', *Biophysical Journal*, 2003, 85 pp. 2028–2034
- 16) Han, H.K. and Frazier, B.A., 'Lateral-driven continuous dielectrophoretic microseparators for blood cells suspended in a highly conductive medium', *Lab Chip*, 2008, 8, pp. 1079–1086
- 17) Gascoyne, P., Mahidol, C., Ruchirawat, M., Satayavivad, J., Watcharasit, P. and Becker, F. F. 'Microsample preparation by dielectrophoresis: isolation of malaria', *Lab Chip*, 2002, 2, pp. 70–75
- 18) Prasad, S. Zhang, X., Ozkan, S.C., Ozkan, M., 'Neuron-based microarray sensors for environmental sensing', *Electrophoresis* 2004, 25, pp. 3746–3760
- 19) Ikeda, I., Tsukahara, S., Watarai, H., 'Effects of Viability and Lectin Protein Binding on Dielectrophoretic Behavior of Single Yeast Cells', *Analytical Sciences*, 2003, 19, pp. 27-31
- 20) Hubner, Y., Hoettges, K. F., and Hughes, M.P., 'Water quality test based on dielectrophoretic measurements of fresh water algae *Selenastrum capricornutum*', *J. Environ. Monit.*, 2003, 5, pp. 861–864
- 21) Ermolina, I., Milner, J., Morgan, H., 'Dielectrophoretic investigation of plant virus particles: Cow Pea Mosaic Virus and Tobacco Mosaic Virus' *Electrophoresis* 2006, 27, pp. 3939–3948
- 22) Suehiro, J., Hamada, R., Noutomi, D., Shutou, M., Hara, M., 'Selective detection of viable bacteria using dielectrophoretic impedance measurement method', *Journal of Electrostatics*, 2003, 57, pp. 157–168
- 23) Lapizco-Encinas, B.H., Davalos, R.V., Simmons, B.A., Cummings, E.B. and Fintschenko, Y., 'An insulator-based (electrodeless) dielectrophoretic concentrator for microbes in water', *Journal of Microbiological Methods*, 2005, 62, pp. 317– 326
- 24) Markx, G.H., Andrews, J.S., and Mason, V.P., 'Towards microbial tissue engineering?' *TRENDS in Biotechnology*, 2004, 22, pp. 417-422
- 25) Markx, G.H., Talary, M.S., and Pethig, R., 'Separation of viable and non-viable yeast using dielectrophoresis', *Journal of Biotechnology*, 1994, 32, pp. 29-37
- 26) Hughes, M.P., and Morgan, H., ' Dielectrophoretic Characterization and Separation of Antibody-Coated Submicrometer Latex Spheres' , *Anal. Chem.*, 1999, 71, pp. 3441-3445
- 27) Henning, A., Henkel, J., Bier, F.B., and Hölzel, R., 'Label-free electrical quantification of the dielectrophoretic response of DNA', *PMC Biophysics*, 2008, 1, pp. 1-12
- 28) Aghdaei, S., Sandison, M.E., Zagnoni, M., Green, N.G., and Morgan, H., 'Formation of artificial lipid bilayers using droplet dielectrophoresis', *Lab Chip*, 2008, 8, pp. 1617–1620

- 29) Regtmeier, J., Duong, T.T., Eichhorn, R., Anselmetti, D., and Ros, A., 'Dielectrophoretic Manipulation of DNA: Separation and Polarizability', *Anal. Chem.*, 2007, 79, pp. 3925-3932
- 30) Lapizco-Encinas, B.H., Ozuna-Chacon, S., and Palomares, M., 'Protein manipulation with insulator-based dielectrophoresis and direct current electric fields' *Journal of Chromatography A*, 2008, 1206, pp. 45–51
- 31) Mureau, N., Mendoza, E., and Silva, P.R.S, 'Dielectrophoretic manipulation of fluorescing single-walled carbon nanotubes', *Electrophoresis*, 2007, 28, pp. 1495–1498
- 32) Zhang, L.J., Yang, Q., and D., Tian, J., 'Fabrication of carbon nanotube field effect transistors by AC dielectrophoresis method', *Carbon*, 2004, 42, pp. 2263–2267
- 33) Krupke, R., Linden, S., Rapp, M., and Hennrich, F., 'Thin Films of Metallic Carbon Nanotubes Prepared by Dielectrophoresis', *Adv. Mater.*, 2006, 18, pp. 1468–1470
- 34) Suehiro, J., Nakagawa, N., Hidaka, S. I., Ueda, M., Imasaka, K., Higashihata, M., Okada, T., and Hara, M., 'Dielectrophoretic fabrication and characterization of a ZnO nanowire-based UV photosensor', *Nanotechnology*, 2006, 17, pp. 2567–2573
- 35) Lao, C.S., Liu, J., Gao, P., Zhang, L., Davidovic, D., Tummala, R., and Wang, Z. L., 'ZnO Nanobelt/Nanowire Schottky Diodes Formed by Dielectrophoresis Alignment across Au Electrodes', *Nano Lett.*, 2006, 6, pp. 263-266
- 36) Gorter, E., and Grendel, F., 'On bimolecular layers of lipoids on the chromocytes of the blood', *The Journal of Experimental Medicine*, 1925, 41, pp. 439-443
- 37) Cole, K.S., and Curtis, H.J, 'Electric impedance of single marine eggs' *J. Gen. Physiol.*, 1938, 21, pp. 591–599
- 38) Schwan, H.P., Schwarz, G., Maczuk, J., and Pauly, H., 'On the low-frequency dielectric dispersion of Colloidal particles in electrolyte solution', *J. Phys. Chem.*, 1962, 66, pp. 2626-2635
- 39) Sun, T., Holmes, D., Gawad, S., Green, N.G., and Morgan, H., 'High speed multi-frequency impedance analysis of single particles in a microfluidic cytometer using maximum length sequences', *Lab Chip*, 2007, 7, pp. 1034–1040
- 40) Arnold, W.M., and Zimmermann, U., 'Rotating-field-induced rotation and measurement of the membrane capacitance of single mesophyll cells of *Avena sativa* [oat]', *Zeitschrift fuer Naturforschung*, 1982, 37, pp. 908-915
- 41) Huang, Y., Wang, X.B., Gascoyne, P. R.C., and Becker, F.F., 'Membrane dielectric responses of human T-lymphocytes following mitogenic stimulation' *Biochimica et Biophysica Acta*, 1999, 1417, pp. 51-62

Chapter 2

Theory

2.1 Dielectrics in Electric Fields

Dielectrics are substances that do not possess free electric charges but have the ability to modify the electric field and they can broadly be classified as polar and non-polar. Polar molecules have a permanent dipole moment and non polar molecules undergo electric charge displacement in or around the molecule. There are various polarisation mechanisms such as interfacial, orientational, atomic and electronic polarisations as shown in figure 2.1. In the case of electronic polarisation the centre of the charge of the electron cloud in an atom moves slightly with respect to the centre of the charge of the nucleus. Atomic polarisation occurs in crystalline substances where ions of different charges move in different direction when subjected to an electric field. Orientational polarisation occurs in molecules which have a permanent dipole moment and this is because these molecules experience a torque to align themselves with the electric field [1, 2].

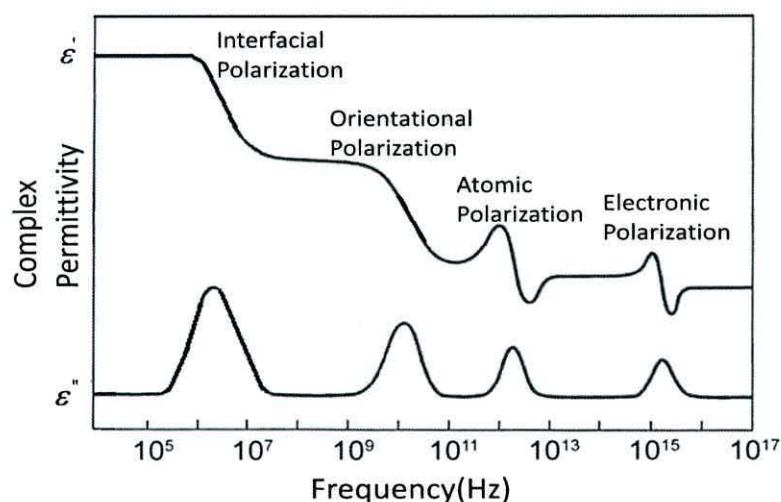


Figure 2.1: Different frequency dependant polarisation mechanisms of a dielectric particle. The real part of the complex permittivity relates to the energy stored in the dielectric and imaginary part relates to the loss of energy in a dielectric.

According to the differential form of Gauss's law, the divergence of the electric flux density \mathbf{D} is equal to the free volume charge density ρ_f

$$\nabla \cdot \mathbf{D} = \rho_f \quad (2.1)$$

The electric flux density \mathbf{D} is defined as

$$\mathbf{D} = \varepsilon_o \mathbf{E} + \mathbf{P}, \quad \mathbf{P} = \chi \varepsilon_o \mathbf{E} \quad (2.2)$$

where \mathbf{E} denotes the electric field, \mathbf{P} is the polarization, ε_o is the absolute permittivity of free space and χ is the electric susceptibility of the dielectric. For a linear and isotropic dielectric, the polarisation \mathbf{P} is proportional to the total electric field intensity [2-5] as shown in equation 2.2. In a non-ideal dielectric with conductivity σ , in the presence of an AC field, the polarisation mechanism is more convoluted as it causes a phase shift between the field and the induced polarization. The Polarisation \mathbf{P} is then given by [2]

$$\mathbf{P} = \varepsilon_o \left(\frac{\varepsilon^*}{\varepsilon_o} - 1 \right) \mathbf{E}, \quad \varepsilon^* = \varepsilon - \frac{j\sigma}{\omega} \quad (2.3)$$

Where ε^* is the complex permittivity of the dielectric.

Interfacial polarisation or Maxwell-Wagner mechanism plays a significant role in the dielectrophoretic mechanism of biological cells since biological particles exhibit both pure dielectric as well as electrical conductivity properties. The Maxwell-Wagner effect is an interfacial relaxation process which occurs in systems where the electric current must pass an interface between two different dielectrics. This can be explained by means of a parallel plate capacitor with two different materials placed in series between the capacitor plates as shown in figure 2.2. In this case, a classical Debye type dispersion without any dipole relaxation in the dielectric [2, 3], is observed. The dispersion is due to a conductance in parallel with a capacitance for each dielectric resulting in the charging of the interface by means of electrical conduction. If the interface does not possess free charges the dielectric displacement is continuous and hence does not exhibit such an interfacial polarisation mechanism.

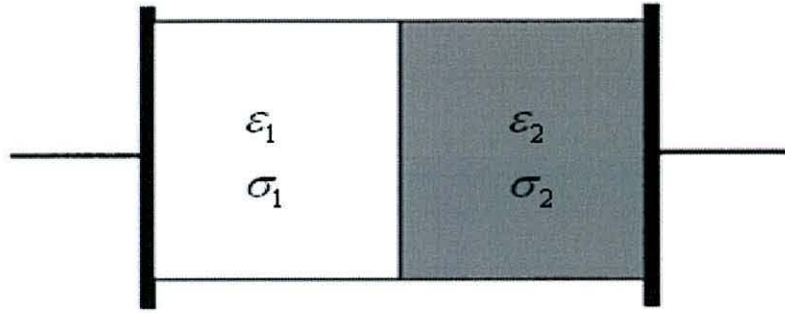


Figure 2.2: A parallel plate capacitor containing two lossy dielectrics.

2.2 Force on an Infinitesimal Dipole and Effective Dipole Moment of a Sphere

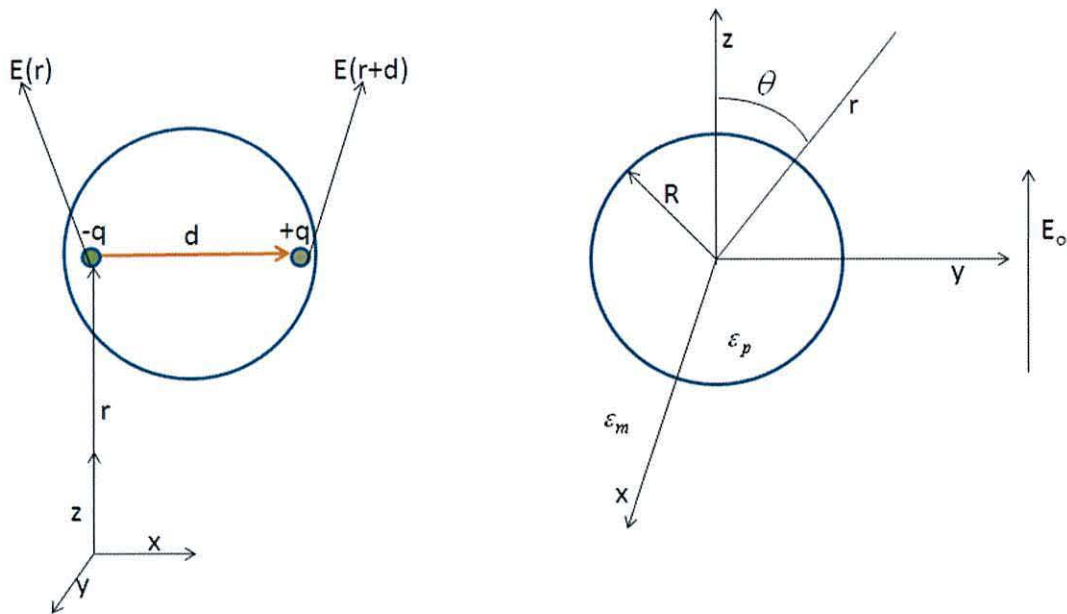


Figure 2.3: (a) Force on a small dipole due to an electric field. (b) Force on a dielectric sphere of radius R , permittivity ϵ_p suspended in a medium ϵ_m .

The starting point for formulating the force exerted on a dielectric particle is to estimate the net force upon a small physical dipole [5, 6], since a neutral particle far away can be represented by a dipole moment as shown in figure 2.3a. A non-uniform electric field is applied to a dipole with a distance vector d between the two charges. The

electric fields at the two charges are not equal, and the sum of electric forces on the particle is

$$\mathbf{F} = q\mathbf{E}(\mathbf{r} + \mathbf{d}) - q\mathbf{E}(\mathbf{r}) \quad (2.4)$$

where \mathbf{r} is the position vector of $-q$. The electric field at the position of $+q$ can be expressed by Taylor's expansion

$$\mathbf{E}(\mathbf{r} + \mathbf{d}) = \mathbf{E}(\mathbf{r}) + \mathbf{d} \cdot \nabla \mathbf{E}(\mathbf{r}) + \dots \quad (2.5)$$

$$\mathbf{F} = q\mathbf{d} \cdot \nabla \mathbf{E} + \dots \quad (2.6)$$

If higher order derivatives of the electric field are neglected, and since the dipole moment is $\mathbf{p} = q\mathbf{d}$, the approximate expression of the force on the dipole can be expressed as

$$\mathbf{F} = \mathbf{p} \cdot \nabla \mathbf{E} \quad (2.7)$$

In figure 2.3b, a homogeneous dielectric sphere of radius R , permittivity ϵ_p , and conductivity σ_p , is assumed to be immersed in a dielectric medium of permittivity ϵ_m and conductivity σ_m and subjected to an electric field of magnitude E_0 . This case has one interface and one relaxation frequency. The effective dipole moment p_{eff} for a particle can be defined as the moment of an equivalent, free-charge, point dipole that, when immersed in the same dielectric liquid and positioned at the same location as the center of the original particle, produces the same dipolar electrostatic potential. The electrostatic potential ϕ_{dipole} due to a point dipole of moment p_{eff} , in a dielectric medium can be simplified to

$$\phi_{dipole} = \frac{p_{eff} \cos \theta}{4\pi \epsilon_m r^2} \quad (2.8)$$

where θ and r are, respectively, the polar angle and the radial position in spherical coordinates.

The derivation of the effective dipole moment is made under simplifying conditions. That is, the applied electric field outside the particle is taken to be a uniform magnitude E_o and parallel to z axes. The electrostatic potential satisfies Laplace's equation outside $\phi_1(r, \theta)$ and $\phi_2(r, \theta)$ inside

$$\phi_1(r, \theta) = -E_o r \cos\theta + \frac{A \cos\theta}{r^2}, \quad r > R \quad (2.9)$$

$$\phi_2(r, \theta) = -B r \cos\theta, \quad r < R \quad (2.10)$$

A and B are the unknown coefficients to be determined by the boundary conditions. The first term in the right hand side of equation 2.9, is the imposed electric field, and the second term is due to the dipole moment of the particle. There are two boundary conditions at the surface $r = R$. One is that the electric potential should be continuous and the second is that the normal component of the displacement flux vector must be continuous across the boundary

Upon imposing these boundary conditions

$$A = \frac{\epsilon_p - \epsilon_m}{\epsilon_p + 2\epsilon_m} R^3 E_o \quad \text{and} \quad B = \frac{3\epsilon_m}{\epsilon_p + 2\epsilon_m} E_o \quad (2.11)$$

Upon comparing the equation 2.11 to the induced electric dipole term in equation 2.9, yields a useful general relationship between the effective moment and the coefficient A

$$p_{eff} = 4\pi\epsilon_m A \quad (2.12)$$

For the special case of the homogeneous, dielectric sphere, the expression for the effective dipole moment is

$$p_{eff} = 4\pi\epsilon_m CM R^3 E_o \quad (2.13)$$

The Clausius-Mossotti function CM , provides a measure of the strength of the effective polarisation of a spherical particle as a function of ϵ_m and ϵ_p .

$$CM(\epsilon_p, \epsilon_m) = \frac{\epsilon_p - \epsilon_m}{\epsilon_p + 2\epsilon_m} \quad (2.14)$$

When $\varepsilon_p > \varepsilon_m$, then $CM > 0$ and the effective moment vector p_{eff} is collinear with the imposed electric field vector E_o . On the other hand, when $\varepsilon_p < \varepsilon_m$, then $CM < 0$ so that p_{eff} and E_o are antiparallel.

Figure 2.4 shows the direction of the dipole moment p and dielectrophoretic force vector on a dielectric sphere. The electric field lines shows the density of the electric field in the particle and it is clear that when the particle is less polarisable than the medium the electric field lines are pushed around the particle and the field strength inside the particle is high. In the case where the particle is more polarisable than the medium the electric field lines intersect the surface at right angles and the field strength inside the particle is low.

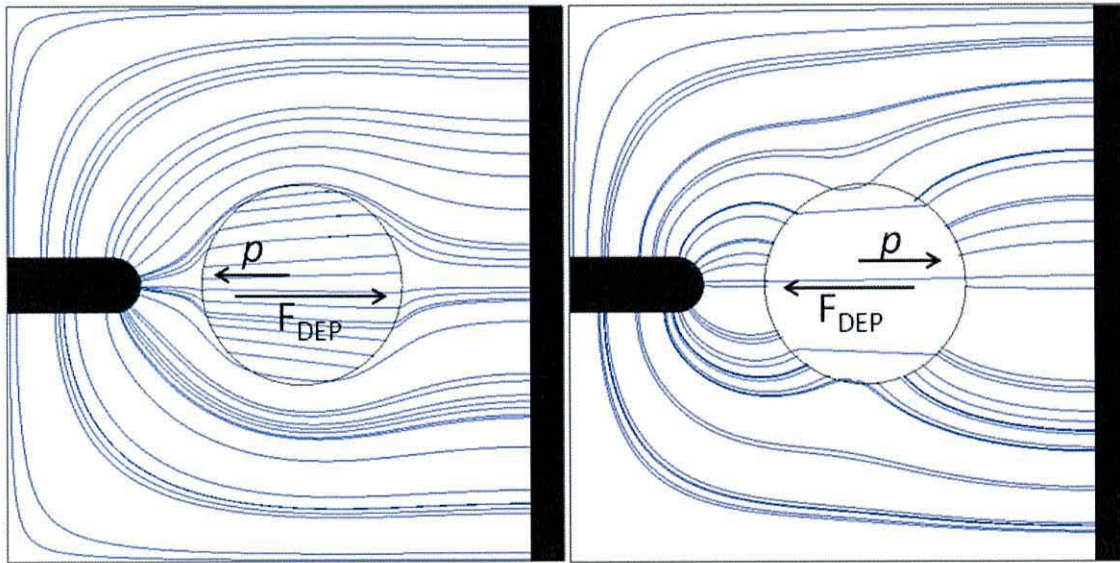


Figure 2.4: Schematic showing the electric field lines and the direction of the electric dipole moment p and the dielectrophoretic force vector induced in a dielectric sphere. (a) The particle is less polarisable than the medium. (b) The particle is more polarisable than the medium.

2.2.1 DEP Force in an AC Field

For deriving the DEP force in a time varying electric field, a field having a spatially varying field magnitude and constant phase is considered. Assuming an applied potential of a single frequency ω , the electric field will be given by [7]

$$\mathbf{E}(r, t) = \text{Re}[\mathbf{E}(r)e^{i\omega t}] \quad (2.15)$$

where r is the spatial position

$$\mathbf{p}_{eff}(t) = 4\pi\epsilon_m \text{Re}[CM]R^3 \text{Re}[\mathbf{E}(r)e^{i\omega t}] \quad (2.16)$$

where $CM(\epsilon_p^*, \epsilon_m^*)$ is the complex Clausius-Mossotti factor and ϵ_p^* is the complex

permittivity given by $\epsilon_p^* = \epsilon_p - \frac{j\sigma_p}{\omega}$

$$CM(\epsilon_p^*, \epsilon_m^*) = \frac{\epsilon_p^* - \epsilon_m^*}{\epsilon_p^* + 2\epsilon_m^*} \quad (2.17)$$

The time dependant DEP force is given by substituting 2.15 and 2.16 into 2.7

$$\mathbf{F}_{DEP} = \mathbf{p}_{eff}(t) \cdot \nabla \text{Re}[\mathbf{E}(r)e^{i\omega t}] \quad (2.18)$$

Upon simplifying equation 2.17, the time averaged DEP force equation is given by

$$\mathbf{F}_{DEP} = 2\pi\epsilon_m \text{Re}[CM]R^3 \nabla |\mathbf{E}_{rms}|^2 \quad (2.19)$$

The dielectrophoretic force is often represented using the root mean square values (*rms*) of the electric field, as shown in equation 2.19. The *rms* notation is often confusing and from now on in this thesis, the expression for the DEP force will contain the peak amplitude of the electric field, given by equation 2.20

$$\mathbf{F}_{DEP} = \pi\epsilon_m \text{Re}[CM]R^3 \nabla |\mathbf{E}|^2 \quad (2.20)$$

An expression for Clausius-Mossotti factor that gives us some understanding into the frequency dependent behavior can be given by [7]

$$\text{Re}[CM] = \epsilon_m \left(\frac{\omega^2 \tau_{M\omega}^2}{1 + \omega^2 \tau_{M\omega}^2} \left(\frac{\epsilon_p - \epsilon_m}{\epsilon_p + 2\epsilon_m} \right) + \frac{1}{1 + \omega^2 \tau_{M\omega}^2} \left(\frac{\sigma_p - \sigma_m}{\sigma_p + 2\sigma_m} \right) \right) \quad (2.21)$$

where ω is the angular frequency of the applied field, and $\tau_{M\omega}$ is the relaxation time constant, which explains that for lossy particles the dipole moment of the particle in an oscillating field exhibits a phase lag. This delay or lag depends on the accumulation of

free charge at the particle-medium interface giving rise to the induced dipole moment and it equates to the interfacial free charge to build up to $\frac{1}{e}$ times the final value. The corresponding relaxation time is given by [7]

$$\tau_{M\omega} = \frac{\varepsilon_p + 2\varepsilon_m}{\sigma_p + 2\sigma_m} \quad (2.22)$$

For low frequency values ($\omega\tau_{M\omega} \rightarrow 0$), the Clausius-Mossotti factor reduces to

$$\lim_{\omega\tau_{M\omega} \rightarrow 0} \text{Re}[CM(\omega)] = \left(\frac{\sigma_p - \sigma_m}{\sigma_p + 2\sigma_m} \right) \quad (2.23)$$

For high frequency values ($\omega\tau_{M\omega} \rightarrow \infty$)

$$\lim_{\omega\tau_{M\omega} \rightarrow \infty} \text{Re}[CM(\omega)] = \left(\frac{\varepsilon_p - \varepsilon_m}{\varepsilon_p + 2\varepsilon_m} \right) \quad (2.24)$$

From equations 2.23 and 2.24, the interfacial polarisation properties of the particle at low frequency depend on the conductive properties of the particle and medium and at higher frequencies the permittivity is dominant.

In certain cases the dipole approximation is not sufficient in regions where the field strength is extremely spatially non-uniform over the particle dimensions. To determine the exact forces on the particle it is necessary to use the Maxwell stress tensor. However, this is a very complicated approach and some of the required physical parameters are not readily calculable. A more simple approach is the multipole approach given by Jones and Washizu [8, 9].

The multipolar force approximation is sufficient to provide an accurate representation of the force on a spherical particle and this can be given by [8, 9]

$$\mathbf{F}_{DEP}^{(n)} = \frac{\mathbf{p}^{(n)} [\cdot]^n (\nabla)^n \mathbf{E}}{n!} \quad (2.25)$$

where n refers to the force order ($n=1$ is the dipole, $n=2$ is the quadrupole and $n=3$ is for the octupole), $[\cdot]^n$ represents the n dot products, $(\nabla)^n$ represents the n gradient operations, and $\mathbf{p}^{(n)}$ is the multipolar induced tensor of order n

$$\mathbf{p}^{(n)} = \frac{4\pi\epsilon_m R^{2n+1} n}{(2n+1)!!} CM^{(n)} (\nabla)^{n-1} \mathbf{E} \quad (2.26)$$

The multipolar CM factor for a uniform lossy dielectric sphere is given by

$$CM^{(n)} = \frac{\epsilon_p^* - \epsilon_m^*}{n\epsilon_p^* + (n+1)\epsilon_m^*} \quad (2.27)$$

2.2.2 Electrorotation

When a spherical particle is subjected to a rotating electric field a time averaged electrical torque is exerted [10]. Similar to DEP electrorotation is also caused by the differences in the field induced polarisation between the particle and the surrounding medium. Electrorotation is a very useful method to measure the physiological state of the cell. The torque exerted on a dielectric particle in a uniform electric field is given by [10]

$$\mathbf{T} = \frac{1}{2} \text{Re}[\mathbf{p}_{eff} \times \mathbf{E}^*] \quad (2.28)$$

where \mathbf{E}^* is the electric field and it is assumed to be a right circularly polarised vector of magnitude E

$$\mathbf{T} = -4\pi\epsilon_m R^3 E^2 \text{Im}[CM(\epsilon_p^*, \epsilon_m^*)] \hat{\mathbf{z}} \quad (2.29)$$

2.3 Multi Shelled Model

Biological cells have complex internal heterogeneous structure with components such as wall, membrane and nucleus. Therefore in order to express the interfacial polarisation effects that occur at each interface, a shelled model which provides an

approximation of various compartments within a real biological cell is used [7, 11]. By adding more interfaces the number of dispersions also increases. The most widespread approach used is to model cells as concentric spheres called shells. Figure 2.5 shows a cell and the equivalent two-shelled model. Analytical calculation brings iteratively the 2 shell model to an effective homogeneous sphere model. The mathematical reduction from a two shelled sphere is explained [12]

$$\varepsilon_{eff2}^* = \frac{\varepsilon_2^*(R_2^3(\varepsilon_1^* + 2\varepsilon_2^*) - 2R_1^3(\varepsilon_2^* - \varepsilon_1^*))}{(R_2^3(\varepsilon_1^* + 2\varepsilon_2^*) + R_1^3(\varepsilon_2^* - \varepsilon_1^*))} \quad (2.30)$$

$$\varepsilon_{eff}^* = \frac{\varepsilon_3^*(R_3^3(\varepsilon_{eff2}^* + 2\varepsilon_3^*) - 2R_2^3(\varepsilon_3^* - \varepsilon_{eff2}^*))}{(R_3^3(\varepsilon_{eff2}^* + 2\varepsilon_3^*) + R_2^3(\varepsilon_3^* - \varepsilon_{eff2}^*))} \quad (2.31)$$

$$CM = \frac{\varepsilon_{eff}^* - \varepsilon_{medium}^*}{\varepsilon_{eff}^* + 2\varepsilon_{medium}^*} \quad (2.32)$$

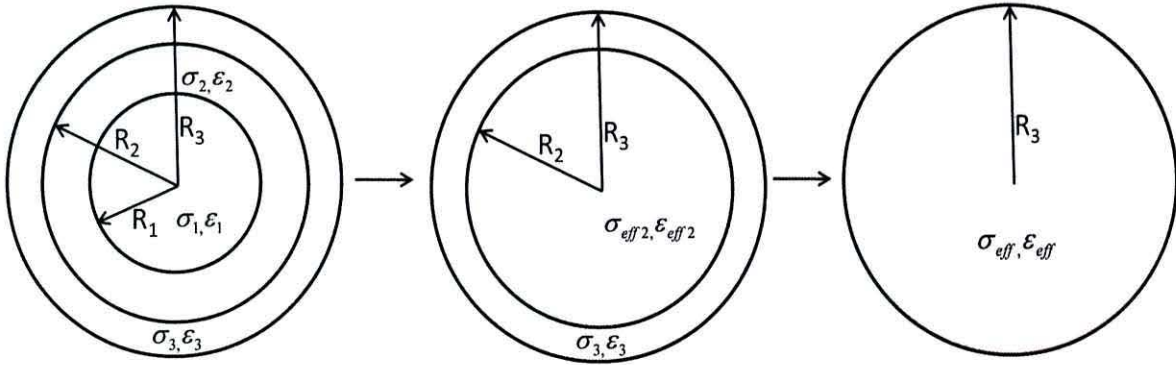


Figure 2.5: Schematic of a shelled model used to determine the effective permittivity of a two-shelled model of a homogeneous sphere.

As an example, a single shelled model of a lymphocyte [13] is considered. Here the cell is simplified to be a conducting sphere surrounded by a poorly conducting cell membrane. The four parameters that are varied to characterize the effects of cell parameters on the dielectric behavior are the membrane specific capacitance,

membrane conductivity, the cell radius and the internal conductivity of the cell. The values used for this modeling has been extracted from [13].

In figure 2.6a, increasing the cell radius results in a positive shift in the lower cross over frequency, but, at higher frequencies the effects of cell radius are not strongly observed and this is because in the higher frequency regime, the real part of the Clausius-Mossotti factor is dominated by smaller polarisation processes such as the dispersion that occurs around the nuclear envelope.

In figure 2.6b, an increase in the specific membrane capacitance which in reality is a result of changes in membrane morphology results in a positive shift in the lower cross over frequency. The work in the following chapters uses the effect of membrane capacitance for distinguishing cell types with slightly different morphologies. The effects of membrane morphology in relation to the lower frequency DEP responses has been studied extensively [14-17]. At higher frequencies the effects of membrane capacitance are not strongly observed and this is because in the higher frequency regime, the real part of the Clausius-Mossotti factor is dominated by smaller processes.

The cell membrane conductivity often increases as a result of the loss of cell viability. This is because cell death often leads to the disintegration of the membrane. Figure 2.6c shows how the cell membrane conductivity affects the Clausius-Mossotti factor. It can be observed that a change in the cell membrane conductivity does not have a significant effect at higher frequencies.

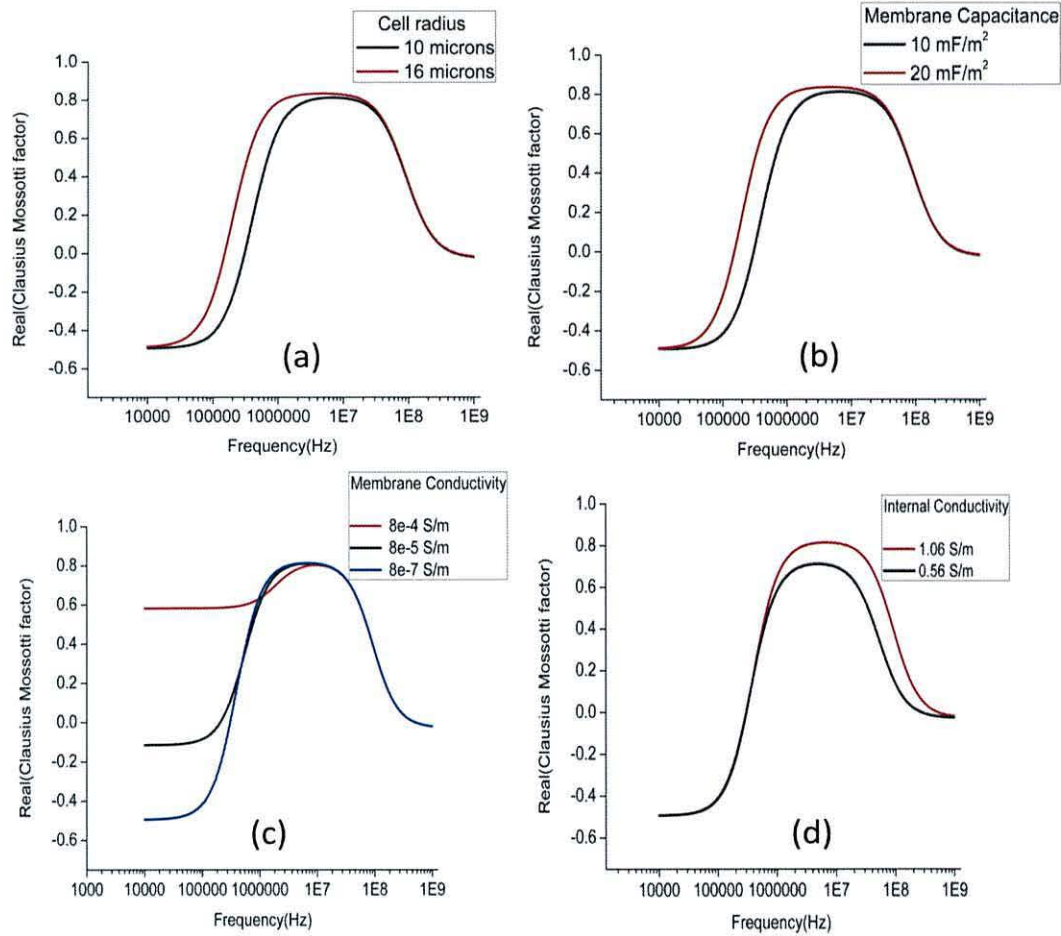


Figure 2.6: Calculated real part of the CM factor of a human T-lymphocyte as a function of frequency for different parameters (a) cell radius (b) membrane capacitance (c) membrane conductivity (d) internal conductivity

Figure 2.6d shows the effect of changing the interior conductivity. It can be seen that as the internal conductivity decreases the positive DEP effect gets stronger and it also exhibits a positive shift in the CM factor at higher frequencies.

Therefore, in summary, under constant suspending medium conditions, the membrane capacitance and the cell radius primarily determine the lower cross-over frequency, whilst the higher frequency effects are dominated by changes in internal conductivity and other smaller membrane dispersions in the interior of the cell.

The example given in figure 2.7 is that of a two shelled model of a yeast cell [12]. In this case a cell wall exists in addition to the cell membrane. In this plot, the effect of

solution conductivity is demonstrated. A shift in the cross-over frequencies towards higher frequencies is the most prominent effect. It is also observed that the solution conductivity does not have a significant effect on the CM factor for frequencies above 100 MHz.

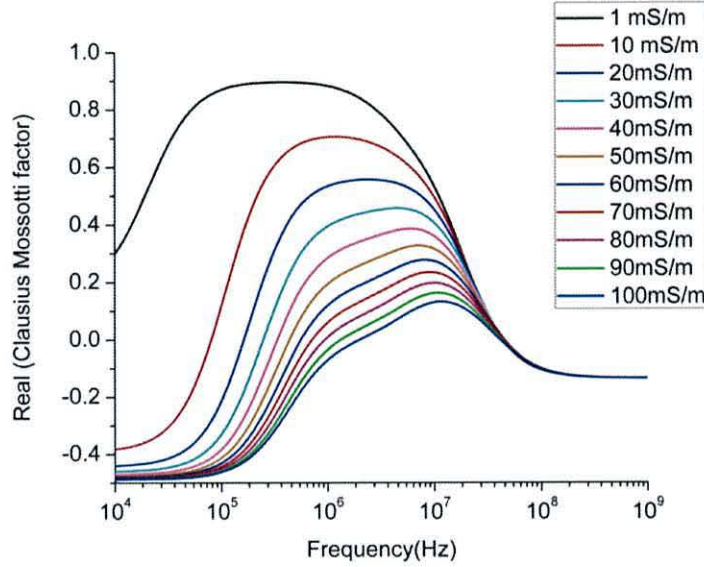


Figure 2.7: Simulated real part of the Clausius-Mossotti factor of yeast cells as a function of frequency for different values of solution conductivity using a two-shelled model.

The frequency response of a viable cell sphere is normally characterized by two cross-over frequencies, corresponding to where the cell appears to be transparent to the applied field and no charges are induced on or within the cell. From equations 2.21 and 2.22, an expression for the cross-over frequency is derived to be

$$f_{cr}^2 = \frac{1}{(2\pi)^2} \frac{(\sigma_p - \sigma_m)(\sigma_p + 2\sigma_m)}{(\varepsilon_p - \varepsilon_m)(\varepsilon_p + 2\varepsilon_m)} \quad (2.33)$$

The lower cross-over frequency is found to mostly depend upon the solution conductivity, the cell radius and the membrane capacitance - whereas the higher cross-over frequency is found to mostly depend upon the properties of the interior of the cell.

2.4 Dipolar Interactions and Chaining in Cell Suspensions Undergoing DEP

In dense particle suspensions undergoing DEP, particles are found to interact with one another. It is inaccurate to treat cells in DEP systems as non-interacting standalone single particles, because, in most DEP experiments some form of cell clustering is observed. There has been some previous work in this area which details the AC frequency and field intensity dependence on the interaction and chaining of particles [18, 19].

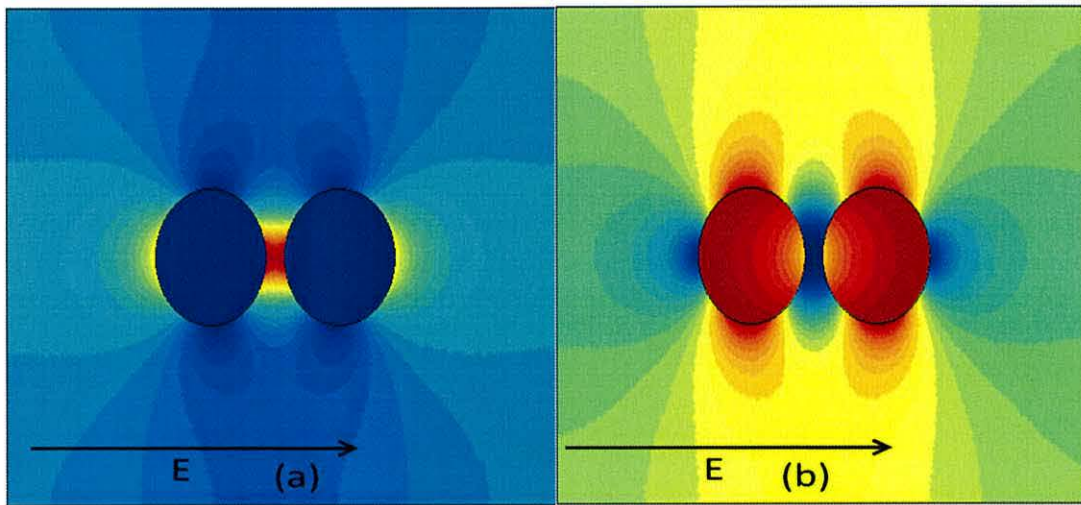


Figure 2.8: The electric field magnitude around the particles (red denotes high electric field intensity and blue denotes weak electric field intensity) (a) Particles are more polarisable than the medium. (b) Particles are less polarisable than the medium.

Two particles along the direction of the uniform electric field is considered. In the first case both the particles are much more polarisable than the surrounding medium as shown in figure 2.8a. The field strength inside the particle is low and also low field strength is observed on either side of each particle. There are high field strengths along the direction of the electric field. Since both the particles experience positive DEP, they will move towards the high field regions.

In the figure 2.8b, both the particles are less polarisable than the suspending medium and hence they will undergo negative DEP. In this case, the high field region is observed on the sides of the particle and regions of low field strength are observed along the direction of the electric field. For two or more particles having the same dielectric characteristics, the most stable particle chaining configuration is to chain along the direction of the electric field and not perpendicular to the field lines.

These phenomena can be explained in terms of the interaction energies between the particles. The interaction energy is given by [19]

$$U = \frac{1}{4\pi\epsilon_m} (4\pi\epsilon_m CM_1 R_1^3)(4\pi\epsilon_m CM_2 R_2^3) \frac{1 - 3\cos^2\theta}{d^3} E_{rms}^2 \quad (2.34)$$

where R_1, R_2 is the radius of particle 1 and 2, d is the separation distance between the two particles, ϵ_m is the permittivity of the medium, E_{rms} is the root mean square value of the electric field and θ is the orientation angle with respect to the field.

In the case of two particles of similar polarisability, the two particles try to achieve a minimum energy configuration by joining together along the field lines. Whereas in the case of two particles of equal and opposite polarisation, the minimum energy configuration is obtained when these particles are aligned perpendicular to the field. This is shown in figure 2.9 for the case of two particles each of radius 5 microns placed in a uniform electric field of magnitude 10^6 V/m separated by distance of 15 microns. The real part of the Clausius-Mossotti factors for the two particles in the different configurations are (0.5, 0.5) and (0.5,-0.5).

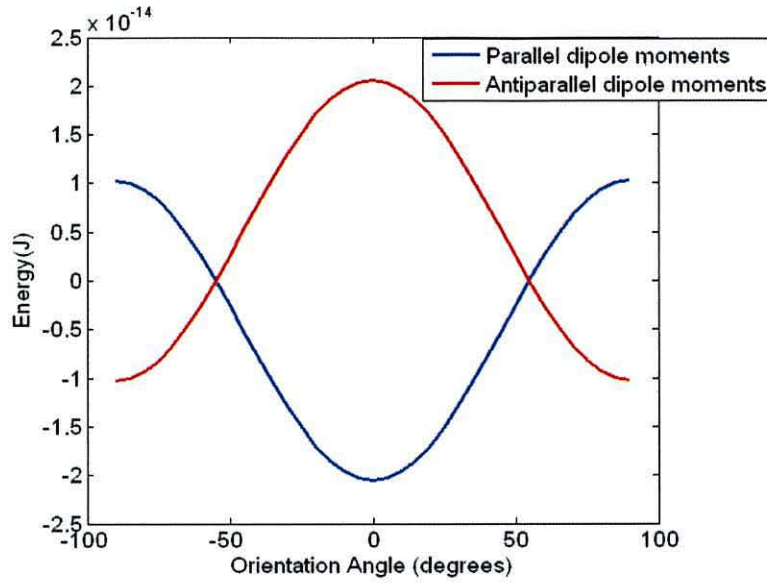


Figure 2.9: Simulation of the effect of orientation angle on the interaction energy for two particles having the same polarisability.

However, particle chaining is not always observed along the electric field lines and this can be explained by both the incompatibility of the electric field lines with the dielectrophoretic force patterns and also by understanding the ratio of the dipolar interaction force to the DEP force. Close to the cross-over frequency particle chaining is rarely observed and this can be explained as follows: as the Clausius-Mossotti factor decreases the ratio mentioned above also decreases and hence the particles have a tendency to be manipulated individually. In sparse particle suspensions it also uncommon to observe particle chaining and this can be explained by the significant decrease in particle interaction force with increasing separation distance between the particles [20].

Figures 2.10 and 2.11, shows 2D simulations and experimental results of particle chaining under both positive and negative DEP conditions, respectively. In the simulations, the surface plot indicates the electric potential where red indicates an electric potential of 1V peak and blue indicates a electric potential of -1V peak. The arrows indicate the relative DEP force and the lines indicate the electric field lines.

For the positive DEP setup, a set of polynomial quadrupole electrodes are energised in the manner shown in figure 2.10. The DEP force is directed towards the electrode edge and the electric field lines extend perpendicular to the edge for a distance of up to 40 microns, allowing stable conditions for particle chaining.

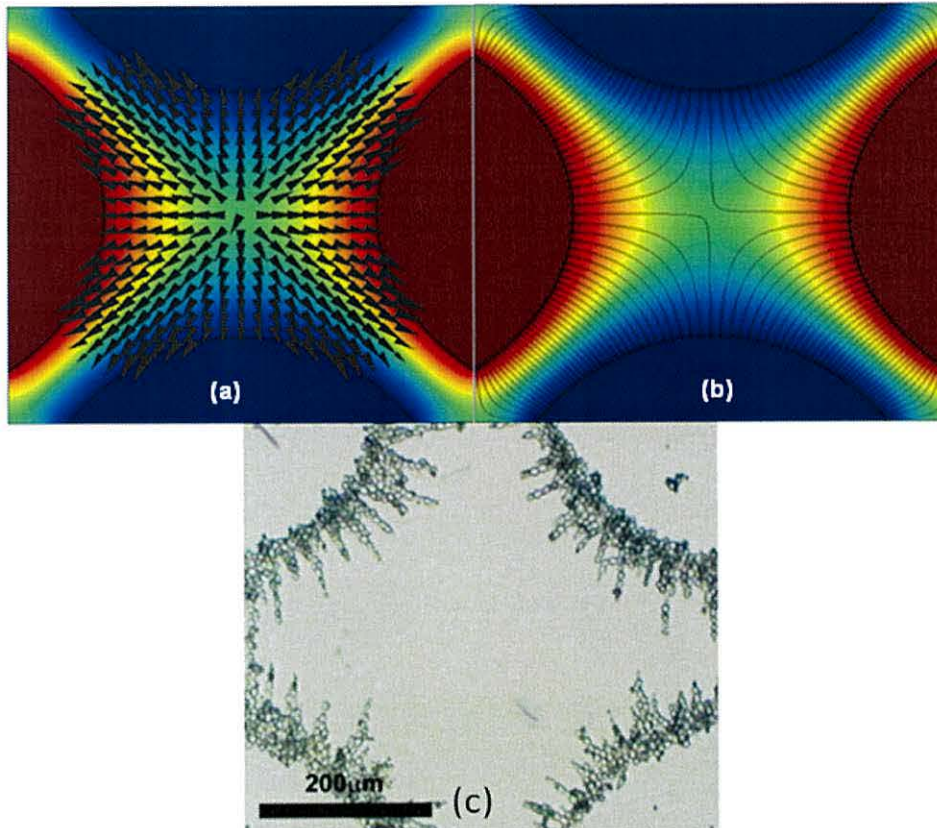


Figure 2.10: Pearl chaining under positive DEP conditions in a polynomial quadrupole geometry electrode (a) Arrows indicate the relative DEP force. (b) Electric field lines (c) Experimental pearl chaining of yeast cells around the electrode edge.

Particle chaining is less commonly observed in cells undergoing negative DEP. This is because for electrode geometries such as the interdigitated electrode geometry, the cells are pushed into the gap due to the dielectrophoretic force pattern, whereas the electric field lines are perpendicular to the electrode layout and hence there is an instability which does not support effective particle chaining.

To demonstrate dipolar chaining under conditions of negative DEP, a quadrupole semicircular electrode geometry is energised in the manner shown by the electric

potential surface plot in figure 2.11. In this case, the DEP force pattern pushes the particles into the centre and then outwards through the electrode gaps. The electric field lines are observed to stretch in a manner conducive to particle chaining and hence chains are rapidly formed.

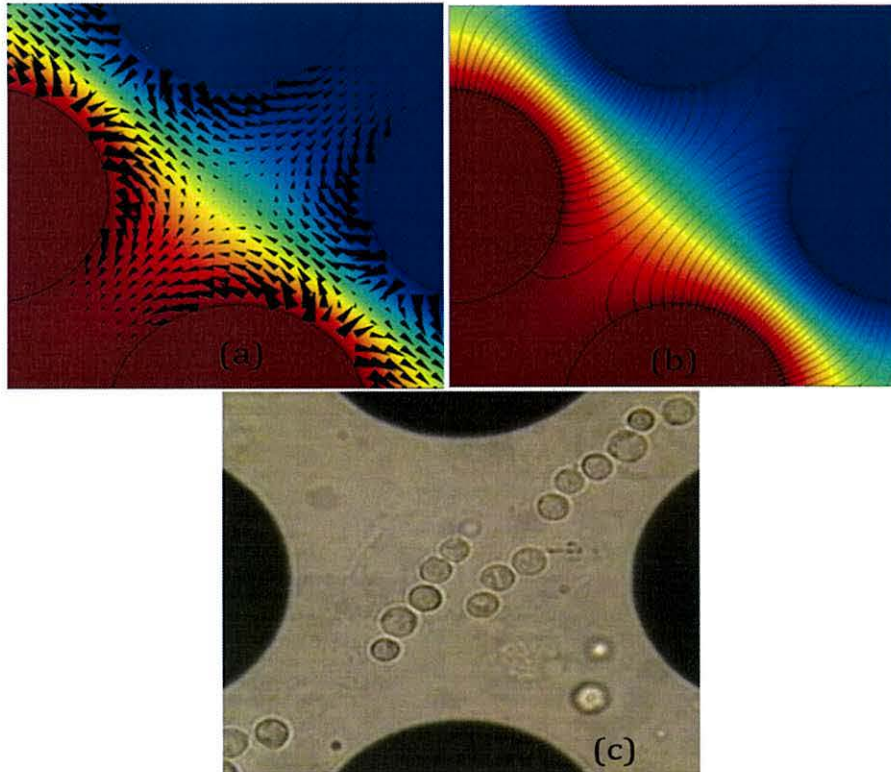


Figure 2.11: Conditions for pearl chaining under negative DEP conditions in a semi- circular quadrupole geometry electrode (a) arrows indicating the relative DEP force (b) the electric field lines (c) experimental pearl chaining of schwannoma cells under conditions of negative DEP

2.5 Fluid Flow in Micro Channels

2.5.1 Navier-Stokes Equation

The biological applications of DEP require the use of fluid as the suspending medium, it is therefore essential to understand fluid behavior in microfluidic devices. The density of the fluid observes the conservation of mass equation which states that the rate of change of mass in an arbitrary volume is equal to the flux of mass through the surface

enclosing the volume. The fluid dynamics for incompressible fluids is governed by the incompressible Navier-Stokes equation. The effect of the viscous drag force in dielectrophoretic microfluidic devices is also discussed in chapter 4.

Incompressible Newtonian fluids are governed by the Navier-Stokes equation [2]

$$\rho_m \frac{\partial \mathbf{u}}{\partial t} + \rho_m (\mathbf{u} \cdot \nabla) \mathbf{u} = -\nabla p + \eta \nabla^2 \mathbf{u} + \mathbf{f} \quad (2.35)$$

where ρ_m is the mass density, p is the pressure, η is the viscosity and \mathbf{f} is the applied body force. The equation can be further simplified by examining the scales of the problem and non dimensionalising the Navier-Stokes equation.

In the non-dimensional form the ratio of the inertial term $\rho_m (\mathbf{u} \cdot \nabla) \mathbf{u}$ to the viscous term $\eta \nabla^2 \mathbf{u}$ gives a factor called the Reynolds number. For a flow speed u , fluid density ρ_m and fluid viscosity η , the Reynolds number Re is given by

$$Re = \frac{\rho_m u l_o}{\eta} \quad (2.36)$$

With the reduction in the size of the channels there is an increase of the surface-to-volume ratio and therefore the viscous term dominates over the inertial regime. For microfluidic applications, the values for $l_o \approx 10^{-4}$ m and $u \approx l_o \approx 10^{-3} - 10^{-5}$ ms⁻¹ and assuming the fluid is water the Reynolds number is of the order of 0.1 to 0.001 and therefore the fluid profile is well within the laminar regime without any presence of turbulence. It can be said from equation 2.36 that decreasing Reynolds number results in the domination of the viscous force component over the inertial force component and hence the fluid travels along smooth trajectories unlike in the case of turbulent flow where the fluid trajectories can be chaotic leading to fluid mixing. Since the viscosity factor dominates in case the applied fluid pressure is halted the fluid flow comes to an immediate stop.

2.5.2 Fluid Effect on a Moving Particle

In a fluidic system, the fluid exerts a drag force on the particle which affects the velocity of the particle. When a particle is moving relative to the fluid, it experiences a force that is proportional to the particle velocity v . For a moving spherical particle the drag force can be given by

$$F_{\eta} = -6\pi\eta r v \quad (2.37)$$

When a particle is suspended in a fluid and is accelerated, it experiences an increasing drag force. For a constant applied force the particle reaches a terminal velocity beyond which it does not accelerate. If the fluid is in motion with a velocity u and there exists an external force on the particle such as the dielectrophoretic force, the drag force experienced by the particle is proportional to its velocity relative to the fluid and this is given by

$$F_{\eta} = 6\pi\eta r(u - v) \quad (2.38)$$

The equation of motion for the particle is given by Newton's second law

$$m \frac{dv}{dt} = F_{DEP} + 6\pi\eta r(u - v) \quad (2.39)$$

If the particle is at rest before application of DEP force, the solution for particle velocity becomes

$$v = \left(\frac{F_{DEP}}{6\pi\eta r} + u \right) \left(1 - e^{-t/(\frac{m}{6\pi\eta r})} \right) \quad (2.40)$$

The exponential term gives the velocity for the particle at times greater than zero. The exponential term describes the acceleration and has a time constant τ

$$\tau = \frac{m}{6\pi\eta r} \quad (2.41)$$

For a biological particle with a diameter of approximately 10 microns the time constant would have a value in micro seconds. The particle is therefore considered to travel at terminal velocity v_T at each calculated instant, and this can be given by

$$v_T = \frac{F_{DEP}}{6\pi\eta r} + u \quad (2.42)$$

2.6 Surface Tension Effects

A distinctive feature of microfluidics is the influence of surface effects such as surface tension and this is primarily due to the large surface to volume ratio on such tiny length scales [21]. This effect can be understood by studying Gibbs free energy G . The Gibbs free energy of a system can be defined as the non-pressure volume work exchanged by the system with its surroundings. The surface tension for an interface is defined as the Gibbs free energy per unit area for fixed pressure and temperature. In order to explain the process, an interface between a liquid and a gas is considered. The bulk liquid forms chemical bonds with the neighboring molecules thus gaining a certain amount of binding energy. A molecule at the surface cannot form as many bonds since there are almost no molecules in the gas. This lack of chemical bonds results in a higher energy for the surface molecules. This energy of the surface is what is observed as surface tension effects.

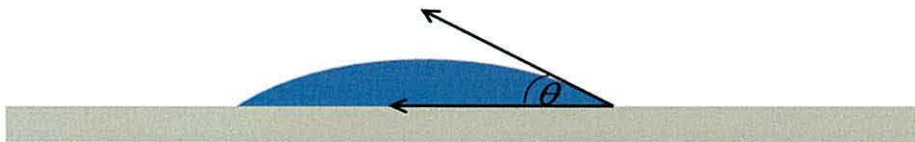


Figure 2.12: Schematic showing the wetting of a substrate with a droplet forming a contact angle θ between the solid-liquid and the liquid-gas interface at the contact line.

One of the important features of a substrate material used for microfluidic applications is its ability to wet the surface of the substrate. If the liquid has a stronger adhesive force to the substrate than a cohesive force between the molecules of the liquid and the wetting of the surface occurs more easily. If the cohesive forces of the liquid molecules are stronger than the adhesive forces the liquid molecules are more strongly attracted to each other than the molecules of the solid surface. One way to estimate

the surface wetting characteristics is to measure the contact angle θ of a drop of liquid placed on the surface of a substrate, shown in figure 2.12.

2.7 AC Electrokinetic Fluid Effects

An understanding of other AC electrokinetic effects such as electrothermal flow and electroosmosis is also necessary because in some cases these fluid forces tend to interfere with dielectrophoretic movement. Non-uniform electric fields used for DEP also results in joule heating, which in turn gives rise to electrothermal forces on the fluid by the variation in the conductivity and permittivity of the suspending medium. AC Electroosmosis is a result of induced charges on the electrode surface in the presence of non-uniform AC electric fields. This results in a force in the double layer on the microelectrodes which leads to fluid motion termed as AC electro-osmosis. These effects compete with the dielectrophoretic forces and therefore the total force acting on the particle is given by the sum of all these effects [2, 22]. The degradation of the DEP effect due to these external fluid forces can be controlled and hence it is essential to understand these phenomena.

2.7.1 Electrothermal Heating Leading to Fluid Flow

The non-uniform electric field generated for DEP applications gives rise to temperature gradients in the suspending medium [22-24]. The temperature gradient leads to the variations in the conductivity and permittivity of the fluid and these gradients in the conductivity and permittivity of a fluid under the influence of an electric field will result in an electrical force in the fluid resulting in fluid motion, shown in figure 2.13.

The joule heating which causes the temperature gradients can be explained by the amount of heat energy that the fluid absorbs and this is given by

$$Q = \sigma |E|^2 \quad (2.43)$$

The time averaged electric force density on the particle due to local heating is given by [23]

$$f_e = -0.5 \left[\left(\frac{\nabla \sigma}{\sigma} + \frac{\nabla \varepsilon}{\varepsilon} \right) \cdot E \frac{\varepsilon E}{1 + \omega^2 \tau^2} + 0.5 |E|^2 \nabla \varepsilon \right] \quad (2.44)$$

where as $\nabla \varepsilon = \left(\frac{\partial \varepsilon}{\partial T} \right) \nabla T$, $\nabla \sigma = \left(\frac{\partial \sigma}{\partial T} \right) \nabla T$, $\nabla^2 T = \sigma E^2$.

The electric force acting on the fluid is frequency dependent and so is the resulting fluid flow. The Coulomb force is dominant at low frequencies and the dielectric force dominates at higher frequencies. The crossover frequency at which the behavior changes from being one force dominated to being the other force dominated occurs when the magnitudes of the two forces are equal to each other.

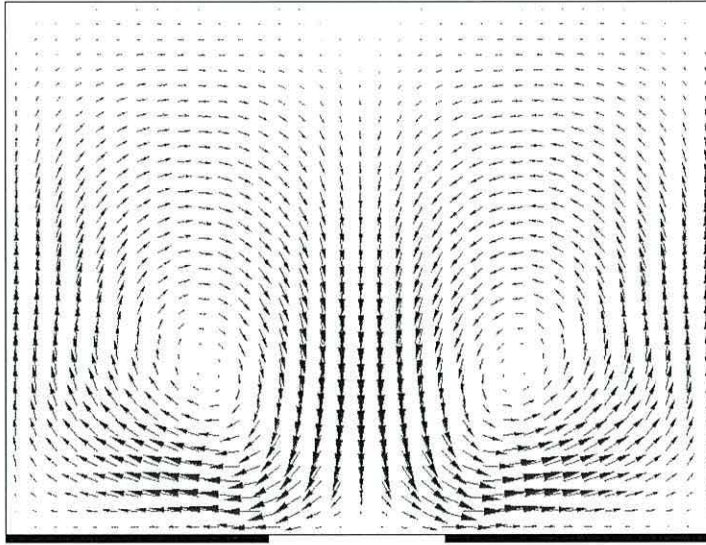


Figure 2.13: Schematic of the electrothermal flow over a two parallel electrode system

2.7.2 AC Electroosmosis

A nanometer layer of charges/ions is induced by an AC electric field at the interfaces of electrolytes and solids and this charge accumulation is frequency dependant [1, 25]. The tangential electrical fields drives ions along the electrode surface which in turn drives the fluid at the electrode surfaces, and this is referred to as AC electroosmosis.

This effect is not very pronounced for frequencies above a 100 kHz, because of the inability of the charges to form a double layer. In AC electroosmosis, the charges in the double layer are induced by AC voltages, and tangential E-fields are a result of the same voltage source. Hence, changes of polarities in charges and field directions are synchronized and cancelled out, maintaining steady fluid motion.

A simplified expression for fluid slip velocity v on the electrode surface is given by the Helmholtz-Smoluchowski relationship [25]

$$v = -\frac{\varepsilon\zeta}{\eta} E_t \quad (2.45)$$

where ε is the permittivity, η is the viscosity of bulk solution, ζ is the zeta potential at the interface between the liquid and the substrate and E_t is the tangential component of electrical field.

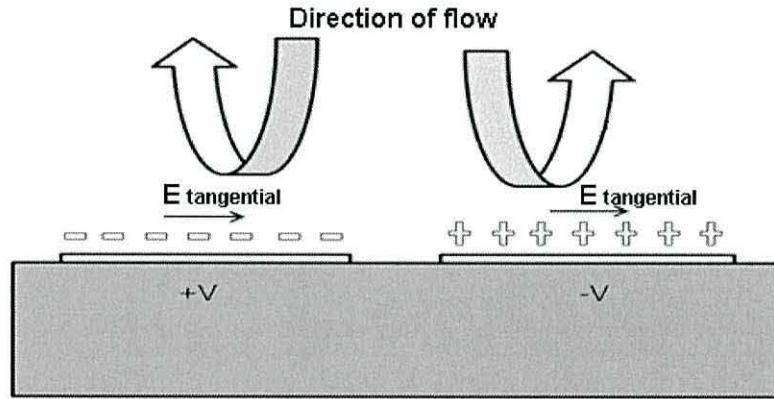


Figure 2.14: Diagram showing the interaction of the tangential field with the double layer to provide fluid movement on two thin parallel electrodes caused by electroosmosis.

2.8 Finite Element Analysis

In order to understand and quantify physical phenomena such as dielectrophoresis, the effect of fluid forces or the interaction of both, it is necessary to solve a set of partial differential equations. Solutions to partial differential equations (PDE's) can be obtained analytically or numerically. Numerical approximations are normally used to

estimate the solution of a set of partial differential equations when the solution cannot be obtained analytically. Complex problems such as fluid dynamics, structural mechanics and electromagnetics require numerical solvers such as the finite difference or finite element method.

The finite difference method is one approach of approximating solutions of PDE's, implemented by discretizing the solving space into a fixed width rectangular grid. This grid method is not very suitable for complex curved geometries. The finite difference method also does not allow for a good approximation of values between the grid points.

The finite element method (FEM) is a more attractive alternative for solving PDE's over a certain system space and it involves dividing the solution space into finite elements [21]. Each element is assigned a set of equations detailing the material properties and the boundary conditions which are then solved as a set of simultaneous equations to predict the object's behaviour. FEM involves the partitioning of the domain into a set of smaller domains called elements. FEM involves representing the solution as a combination of some basis functions over the whole solving space. The Lagrange finite element space is defined by a linear or polynomial function on each mesh element with value 1 in the working node and 0 in all other nodes. The value of the basis function determines the number of working node points and these are distributed within the mesh element. The basis functions are matched at element boundaries to ensure continuity and smoothness. This method is more versatile than the finite difference method as the elements can take shapes such as triangles which are more suited for curved geometries. The mesh elements can have different shapes but commonly triangles are used in the case of a 2D geometry and tetrahedra in the case of a 3D geometry.

A modelling package called COMSOL Multiphysics was used to perform the simulation work. The various steps in the modelling process are detailed below

Geometry definition: The limits for the axis and the grid lines are set. The grid and axis settings help to construct geometry of the exact dimensions required. The geometry can be defined by using boundary or solid modelling to create objects in 2D or 3D. In the case of solid modeling the geometry is defined as a combination of solid objects using Boolean operations like union, intersection, and difference. The common solid modeling shapes like rectangles, circles, blocks, cones, and spheres are directly available in COMSOL Multiphysics. In the case of 3D geometries one can also define the geometries in 2D then extrude them into 3D solids.

Parameter Definition: Select predefined or user defined PDE's. Define material values within each shape such as the permittivity of the medium. Define the polynomial basis functions to be used for interpolation within the element. The boundary conditions are then defined in order to describe how the geometry interacts with the background in which it is set. The boundary conditions that are used generally are the Dirichlet boundary conditions where the value of the function on the boundary is provided or Neumann boundary conditions where the normal derivative is specified.

Coupled Physics: Physics modules are coupled where necessary, for example: modeling of electrothermal flow, the electric field is coupled to the heat transfer module and the fluid flow module.

Mesh geometry: Following the definitions of the various parameters the geometry of the problem space is split up into finite elements in the form of a triangular mesh. The mesh size of geometry must be based on the dimension and design of the geometry that is to be solved. COMSOL allows for the element size and also parameters such as the element growth rate to be set, which effect mesh sizes further away from the boundaries.

Solving the model and Post processing: The type of solver is chosen such as a stationary solver or a time dependant solver. It also allows for only certain domains or certain sets of physics to be solved. The post processing helps to visualize the solution using various different plots such as coloured surfaces, streamlines, contour plots and arrows.

An example follows of the steps involved in the modeling process and the steps involved in improving the accuracy of the solution while solving a simple electric field problem. A 2D electrostatic model of a pin plane electrode system has been used. The appropriate PDE's are chosen by selecting the appropriate application mode in COMSOL. A quasi-static potential field is solved and this is done by solving Laplace's equation.

$$\nabla^2 V = 0 \quad (2.46)$$

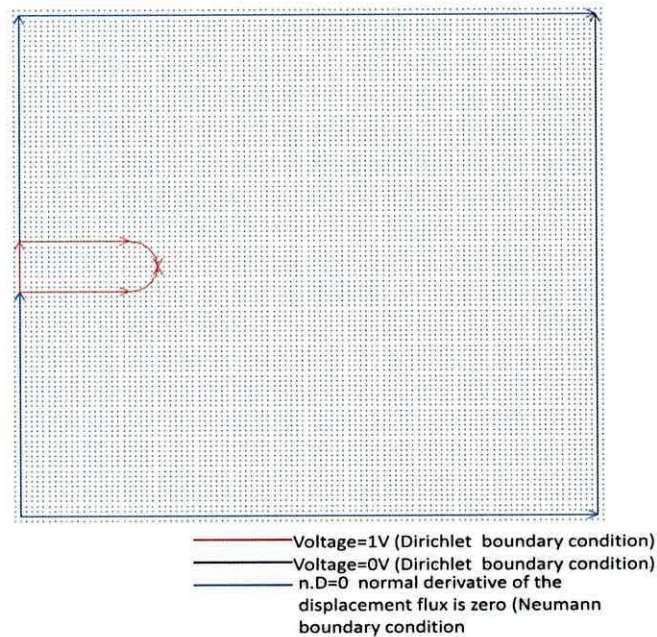


Figure 2.15: Geometry and boundary definitions of the pin-plane electrode system.

At first the geometry and the space over which to solve the electric field is defined. The pin electrode was constructed by performing a simple Boolean union operation between a sphere and a rectangle. The other geometry boundaries were defined as lines. The boundary conditions are zero charge symmetry everywhere except on the electrodes, where a voltage is applied, shown in figure 2.15. The subdomain conditions are defined to include the permittivity of the different sections in the solution space.

After defining the various parameters, the geometry is meshed. In this case, triangular elements within the 2D geometry were used, shown in figure 2.16. The size and number of elements in a finite element model are inversely related. Upon each mesh refinement, every element is divided into four smaller elements. As the number of elements increases, the size of each element must decrease and consequently the accuracy of the model generally increases. The more the number of elements that are used the solution is generally more refined. This is demonstrated in the figure 2.17a. However, element size is not the only criteria to obtain an accurate solution. Just as critically, the element basis functions which define the interpolation polynomials for a set of equally spaced interpolation points must also be set.

The element basis is chosen to be simply the Lagrange interpolation polynomials for a set of equally spaced interpolation points or nodes in the element. The interpolation patterns (p) are normally linear, quadratic or cubic. This is critical to determining the accuracy and higher order smoothness of the solution. The adjoining elements share the position of the nodes on their common edge. This process ensures continuity throughout the solution domain when the elements are combined together. Therefore it is necessary adopt a combination of the element size through mesh refinement and the interpolation patterns in the basis functions to produce an accurate solution.

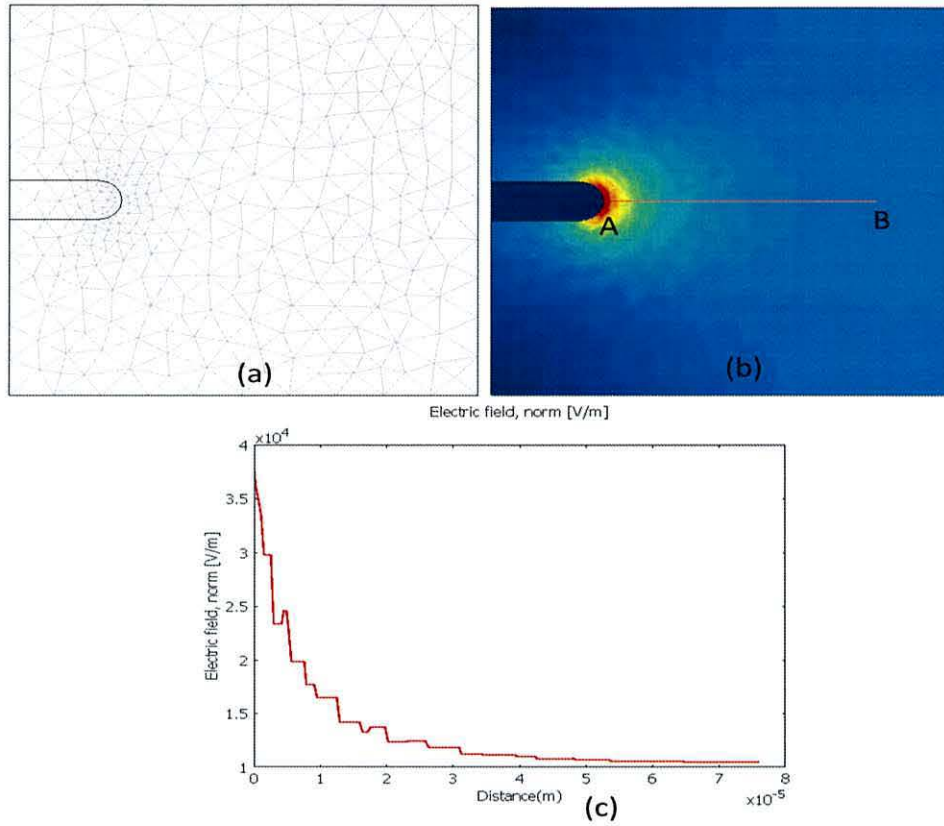


Figure 2.16: (a) Meshed geometry with 607 triangular elements and a linear interpolation. (b) The electric field simulation pattern. (c) The electric field magnitude plotted along line AB.

From figure 2.16 it can be seen that in the case where an adaptive mesh is used, with 607 triangular elements and a linear interpolation basis function with 2 nodes on each element edge, a very rough electric field variation along line AB is obtained, as shown in figure 2.16c.

In order to characterize the effects of increasing the number of elements by means of one extra mesh refinement, a mesh containing 2428 elements again with 2 nodes on each element edge was also considered. The smoothness of the electric field plot as shown in figure 2.17a is observed to improve.

On increasing the number of nodes on each element edge upon keeping the triangular element numbers at 607, the smoothness of the electric field plot shown has increased

considerably as shown in figure 2.17b. This method is more memory intensive than the method of increasing the number of elements in the solution

These two different methods, either independently or in combination must therefore be used appropriately after understanding the problem to be solved as well as the memory constraints and the exact level of accuracy and smoothness required in the finite element solution.

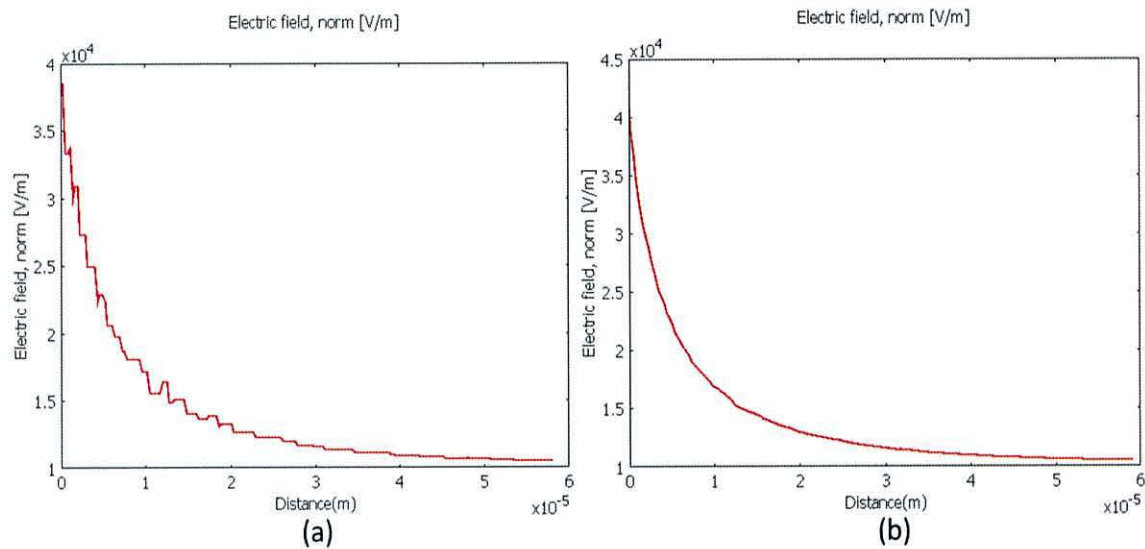


Figure 2.17: (a) The electric field magnitude plotted along line AB for a mesh with 2428 elements with 2 nodes on each element edge. (b) The electric field magnitude plotted along line AB for a mesh with 607 elements and 3 nodes on each element edge.

2.9 References

- 1) Hughes, M.P., 'Nanoelectromechanics in Engineering and Biology', CRC Press LLC, Boca Raton, Florida, 2002
- 2) Morgan, H., and Green, N.G., 'AC Electrokinetics: Colloids and Nanoparticles'. Research Studies Press, Baldock, Hertfordshire, 2002
- 3) Martinsen, O.G., Grimnes, S., Schwan, H.P., 'Interface phenomena and dielectric properties of biological tissue', Encyclopedia of Surface and Colloid Science, pp. 2643-2652
- 4) Pohl, H.A., 'Dielectrophoresis'. , Cambridge Univ. Press, Cambridge, 1978
- 5) Pethig, R., 'Dielectric and electronic properties of biological materials', John Wiley, Chichester, 1979
- 6) Jones, T.B., 'Electromagnetics of Particles', Cambridge University Press, Cambridge, 1995
- 7) Pethig, R., 'Dielectrophoresis of Biological Cells', Encyclopedia of Surface and Colloidal Science, 2nd Edition, Taylor & Francis, New York, 2006, pp.1719-1736
- 8) Jones, T.B., 'Basic theory of dielectrophoresis and electrorotation', Engineering in Medicine and Biology Magazine, IEEE, 2003, 226, pp. 33-42
- 9) Washizu, M., and Jones T.B., 'Multipolar dielectrophoretic force calculation'. J. Electrostat., 1994, 33, pp. 187–198
- 10) Arnold, W.M., Schwan, H.P., and Zimmermann U., 'Surface Conductance and Other Properties of Latex-Particles Measured by Electrorotation'. Journal of Physical Chemistry, 1987, 91, pp. 5093–5098
- 11) Irimajiri, A., Hanai, T., and Inouye, A., 'A dielectric theory of "multi-stratified shell" model with its application to a lymphoma cell', J. Theor. Bio., 1979, 78, pp. 251-269
- 12) Huang, Y., Hölzel, R., Pethig, R., and Wang, X. B., 'Differences in the AC electrodynamics of viable and non-viable yeast cells determined through combined dielectrophoresis and electrorotation studies'. Phys. Med. Biol., 1992, 37, pp. 1499–1517
- 14) Huang, Y., Wang, X.B., Gascoyne, P.R.C., and Becker, F.F., 'Membrane dielectric responses of human T-lymphocytes following mitogenic stimulation', Biochim. Biophys. Acta, 1999, 1417, pp. 51–62
- 14) Becker, F. F., Wang, X.B, Huang, Y., Pethig, R., Vykoukal, J. and Gascoyne, P. R. C., 'Separation of human breast cancer cells from blood by differential dielectric affinity', Proc. Natl Acad. Sci, 1995, 92, pp. 860–864
- 15) Wang, X.J., Becker, F.F., and Gascoyne, P.R.C., 'Membrane dielectric changes indicate induced apoptosis in HL-60 cells more sensitively than surface phosphatidylserine expression or DNA fragmentation', Biochim Biophys Acta: Biomembr, 2002, 1564, pp. 412–420.

- 16) Gascoyne, P.R.C., Wang, W.-B., Huang, Y., and Becker, F.F., 'Dielectrophoretic separation of cancer cells from blood', Industry Applications Conference, 1995. Thirtieth IAS Annual Meeting, IAS '95., Conference Record of the 1995 IEEE , 2, pp.1366-1373
- 17) Huang, Y., Wang, X.B., Becker, F.F., and Gascoyne, P.R.C., 'Membrane changes associated with the temperature-sensitive P85gag-mos-dependent transformation of rat kidney cells as determined by dielectrophoresis and electrorotation', Biochim. Biophys. Acta, 1996, 1282, pp. 76–84
- 18) Fraden, S., Hurd, A.J. and Meyer, R.B., 'Electric-field-induced association of colloidal particles', Phys. Rev. Lett., 1989, 63, pp. 2373–2376
- 19) Giner, V., Sancho, M., Lee, R.S., Martinez, G., and Pethig, R., 'Transverse Dipolar Chaining in Binary Suspensions Induced by RF Fields', J. Phys. D, 1999, 32, pp. 1182-1186
- 20) Kadaksham, J., Singh, P., Aubry, N., 'Dielectrophoresis induced clustering regimes of viable yeast cells', Electrophoresis, 2005, 26, pp. 3738–3744
- 21) Bruus, H., 'Theoretical Microfluidics' Oxford University Press, Oxford, 2007
- 22) Castellanos, A., Ramos, A., González, A., Green N.G., and Morgan, H., 'Electrohydrodynamics and dielectrophoresis in microsystems: scaling laws', Journal of Physics D: Applied Physics, 2003, 36, pp. 2584–2597
- 23) Chen, D.F., and Du, H., 'Simulation studies on electrothermal fluid flow induced in a dielectrophoretic microelectrode system', Journal of Micromechanics and Microengineering, 2006, 16, pp. 2411–2419
- 24) Green, N.G., Ramos, A., González, A., Castellanos, A., and Morgan, H., 'Electrothermally induced fluid flow on microelectrodes', Journal of Electrostatics, 2001, 53, pp. 71–87
- 25) Zhou, H., White, L.R. and Tilton, R.D., 'Lateral separation of colloids or cells by dielectrophoresis augmented by AC electroosmosis', Journal of Colloid and Interface Science, 2005, 285, pp. 179–191

Chapter 3

Controlling Cell Destruction using Dielectrophoretic Forces

3.1 Introduction

The work performed for this chapter was directed towards identifying and theoretically quantifying how the AC voltage frequency and magnitude can be controlled to either minimise or enhance the number of cells destroyed during DEP experiments on cells.

The possibility that, under certain conditions, cells may be irreversibly damaged as a result of exposure to DEP forces is well known to workers in the field, but is often not reported. The desired objective in many DEP experiments is to use radio-frequency electric fields to selectively isolate, concentrate, or purify target bioparticles from prepared or natural fluid suspensions. Examples include the isolation of cancer cells, fetal cells, stem cells or bacteria from blood for further analysis or potential therapeutic purposes. Maintaining cell viability is an important objective in such cases. In previous studies at Bangor, the frequency and voltage of the applied electrical signals were programmed to avoid regimes where cell damage had been observed [1]. However, for other envisaged applications of DEP, as for example to facilitate the release of proteins or DNA from target cells, utilizing such frequency-voltage regimes to achieve selective cell destruction may be a desired objective.

DEP-induced cell damage can arise from at least three main sources, namely effects associated with the cells being suspended in a non-physiological medium, stress induced by the applied electric field, and shear stresses associated with fluid flow. Workers in the field are now competent in their choice of cell suspending media and

applied signal voltages, so that under gentle DEP conditions cell viability can readily be maintained. For example, the viability of erythrocytes separated from leukemia cells has been verified using trypan blue dye [2] and CD34+ cells have been successfully cultured following their DEP enrichment from bone marrow and peripheral stem cell harvests [3]. Fibroblasts can be successfully cultivated, without significant change in their viability, motility, anchorage or cell-cycle time, when exposed to DEP fields continuously over a period of three days [4]. Although very small increases were observed in the stress-related gene c-fos expression levels for glioma and neuroblastoma cells separated by DEP, subsequent culturing experiments demonstrated that there were no effects on cell growth [5]. The highest reported fluid flow rate for DEP cell separation appears to be 2.5 mL/min [6]. Because of the relatively small dimensions of a typical DEP separation chamber, this flow rate is well within the limits for laminar flow and corresponds to a shear stress exerted on the cells of around 0.3 N/m^2 . This is well below the shear stress of 150 N/m^2 required to damage erythrocytes [7] or of 20 N/m^2 for T cells [8].

Cell membranes can also be disrupted by forced oscillation at frequencies greater than around 10 kHz, and this is the basis for using high-power sonication to disintegrate cells. Cell-destruction by DEP is more subtle, and is primarily related to a field-induced breakdown of the physical integrity of the plasma membrane, as evidenced by the fact that the internal structure of the cell appears (under phase-contrast microscopy) to remain intact for some time and is even manipulable by DEP [9]. A related topic is electroporation (also called electropermeabilization) of cells, which is typically achieved by subjecting cells to electric pulses of field strengths ranging from around 5 MV/m (for microsecond pulses) down to 0.1 MV/m (for millisecond pulses) [10]. Field-frequency maps have also been produced of the observed probability of AC electromediated cell bursting [11],

In this work, analyses were made of the conditions, in terms of the strength and frequency of the applied AC field, under which two different cell types (human T-cells and HL60 leukemia cells) were observed to burst during routine DEP experiments. This analysis provided insights into the main factors that can be controlled to either minimize or to achieve selected cell destruction using dielectrophoresis.

3.2 Theory

The total force, per unit volume, acting on a dielectric particle subjected to an external electric field is given by the Maxwell stress tensor to determine the time-average mechanical forces and torques (tensions acting along field lines and pressures acting perpendicular to them) exerted by an electric field on the surface and within the body of a particle [12, 15]. This method involves determining difficult integrals that incorporate pressure-like variables difficult to test experimentally, so that for most practical applications the Maxwell stress tensor formulation is not ‘user friendly’. As detailed in Chapter 2, the effective dipole method gives the same results as the more rigorous Maxwell stress tensor method, and has the advantage that it uses simple concepts and relatively straightforward analyses [16].

The time varying sinusoidal electric potential used in our experiments can be written as $V_{peak} \sin(\omega t)$. The time averaged magnitude of the DEP force can be written using the magnitude of the electric field. It is given by

$$F_{DEPx} = \pi \epsilon_m R^3 \text{Re}[CM] \frac{\partial}{\partial x} |E|^2, F_{DEPy} = \pi \epsilon_m R^3 \text{Re}[CM] \frac{\partial}{\partial y} |E|^2 \quad (3.1)$$

$$F_{DEPz} = \pi \epsilon_m R^3 \text{Re}[CM] \frac{\partial}{\partial z} |E|^2 \quad (3.2)$$

where R is the radius of the cell, ϵ_m is the absolute permittivity of the medium, E is the electric field and CM is the Clausius-Mossotti factor.

An electric field across a cell leads to a voltage drop across the membrane, shown in figure 3.1. When a certain voltage is exceeded, it results in a sometimes reversible or irreversible breakdown of the plasma membrane. The reason a relatively weak DEP field can cause electrical damage to a cell is because the field is enlarged because of a potential drop induced across an extremely thin cell membrane. The DC transmembrane voltage can be simplified to the form [18]

$$E_m = 1.5(R/d)E \cos \theta \quad (3.3)$$

where R is the cell radius, E is the external field strength and θ is the polar angle with respect to the field direction.

In a sinusoidal time-varying electric field there is also a voltage drop across the plasma membrane. In the case of a time varying electric field these effects are frequency dependant since the cell membrane acts as a capacitor between the interior and exterior of the cell.

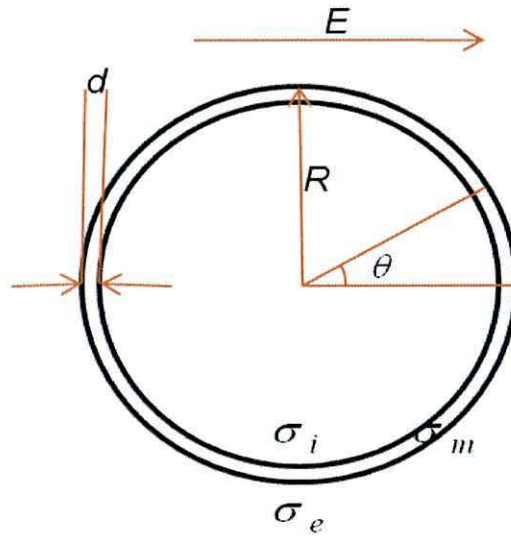


Figure 3.1: Model of a spherical cell with radius of R , enclosed by a membrane of uniform thickness d . The external electric field is denoted as E and θ is the polar angle with respect to the field direction. The Conductivities of the fluid in the cytoplasm, membrane and the extracellular medium are denoted as σ_i , σ_m and σ_e respectively.

For a model spherical cell the frequency dependence of the field E_m acting across the membrane is given by [18, 19]

$$E_m(\omega, \theta) = \frac{1.5(R/d)|E|\cos\theta}{1 + j\omega\tau} \quad (3.4)$$

The factor R/d is the ratio of the cell radius R to the membrane thickness d (ca. 5 nm) and θ is the polar angle with respect to the field direction. The time constant τ is given by:

$$\tau = \frac{RC_m}{\frac{2\sigma_i\sigma_e}{\sigma_i + 2\sigma_e} + \frac{R\sigma_m}{d}} \quad (3.5)$$

where σ_i , σ_m , and σ_e are the conductivities of the cell interior (cytoplasm), cell membrane and extracellular medium, respectively. C_m is the membrane capacitance whose value is principally determined by the morphology of the cell in terms of the presence of microvilli, blebs or membrane folds, for example, and to a good approximation can be determined experimentally from the expression [20]:

$$C_m = \frac{\sqrt{2}}{2\pi R f_{cr}} \sigma_e \quad (3.6)$$

In this equation, f_{cr} is the frequency (the so-called DEP cross-over frequency) where the cell exhibits a transition from negative to positive DEP.

The magnitude of the membrane field in equation 3.4 can be written as

$$|E_m(\omega, \theta)| = \frac{1.5(R/d)|E|\cos\theta}{\sqrt{1 + (\omega\tau)^2}} \quad (3.7)$$

Equation 3.7 predicts that at low frequencies ($\omega\tau < 1$) the field acting across a cell membrane E_m can exceed the applied field E by a factor of 10^3 or greater, depending on cell size.

3.3 Experimental

3.3.1 Cell Samples

Human T lymphocytes (Jurkat E6-1) and leukemia cells (HL60) were obtained from the American Type Culture Collection (ATCC: TIB-152) and the European Collection of Cell Cultures (ECACC: 85011431), respectively. The T cells were grown in RPMI media containing Modified RPMI-1640 (ATCC) supplemented with 10% fetal bovine serum (ATCC), 100 U/mL penicillin, and 100 μ g/ml streptomycin (Gibco/BRL). The HL60 cells were grown in RPMI-1640 media (Sigma) supplemented with 10% fetal bovine serum (Sigma), 1 mM glutamine and 20 mM Hepes buffer (Sigma). A humidified incubator was used, and maintained at 37°C, with 5% CO₂, 95% air.

Immediately before the DEP experiments, the cells were washed twice with 10 mL of an isotonic low conductivity media containing 8.6% w/w sucrose, 0.3% w/w dextrose, and 1.0 mg/mL BSA (Sigma), pH 7.4. The conductivity of this media was adjusted to 40 mS/m at 25°C, by adding modified Eagle's minimum essential media (Sigma) at a ratio of about 40:1, and using a YSI 3200 conductivity instrument with an Orion 018012 conductivity flow cell. After washing, the cells were suspended in the 40 mS/m media. The osmolality of the cell suspensions remained near 296 mmol/kg, as determined using a Vapro 5520 vapor pressure osmometer. The osmolality and conductivity of the cell suspensions were checked before and after each DEP experiment.

3.3.2 Cell Bursting Observations and Electric Field Simulations

Two microelectrode designs were employed in the experiments, namely the interdigitated-castellated and quadrupolar (polynomial) geometries shown in figure 3.2. The interdigitated electrodes were fabricated with a characteristic dimension of 80 μ m defining the castellation geometry [21], and for the quadrupole design [22] the distance

between opposing electrode tips was $400\text{ }\mu\text{m}$. The electrode material was gold, 70 nm thick, vacuum evaporated onto a 5 nm thick seed layer of chromium on a glass microscope slide substrate. Further details of these electrode designs, their fabrication, and how they are used for DEP experiments, have been given elsewhere [21, 22].

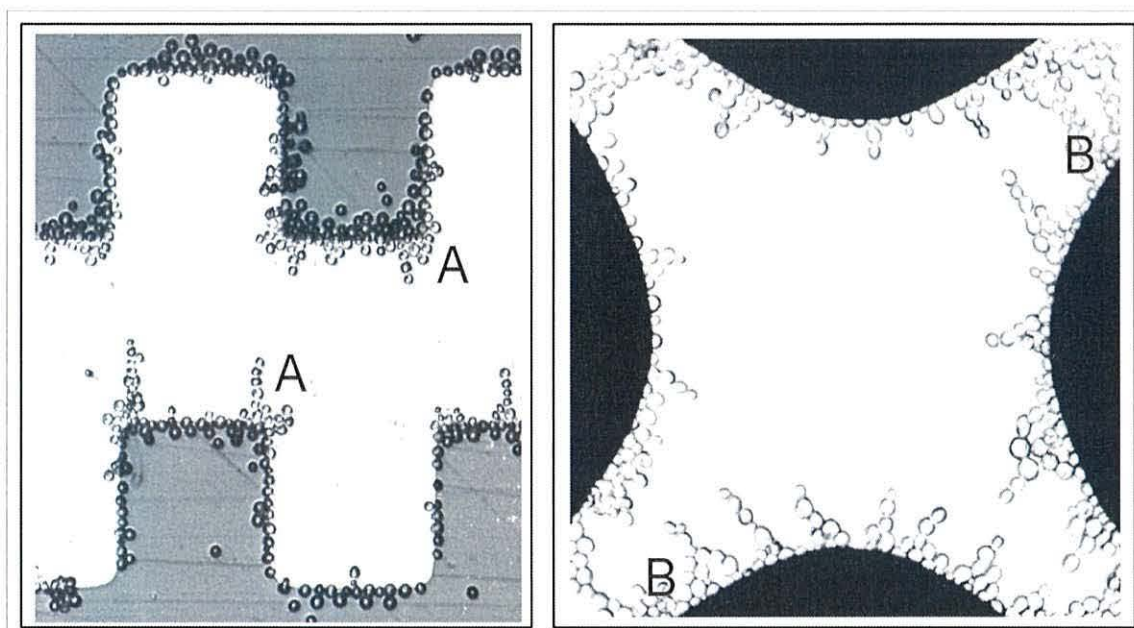


Figure 3.2: The interdigitated and quadrupole electrodes used in these studies are shown on the left and right, respectively. The characteristic dimension defining the interdigitated castellations was $80\text{ }\mu\text{m}$, and the distance between opposing quadrupole electrode tips was $400\text{ }\mu\text{m}$. Cells are shown being attracted to the electrode edges under the influence of positive DEP, cell bursts were events were most common in regions such as those marked A and B.

The data collected for cell bursting events were obtained during experiments performed primarily to characterize the DEP properties of T cells and HL60 cells. The results obtained for the T cells have been reported elsewhere [20] and during the course of these experiments approximately 5% of the cells burst on approaching the (polynomial design) electrode edges under the influence of a positive DEP force. In these experiments the location of each cell could be continuously tracked, and a value for the diameter of each cell could be determined to within $\pm 0.25\text{ }\mu\text{m}$ [20]. The observations made of the location of the cells when they burst, and of the magnitude and frequency of the applied AC voltages, constitute the bulk of the data presented in this paper. Cell

bursting events for a smaller number of T cells were also observed using the interdigitated electrode geometry. The data collected for the HL60 cells were all made using interdigitated electrodes, and in these experiments the locations of the cells and their diameters ($\pm 0.5 \mu\text{m}$) were determined using a simple video imaging method. Cell bursting was observed to occur most often (but not always) in the inter-electrode regions marked 'A' and 'B' in figure 3.2, for the interdigitated and quadrupolar electrodes, respectively.

The magnitudes of the local electric fields imposed on the cells at the time of their observed bursting were deduced from field colour maps shown in figures 3.3 and 3.4. The electric field colour maps were obtained using COMSOL Multiphysics, for a 1 Volt (peak) signal applied to the electrodes.

A numerical approach was employed in this work to calculate the electric field. Using this approach the magnitudes of the electric field are obtained from the electrical potential which in turn is defined by the boundary conditions on the electrode surface. In our simulation an electrostatic or quasi-static approximation was used since this approximation is valid for frequencies and electrode dimensions used for common DEP applications. Using this assumption, Maxwell's equations reduces to

$$\nabla \times \mathbf{E} = 0 \quad (3.8)$$

$$\nabla \cdot \mathbf{D} = \rho, \mathbf{D} = \varepsilon \mathbf{E} \quad (3.9)$$

where E is the electric field intensity, D is the electric flux density, ρ is the space charge density, ε is the dielectric permittivity of the material. The electric field intensity can be defined as the negative gradient of the electric scalar potential V . By substituting for the electric field in equation 3.9, we obtain Poisson's scalar equation

$$\nabla \cdot (\varepsilon_0 \varepsilon_r \nabla V) = \rho \quad (3.10)$$

In our case the permittivity is constant since our medium is a homogeneous dielectric and it is also charge free ($\rho = 0$) and hence equation 3.10 can be further reduced to Laplace's equation

$$\nabla^2 V = 0 \quad (3.11)$$

These assumptions allow a time-dependent to be numerically solved as a static problem. All the simulations have been performed considering it is a static case of 1V (peak).

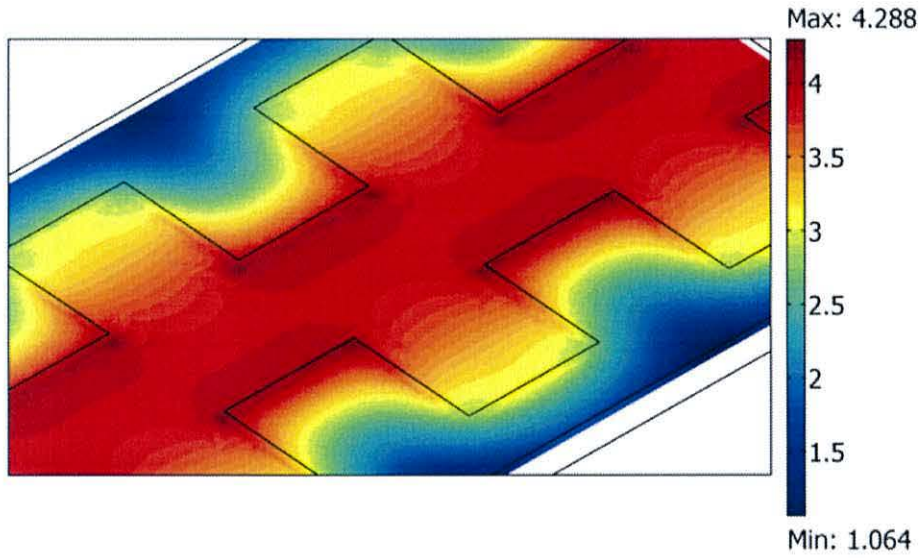


Figure 3.3: Electric field surface plot (V/m, \log_{10} scale) for an interdigitated castellated electrode system energized at 1 V (peak).

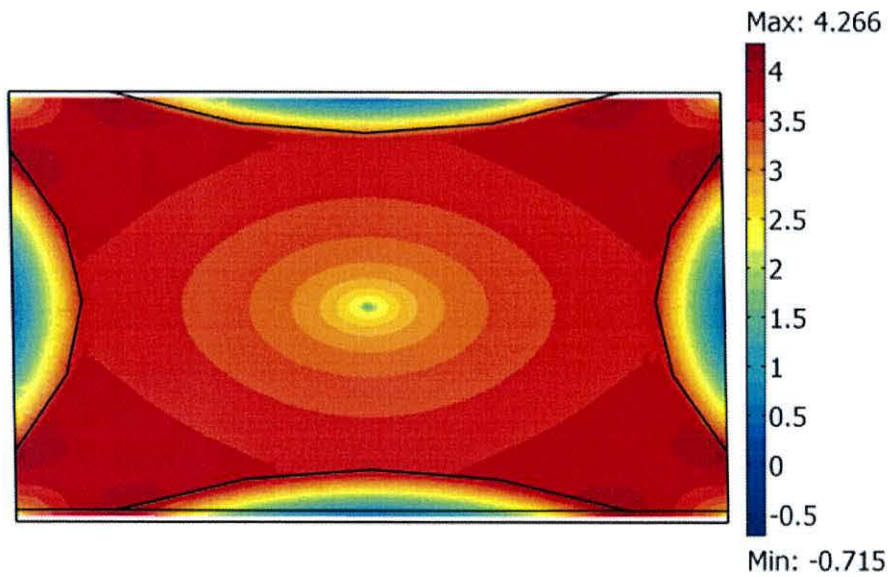


Figure 3.4: Electric field surface plot (V/m, \log_{10} scale) for a polynomial quadrupole electrode system energized at 1 V (peak).

Most of the experiments were performed with an applied AC sinusoidal voltage in the range 2 V to 6 V (peak), and simple linear scaling of the colour values given in figures 3.3 and 3.4 were adopted to accommodate these different voltages. One experiment was performed to induce increased numbers of HL60 cell bursting events, by increasing the interdigitated electrode voltage up to 12 V (peak).

3.4 Results

The cell bursting events, in terms of the local fields experienced by the cells and the frequencies of the applied voltages, are shown in figure 3.5. HL60 cell bursting events for the experiments where the voltage was increased up to 12 V (peak) are not included in figure 3.5 (but see figure 3.7).

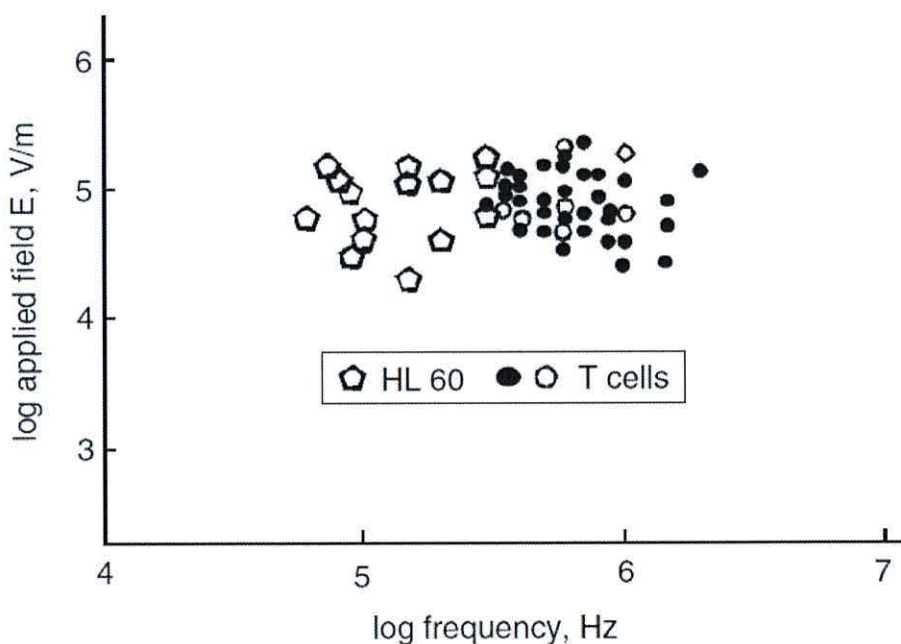


Figure 3.5: Values of the local field and voltage signal frequency at which HL60 and T cells were observed to burst in a suspending electrolyte of conductivity 40 mS/m. The HL60 data points were obtained using the interdigitated electrode design. Both quadrupole (filled circles) and interdigitated (open circles) electrodes were used for the T cell studies.

The data points for the HL60 and T cells in figure 3.5 can be seen to fall into fairly distinct field-frequency windows. The fact that the results obtained for the T cells did

not depend on whether polynomial or interdigitated electrodes were employed indicates that difference in cell type, rather than choice of electrode geometry, determined the different experimental parameters observed for cell bursting.

The data of figures 3.5 has been used to produce figure 3.6, to show values of the membrane field generated parallel to the applied field (i.e., $\theta = 0$) in each cell at the instant of their bursting. These calculations employed equation 3.7 and required the value of the cell radius (which was measured in the experiments) as well as the membrane capacitance C_m to determine the time constant τ given by equation 3.5. For the T cells, the value for C_m was taken as the average value 13.24 mF/m^2 determined [20] for the large number (> 600) of cells that did not burst during the experiments. In equation 3.5 the experimental value of 40 mS/m was used for the conductivity σ_e of the external suspending medium, and values of 0.7 S/m and $5 \times 10^{-7} \text{ S/m}$ were assumed for the conductivities σ_i and σ_m of the cell interior and membrane, respectively. The average cell radius was taken as $5.2 \text{ }\mu\text{m}$ [20], to give $\tau = 9.5 \times 10^{-7} \text{ s}$. for the time constant of the T cells. For the HL60 cells the value for C_m was obtained from measurement of the cross-over frequency f_{cr} for 90 cells that did not burst. Observed values for f_{cr} ranged from 57 kHz to 93 kHz , and gave an average value close to 75 kHz . The radii of the HL60 cells were determined to range from 6.0 to $7.5 \text{ }\mu\text{m}$ ($\pm 0.25 \text{ }\mu\text{m}$) with an average value close to $6.75 \text{ }\mu\text{m}$. This gives a C_m value of 17.8 mF/m^2 for the HL60 cells, and a corresponding time constant value $\tau = 1.66 \times 10^{-6} \text{ s}$.

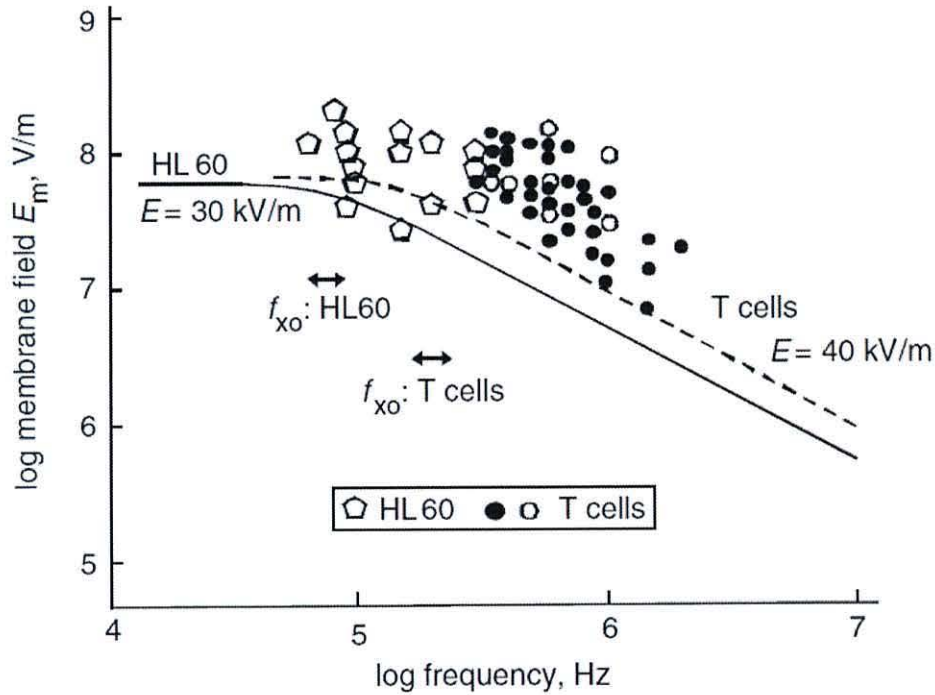


Figure 3.6: Values obtained from equation 3.7, using the field-frequency data given in figure 3.5, for the induced field membrane at the time of cell bursting. Also shown are the DEP cross-over frequency (f_{cr}) range values measured for HL60 and T cells that did not burst. The solid curve shows how the membrane field varies with frequency for the HL60 cells for an applied local field of 30 kV/m and a suspending medium conductivity of 40 mS/m. The dotted line gives the same information for T cells in a local field of 40 kV/m.

The average radii and time constant values ($5.2 \mu\text{m}$, $9.5 \times 10^{-7} \text{ s}$; $6.75 \mu\text{m}$, $1.66 \times 10^{-6} \text{ s}$, for the T and HL60 cells, respectively) were used in equation 3.7 to create the curves drawn in figure 3.6 to show how the membrane field generated parallel to the applied field varies as a function of frequency. These curves are plotted in figure 3.6 for values of external field of 30 kV/m and 40 kV/m for the HL60 and T cells, respectively. The cross-over frequency ranges, where cells exhibited a change from negative to positive DEP with increasing frequency, are also shown in figure 3.6 for the HL60 cells ($f_{cr} \sim 60\text{-}90 \text{ kHz}$) and T cells ($f_{cr} \sim 110\text{-}190 \text{ kHz}$).

3.5 Discussions and Conclusions

The data shown in figure 3.5 indicate that in our DEP experiments a small number ($\sim 5\%$) of cells in suspension were induced to burst if they were directed by positive DEP towards regions at the electrode edges where the local sinusoidal fields exceeded a value of about 30 kV/m. For cells suspended in an isotonic electrolyte of conductivity 40 mS/m and with applied AC voltages between 1V and 6 V (peak), very few cell bursting events were observed in the frequency range from 10 kHz up to the cross-over frequency f_{cr} where the cells made the transition from negative to positive DEP. We assume that in this lower frequency range the cells were directed away from the electrode edges and were never subjected to field stresses greater than 30 kV/m.

From figure 3.6 the critical membrane field for the onset of cell destruction for both the HL60 and T cells is of the order 10^8 V/m for frequencies just slightly above their respective f_{cr} cross-over frequencies, and progressively drops (to a value of the order 10^7 V/m for T cells) as the frequency is raised above f_{cr} . This suggests that a combination of stresses induced by both the increase of membrane field stress and the DEP force acting on the cell leads to cell destruction. At frequencies just above the cross-over frequency f_{cr} it is common in DEP experiments to observe cells spinning at electrode edges under the influence of an induced rotational torque. Such behaviour can result in significant shear forces on the cell membrane, resulting in cell damage [1]. Above a certain frequency, however, where the membrane field falls below 10^7 V/m, the DEP force acting alone is not sufficient to initiate cell destruction. A previous report [11] has described unpublished work to show that different cell types have characteristically different susceptibilities to destruction by AC fields. Although the experimental details of this earlier work are not provided, some interesting comparisons can be made with our work presented here.

As shown in figure 3.6, T cells and breast cancer cells subjected to AC field exhibited maximum cell damage at frequencies around 2 MHz and 200 kHz, respectively [11]. This mirrors the different field-frequency windows for cell destruction of HL60 and T cells shown in figures 3.5 and 3.6, and suggests that in this earlier work [11] the applied fields might have been highly non-uniform and the resulting DEP forces could have contributed to the overall stresses acting on the cells. However, as shown in figure 3.7, the number of cell bursting events was much higher than for our DEP work, with 40 to 100% of the total cells typically being destroyed. This suggests that finer control of electromediated cell bursting can be achieved using DEP fields generated by microelectrode arrays, especially if they are specifically designed to create very localized high field regions. Also, as shown in figure 3.7, in the earlier work [11] the cell bursting probability reached a peak value and then decreased with increasing applied voltage. Without the experimental details it is difficult to understand the reason for this effect, but a possible cause could be an increase of the surrounding medium conductivity as a result of the release of cytoplasm electrolyte from the large number of bursting cells.

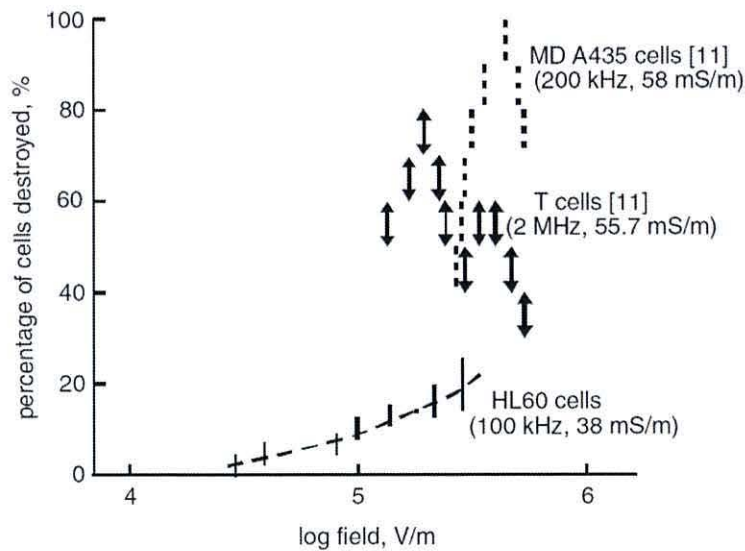


Figure 3.7: Results extracted from the report [11] of the electromediated bursting of T cells and breast cancer cells (MDA-MB-435) are shown with our cell bursting data for HL60 cells. The conductivities of the suspending media are given, and the AC frequency values cited correspond to those where cell bursting was most probable for each cell type.

As a general guide, it appears that to minimize cell destruction the possibility of cells being exposed to fields above 30-40 kV/m should be avoided, especially in the half-decade frequency range immediately above the DEP cross-over frequency where the induced membrane field has yet to fall off significantly in magnitude. Minimizing cell damage could be achieved by 'masking' the electrode regions marked 'A' and 'B' in figure 3.2 with an insulating oxide or polymer film, for example. The location of this frequency window, for a fixed medium conductivity, is defined by the size, morphology (i.e., C_m value) and dielectric properties of a cell type. So, alternatively, this field-frequency window can be exploited to selectively destroy specific cell types in a cell mixture. For example, for a mixture of HL60 and Jurkat T cells, either the HL60 or T cells could be selectively destroyed by applying large AC signals at a frequency of either 100 kHz or 1 MHz, respectively.

The work reported here employed cell suspending media of conductivity near 40 mS/m, but inspection of equations 3.5 and 3.6 indicates that our conclusions will also hold for other values of the medium conductivity. For intact cell membranes, the membrane conductivity σ_m is so small that equation 3.5 can to a good approximation be given as:

$$\tau \approx \frac{RC_m(\sigma_i + 2\sigma_e)}{2\sigma_i\sigma_e} \quad (3.12)$$

If we define $f_{mf} = 1/(2\pi\tau)$ as the frequency where the absolute value of the induced membrane field falls off by a factor of $1/\sqrt{2}$ from its maximum value given by equation 3.7 then on substituting for C_m in equations 3.5 and 3.6 we obtain from equation 3.12 the result:

$$f_{cr} = \frac{f_{mf}}{\sqrt{2}} \left(1 + \frac{2\sigma_e}{\sigma_i} \right) \quad (3.13)$$

Equation 3.13 teaches that the close relationships between the DEP cross-over frequency and the fall in membrane fields shown in figure 3.6 can be expected to hold for the range (1mS/m – 200 mS/m) of medium conductivities commonly employed in DEP experiments on cells.

3.6 References

- 1) Pethig, R., Talary, M.S., and Lee, R.S., 'Enhancing traveling-wave dielectrophoresis with signal superposition', *IEEE Eng. Med. Biol. Mag.* 2003, 22(6), pp. 43-50
- 2) Becker, F.F., Wang, X.B., Huang, Y., Pethig, R., Vykoukal J., and Gascoyne, P.R.C., 'The removal of human leukaemia cells from blood using interdigitated microelectrodes', *J. Phys. D: Appl. Phys.* 1994, 27, pp. 2659-2662
- 3) Stephens, M., Talary, M.S., Pethig, R., Burnett, A.K., Mills, K.I., 'The dielectrophoresis enrichment of CD34⁺ cells from peripheral stem cell harvests', *Bone Marrow Transplant* 1996, 18, pp. 777-782
- 4) Fuhr, G., Glasser, H., Müller, T., and Schnelle, T., 'Cell manipulation and cultivation under a.c. electric field influence in highly conductive culture media', *Biochim. Biophys. Acta* 1994, 1201(3), pp. 353-360
- 5) Huang, Y., Joo, S., Duhon, M., Heller, M., Wallace, B., and Xu, X., 'Dielectrophoretic cell separation and gene expression profiling on microelectronic chip arrays', *Anal. Chem.* 2002, 74(14), pp. 3362-3371
- 6) Marx, G.H., and Pethig, R., 'Dielectrophoretic separation of cells: Continuous separation', *Biotechnol. Bioeng.* 1995, 45, pp. 337-343
- 7) Leverett, L.B., Hellums, L. D., Alfrey C.P., and Lynch, E.C., 'Red blood cell damage by shear stress', *Biophys. J.*, 1972, 12, pp. 257-273
- 8) Chittur, K. K., McIntire, L. V., and Rich, R. R., 'Shear stress effects on human T cell function', *Biotechnol. Prog.* 1988, 4(1), pp. 89-93
- 9) Gascoyne, P.R.C., Pethig, R., Burt J.P.H., and Becker, F.F., 'Membrane changes accompanying the induced differentiation of Friend murine erythroleukemia cells studied by dielectrophoresis', *Biochim. Biophys. Acta* 1993, 1149 (1), pp. 119-126
- 10) Neumann, E., Sowers, A.E., and Jordan, C. A., (Eds), 'Electroporation and Electrofusion in Cell Biology', 1989, Plenum Press, New York
- 11) Gascoyne, P. R., and Vykoukal, J.V., 'Dielectrophoresis-based sample handling in general-purpose programmable diagnostic instruments', *Proc. IEEE* 2004, 92(1), pp. 22-42
- 12) Panofsky, W.K.H., and Phillips, M., 'Classical Electricity and Magnetism'. Addison-Wesley, Reading, Massachusetts, 1955
- 13) Pohl, H. A., 'Dielectrophoresis', Cambridge University Press, Cambridge, 1978
- 14) Debye, P., 'Polar Molecules', Chemical Catalog Co., New York, 1929
- 15) Sauer, F. A., 'Interaction forces between microscopic particles in an external electromagnetic field'. In: 'Interactions between Electromagnetic Fields and Cells' (eds. A. Chiabrera, C. Nicolini, H. P. Schwan). Plenum Publ., New York, 1985, pp. 181-202

- 16) Jones, T. B., 'Electromechanics of Particles', Cambridge University Press, Cambridge, 1995
- 17) Pethig, R., and Markx, G. H., 'Applications of dielectrophoresis in biotechnology'. *Tibtech* 1997, 15(10), pp. 426-432
- 18) Kotnik, T., Bobabovic, F., and Miklavcic, D., 'Sensitivity of transmembrane voltage induced by applied electric fields – a theoretical analysis'. *Bioelectrochem. Bioenergetics* 1997, 43, pp. 285-291
- 19) Kotnik, T., and Miklavcic, D., 'Second-order model of membrane electric field induced by alternating external electric fields', *IEEE Trans. Biomed. Eng.* 2000, 47(8), pp. 1074-1081
- 20) Pethig, R., Bressler, V., Carswell-Crumpton, C., 'Dielectrophoretic studies of the activation of human T lymphocytes using a newly developed cell profiling system'. *Electrophoresis*, 2002, 23(13), pp. 2057-2063
- 21) Price, J. A. R., Burt, J.P.H., and Pethig, R., 'Applications of a new optical technique for measuring the dielectrophoretic behaviour of microorganisms'. *Biochim. Biophys. Acta* 1988, 964(2), pp. 221-230
- 22) Huang, Y., and Pethig, R., 'Electrode design for negative dielectrophoresis'. *Meas. Sci. Technol.* 1991, 2(12), pp. 1142-1146

Chapter 4

Dielectrophoretic characterization and separation of metastatic variants of small cell lung cancer cells

4.1 Introduction

Dielectrophoresis (DEP) has been shown to be a useful technique for the manipulation of particulate matter and is also being widely used to understand the dielectric properties of cell suspensions. DEP has been commonly used as a cell sorter and one of the main advantages that it provides, is the ability to manipulate hundreds of particles in parallel without the need to fluorescently label them. DEP based flow through systems allow us to discriminate between particles with very subtle differences in their dielectric properties. Several studies have been undertaken to determine a role for DEP-based devices in cancer research [1, 2]. There is accumulating evidence that changes in the physicochemical properties of the cell surface, including charge, could contribute to the efficiency of the metastatic process. More recently DEP has been used to differentiate drug accumulation phenotypes in breast cancer cell lines using cytoplasmic conductivity [3], so opening possibilities in the area of drug discovery where DEP devices may be used to determine the functional impact of drug candidates.

One of the initial structural changes observed in cells in response to many extracellular factors is membrane ruffling [4, 5]. The formation of cell surface protrusions is commonly linked to actin filaments and changes in membrane cytoskeletal proteins. In adherent cell lines the actin-driven protrusion of the membrane that causes spreading on the culture substrate is more prominent and this is manifested in the form of

membrane ruffling after the adherent cells are enzymatically detached and placed in suspension. It is becoming clear that actin reorganization is an integral part of early signal transduction pathways, and that many signalling molecules interact with the actin cytoskeleton [6]. The many factors which induce cytoskeletal changes are not entirely clear but they are known to be part of a chemotactic or motility response [6]. Membrane ruffling has been also been shown to indirectly relate to the metastatic potential in tumour cells [4]. The work described in this chapter is directed towards the dielectrophoretic characterisation and separation of the phenotypic variants of small cell lung cancer cells (NCI H69) that we term H69-adherent and H69-suspension variants. Commonly SCLC grow as floating aggregate (suspension) *in vitro* but a certain fraction of the SCLC cells grow as adherent monolayers (Adherent), possessing an altered interaction with the substrate. Pragmatically we define the two variants as follows:

Adherent cells: Cells that attach to the tissue culture substrate and grow in a monolayer, further this variant is affected by contact inhibition and so continuous proliferation is eventually limited by the surface area of the culture vessel. To passage adherent cells, loose cells are removed from the cell culture and the attached cells are subsequently released from the dish using a non-enzymatic cell dissociation solution.

Suspension cells: Usually suspended in a medium as cellular aggregates. In the flask containing these suspension cells, a proportion of the cells were observed to have adherent like characteristics.

It is important to note that the mechanisms for cell-substrate interactions differ from cell-cell interactions. Homophilic cell-cell adhesion in the SCLC cells could be a result of the Neural Cell Adhesion Molecule (NCAM). Polysialylation of NCAM has been demonstrated to markedly reduce the homophilic binding of SCLC cells and thereby resulting in easy detachment from the primary tumor [7]. One of the observed

phenotypic differences between the suspension and adherent variant could be the cell-surface decoration provided by the α -2, 8-linked polysialic acid (PSA) and NCAM. Many other changes at the plasma membrane and associated cytoskeletal architecture will also contribute to the different adhesive properties of the suspension and adherent H69 cells.

An enrichment protocol based on substrate adhesion was used to generate and classify the phenotypic variants of the small cell lung cancer cell tumour. This enrichment protocol is not completely effective as the flask containing suspension cells were observed to contain cells possessing adherent-like characteristics. However, DEP was found to be extremely effective at identifying and separating the adherent-like cells from a suspension flask. This research work was performed in collaboration with Prof. Paul Smith's group at Cardiff university biological sciences department.

4.2 Theory

As shown in chapter 2, the time averaged DEP force on a cell in 2 dimensions can be given by

$$\mathbf{F}_{DEP} = \pi \epsilon_m R^3 \text{Re}[CM] \left(\hat{x} \frac{\partial}{\partial x} (E_x^2 + E_y^2) + \hat{y} \frac{\partial}{\partial y} (E_x^2 + E_y^2) \right) \quad (4.1)$$

where R is the radius of the cell, ϵ_m is the absolute permittivity of the medium, E_x, E_y is the magnitude of the electric field in x and y direction acting on a cell and CM is the Clausius-Mossotti factor.

If the real part of CM is positive then particles move towards the regions of high electric field experiencing what is termed positive DEP. In negative DEP, particles move away from high field regions towards regions of low field intensity.

For cells that exhibits a change from negative to positive DEP as frequency of the electric field is increased, the change in direction occurs at a single frequency known as the cross-over frequency (f_{cr}). At f_{cr} , the dielectric properties of the cell equal those of the medium and so the cell appears transparent to the externally applied electric field and experiences zero DEP force [8]. The cross-over frequency can be given by equation 2.33

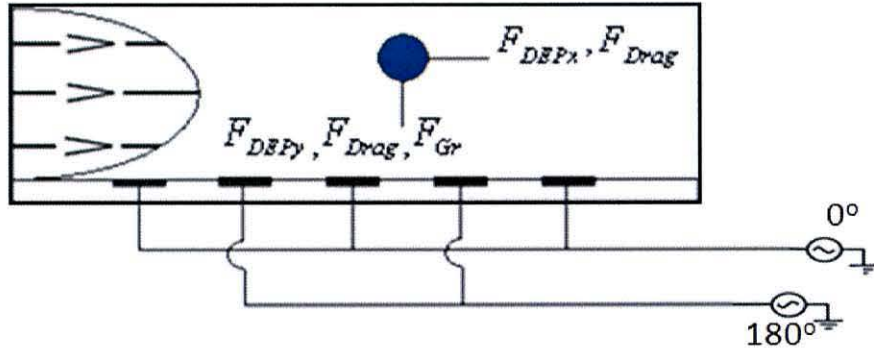


Figure 4.1: Schematic showing the parabolic laminar flow profile of the liquid passing through the separation chamber showing the various forces acting on the particle.

When DEP is used in combination with fluid flow, additional forces of drag, buoyancy have to be considered, shown in figure 4.1. The drag on a spherical particle is given by

$$F_{Drag} = 6\pi\eta r(\mathbf{u} - \mathbf{v}) \quad (4.2)$$

where η is the viscosity of the medium, \mathbf{u} is the instantaneous fluid velocity and \mathbf{v} is the instantaneous particle velocity. Since cells are denser than the aqueous suspending media, the gravitational force (F_{grav}) is given by

$$F_{grav} = \frac{4}{3}\pi r^3 (\rho_p - \rho_m) g \quad (4.3)$$

where ρ_p and ρ_m are the densities of the particle and medium respectively and g is the gravitational constant.

Considering a two dimensional model with stable forces for computational simplicity, the steady state velocity in the horizontal (x) and vertical (y) directions are given by [9]

$$v_x = \frac{F_{DEPx}}{6\pi\eta r} + u_x, \quad v_y = \frac{F_{DEPy}}{6\pi\eta r} - \frac{2r^2}{9\eta}(\rho_p - \rho_m)g \quad (4.4)$$

In the experimental setup the volumetric flow rate was measured and simulations were performed to study the effect of varying fluid flow rates on the cell-capturing efficiency. The velocity of the fluid flow over the electrodes can be derived from the measured volumetric flow rate using equation 4.5

$$Q = u_x A \quad (4.5)$$

where Q is the volumetric flow rate (m^3/sec), u_x is the magnitude of the fluid velocity and A is the cross-sectional area of the fluidic channel.

4.3 Experimental

4.3.1 Cell Preparation

SCLC cells (NCI-H69) [10] were grown in RPMI-1640 media (GIBCO) with 10% FBS under standard culture conditions at 37°C , 5% CO_2 in a humidified incubator. NCI-H69 suspension cells were found to grow as aggregates in culture, but also express a sub-population of variants that show substrate adherence and is referred to as adherent-like. In order to generate a flask containing primarily adherent cells, a simple enrichment protocol for substrate adherence was used.

Cells were washed and re-suspended three times in conductivity buffer prior to use for DEP. The conductivity buffer (8.6% sucrose, 0.3% dextrose and 0.1% BSA in water) was calibrated at room temperature against a $1413 \mu\text{S}/\text{cm}$ standard solution (Hanna instruments, Hungary), to $150 \mu\text{S}/\text{cm}$ by adding Phosphate buffered saline.

4.3.2 Devices and Methods

Quadrupole electrodes were used to dielectrophoretically characterise the two phenotypic variants of SCLC cells used in this work. These electrodes, manufactured

in an 80nm gold and 5nm chromium film on a glass substrate using photolithography, consisted of 4 electrodes with semicircular tips arranged at 90° to each other with an inter-electrode separation of 150 μm between opposite electrodes.

Flow experiments were undertaken in a DEP separation chamber similar to that shown in figure 4.2, consisting of a glass substrate onto which approx 2 cm² arrays of interdigitated microelectrodes with a 20 μm width and spacing was photolithographically fabricated. The channel structure was fabricated from a 150 μm thick adhesive backed polymer cut to shape using femtosecond laser micromachining [11]. An upper polycarbonate plate was used to encapsulate the channels. After assembling the substrate, channel forming layer and upper plate the device was passed through a heated roller to ensure good bonding between the layers. Additionally, the upper plate contained 4 drilled holes over which NanoPort (Upchurch Scientific) fluidic interconnect ports were bonded to form microfluidic inlet and outlets to the separation chamber. Fluid flow through the chamber was controlled using a peristaltic pump (Gilson Minipuls 3).

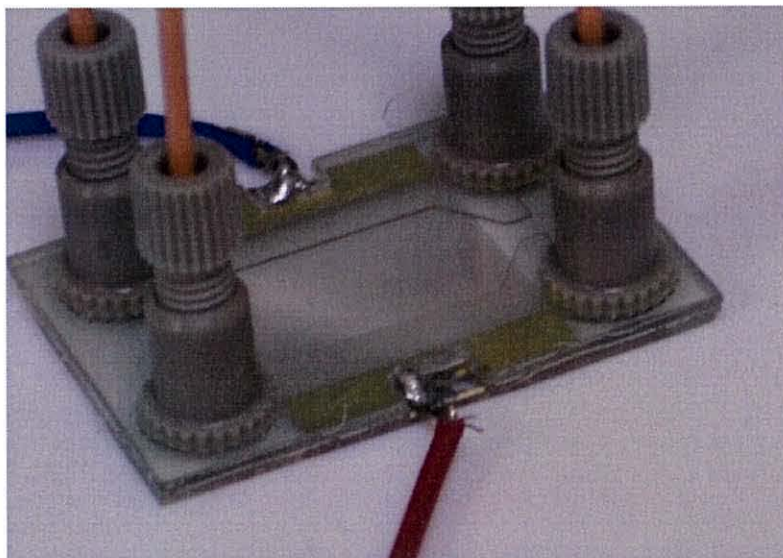


Figure 4.2: Dielectrophoretic fluidic separation chamber.

To obtain a better understanding of the influence of fluid velocity on the dielectrophoretic capture of cells on microelectrodes, two-dimensional simulations of the fluid and particle velocities within the microfabricated DEP chambers used in this work were created using Comsol Multiphysics 3.2. Within the devices the fluid flow channel has a height of 150 μm and a width of 1 cm with five interdigitated electrodes laid out on the bottom surface of the chamber with a width and inter-electrode separation each of 20 μm .

The individual trajectory of the particles can be predicted by using equation 4.4. The flow field in the microchannel is governed by the Navier-Stokes equation with no-slip boundary conditions at the channel wall. Two different velocities of 15 $\mu\text{m/s}$ and 128 $\mu\text{m/s}$ are used for the simulations which were determined from experimental volumetric flow rates.

A quasi-static potential field is calculated by solving Laplace's equation. The boundary conditions are zero charge symmetry everywhere except on the electrodes, where a voltage is applied. All the simulations have been performed considering it is a static case of 3V (peak).

The properties of the liquid are set to: dynamic viscosity $1.0 \times 10^{-3} \text{ kgm}^{-1}\text{s}^{-1}$, density 1000 kgm^{-3} , and permittivity $7 \times 10^{-10} \text{ CV}^{-1}\text{m}^{-1}$. The electrodes were energised with sinusoidal voltages such that the potential difference between adjacent electrodes had a peak value of 3V. Within the simulations CM was set to a value of 0.2 so allowing particles to experience positive DEP towards the high electric field regions around the edges of the electrodes. The density of the cell is assumed to be 1050 kgm^{-3} .

4. 4 Results and Discussion

4. 4. 1 Simulations

The contour plot in figures 4.3 and 4.4 indicates the magnitude of $\nabla|E|^2$ with maximum \log_{10} value of 17.2 V^2/m^3 around the edges of the electrode and it decays to a \log_{10} value of 10 V^2/m^3 at a height of 80 microns. The arrows in figures 4.3 and 4.4 indicate the direction and magnitude of fluid flow along the channel and exhibit a classic laminar-type flow profile. Particle trajectories are indicated by lines starting on the left hand side of the figures 4.3 and 4.4. The particle trajectory is a curve that is tangential to the velocity vector field at every point at a given instant of time. The particle velocity at every point is computed using equation 4.4. These simulations illustrate the pronounced effects of varying fluid flow rates.

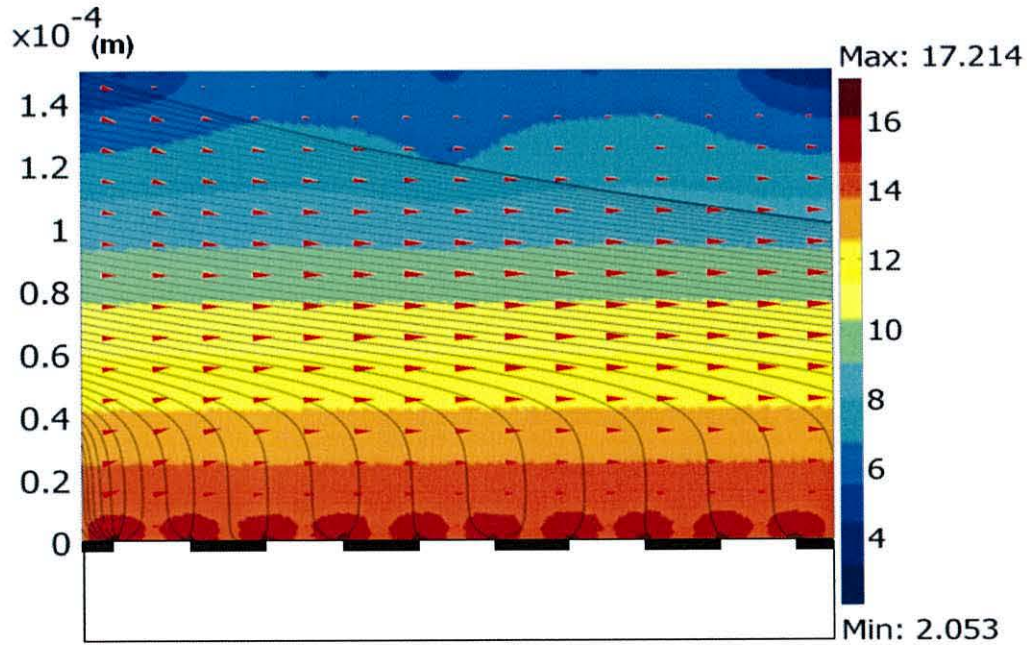


Figure 4.3: Particle trajectories at a fluid flow rate of 15 microns per second. Contour plot shows the $\nabla|E|^2$ magnitude (V^2/m^3 , \log_{10} scale).

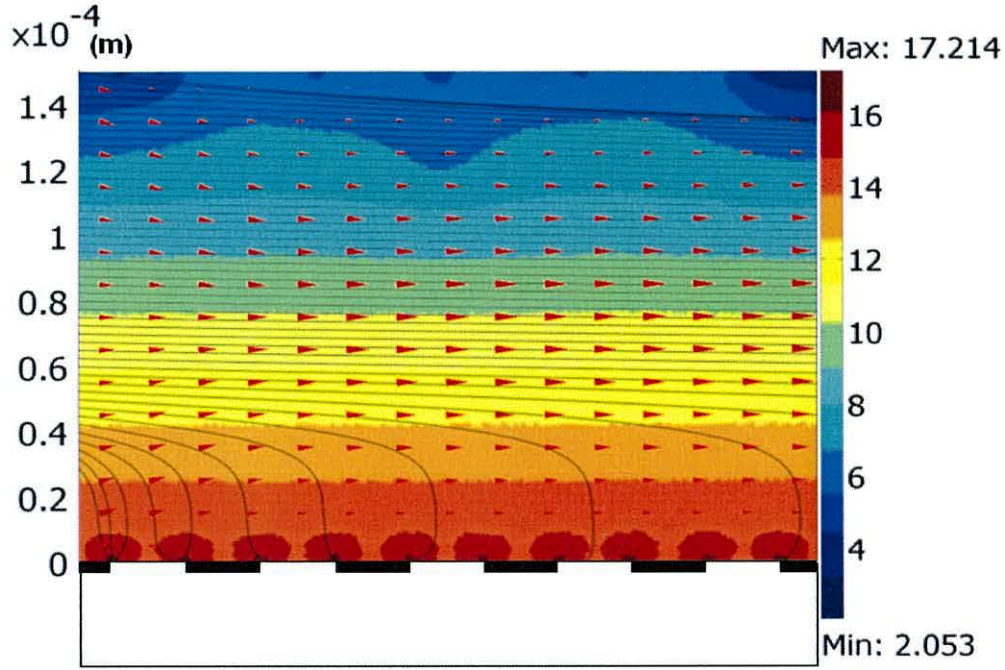


Figure 4.4: Particle trajectories at a fluid flow rate of 128 microns per second. Contour plot shows the $\nabla|E|^2$ magnitude (V^2/m^3 , \log_{10} scale).

The voltages for the two simulations shown above are set to 3 V (peak) between two adjacent electrodes. The simulations show that for a low fluid velocity of 15 $\mu m/s$, shown in figure 4.3, particles up to approximately 80 μm above the electrodes experience a net DEP and gravity-dominated vertical force towards the electrodes. Simulations at 128 $\mu m/s$, shown in figure 4.4, reveals that the vertical force extends only to a height of approximately 45 μm with particles above this height remain mostly unaffected by the electric field. The observations from these and similar simulations have been used to optimize the experimental parameters such as fluid velocity, electrode geometry and energizing voltage for the selective capture and enrichment of cells.

4.4.2 DEP Experiments

SCLC Cells of each phenotype were characterised using the quadrupole electrodes. The electrodes were energised using sinusoidal voltages of 3V (peak) between

adjacent electrodes. Cells were characterised to identify the crossover frequency for each phenotype by observing the direction of dielectrophoresis for electric field frequencies ranging from 1 kHz to 10 MHz. The crossover frequency was measured by finding the frequency at which the cells exhibited zero DEP motion.

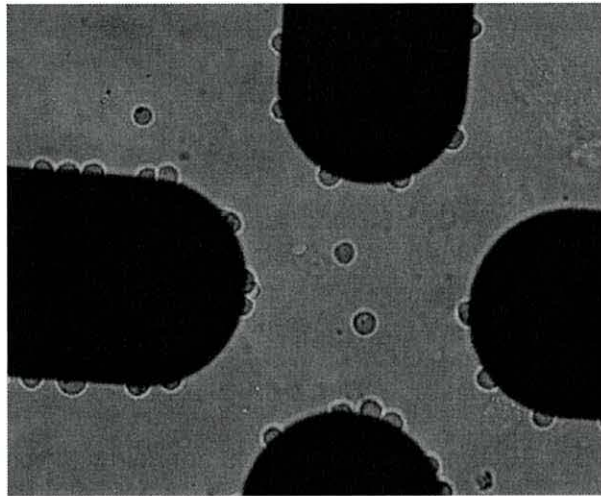


Figure 4.5: DEP collection at 40 kHz shows that almost all the cells taken from an adherent flask experienced positive DEP.

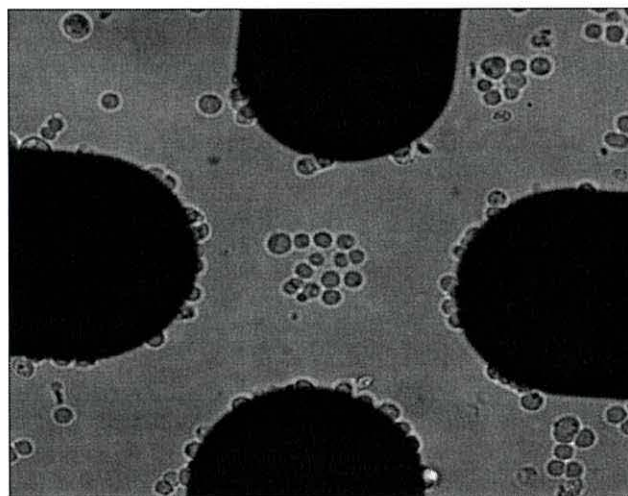


Figure 4.6: Differential DEP separation at 40 kHz from a flask containing suspension SCLC cells. The DEP collection shows adherent-like properties within a population of suspension cells. The adherent cells experienced positive DEP and the suspension cells exhibited negative DEP accumulating in the gap between the electrodes.

Two SCLC cell phenotypes were studied, one an adherent line and the other a line showing predominately suspension characteristics. Using the quadrupole electrodes

the distribution of crossover frequencies for each phenotype was measured. For the adherent phenotype (obtained from a flask containing adherent cells) observations of >50 cells found the crossover frequency ranged from 30 kHz to just below 40 kHz. Figure 4.5 shows cells from an adherent flask undergoing positive dielectrophoresis at a frequency of 40 kHz. For the suspension phenotype, a larger range of crossover frequencies was observed ranging from 30 kHz to 60 kHz. Additionally it was observed that a proportion of the cells from the suspension flask exhibited adherent-like properties within a population of suspension cells, choosing an electric field frequency of 40 kHz, it was possible to selectively separate cells displaying adherent-like properties. Such separation is shown in figure 4.6 where adherent-like cells are seen dielectrophoretically collected at the edge of the electrodes while the suspension cells are pushed into the gaps between the electrodes.

Using the previously determined cross-over frequency values, experiments to selectively collect and enrich samples of mixed phenotype were undertaken using the DEP separation chambers. Prior to these experiments, the chambers were characterised for collection efficiency at different fluid flow velocities. The flow rate to achieve a desired level of cell collection was determined by fixing the electrode voltage and frequency and adjusting the fluid velocity to achieve good capture of a sample of adherent phenotype cells on the electrodes. Figure 4.7 shows the influence of fluid flow rate on the collection efficiency of the chambers. All cell concentrations were determined using a Coulter particle counter (Beckman Coulter, High Wycombe, UK). The error associated with the determination of cell concentration is assumed to be roughly 3%. The collection efficiency can be defined as

$$Collection\ Efficiency(\%) = \frac{Cell\ collected\ by\ PDEP\ \left(\frac{cells}{ml}\right)}{Input\ cells\ \left(\frac{cells}{ml}\right)} \times 100 \quad (4.6)$$

$$\begin{aligned}
& \text{Cells collected by PDEP} \left(\frac{\text{cells}}{\text{ml}} \right) \\
& = \text{Input cells} \left(\frac{\text{cells}}{\text{ml}} \right) - \text{uncaptured cells at the outlet} \left(\frac{\text{cells}}{\text{ml}} \right)
\end{aligned} \tag{4.7}$$

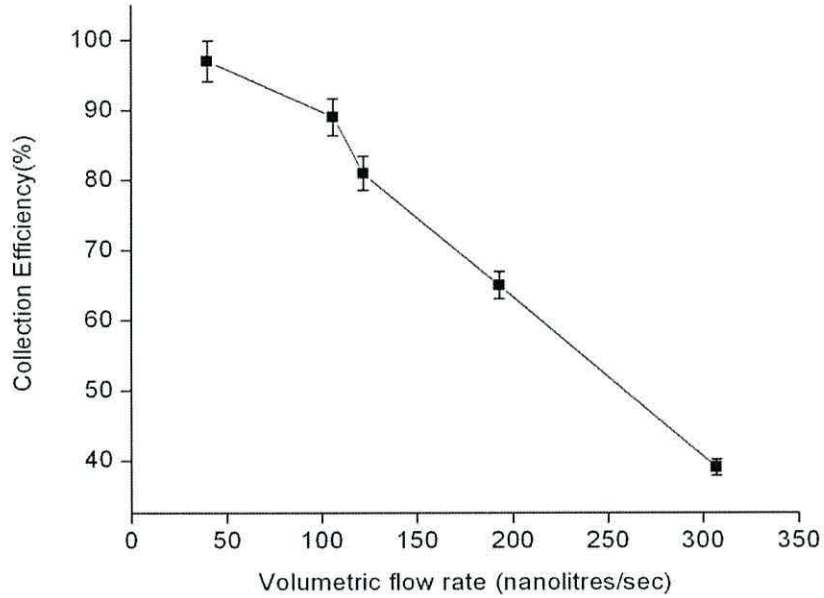


Figure 4.7: Experimentally determined effect of flow rate on collection efficiency of adherent cells.

Using the separation chamber a mixed population of adherent-like and suspension cells were fractionated by flowing the cells through the chamber at a flow rate of 50 nl/s while applying a 3V (peak) 40kHz voltage to the chamber electrodes. At this frequency cells showing adherent-like characteristics collect on the electrodes, as shown in Figure 4.8, while suspension cells experience negative DEP force and were carried through the chamber with the fluid flow.



Figure 4.8: Cells showing adherent-like characteristics collect on the electrodes. The suspension cells (marked in yellow) did not adhere to the electrode edge and is carried through to the outlet.

Cells exiting the chamber while the voltage was applied to the electrodes were collected. When the entire sample had been passed through the chamber, the voltage was turned off and additional suspending medium was passed through the chamber. This allowed the adherent-like cells trapped on the electrodes to be collected as a separate fraction. Both fractions were cultured in 96 well plates for 1 day. Post culture observation of the fractions, revealed that the cells collected by positive DEP exhibited adherent characteristics while the second fraction exhibited suspension characteristics. This experimental result validates the supposition that cells within the suspension flask display phenotypic variations ranging from adherent-like to suspension like characteristics.

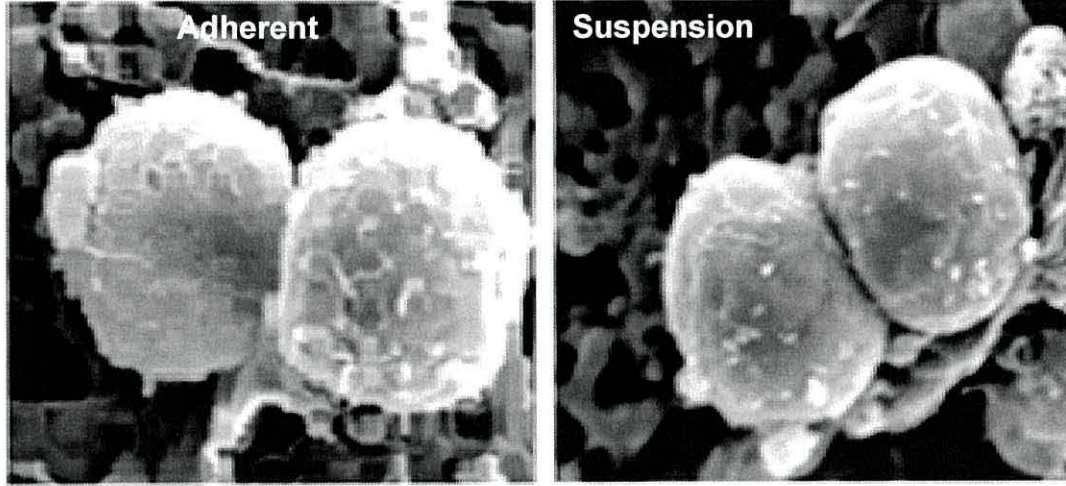


Figure 4.9: Cell Electron Micrographs shows greater membrane texturing in the adherent-like phenotype

For viable cells equation 2.33 can be approximated to [8]

$$f_{cr} = \frac{\sqrt{2}\sigma_m}{2\pi r C_{mem}} \quad (4.8)$$

where r is the cell radius and C_{mem} is the cell membrane capacitance per unit area.

Microscope measurements give the diameter of both cell phenotypes to be $10 \mu\text{m} \pm 1.5 \mu\text{m}$. From equation 4.8 and using the range of crossover frequencies measured for each cell phenotype, and the experimental medium conductivity of $150 \mu\text{S/cm}$, membrane capacitances of $17\text{--}22 \text{ mF/m}^2$ were obtained for the cells from an adherent flask and the adherent-like cells, with a mean value of 19.5 mF/m^2 . For the suspension cells the membrane capacitance varies between $11\text{--}17 \text{ mF/m}^2$ with a mean value of 14 mF/m^2 . Previous studies have shown that membrane capacitance mainly depends on membrane surface topography [12]. Extra surface features can increase the membrane surface area and hence the membrane capacitance. Scanning electron micrograph studies, shown in figure 4.9, of the cell phenotypes used in this work reveal that cells exhibiting adherent characteristics have a greater degree of surface texturing than those exhibiting suspension-like

characteristics. This in turn leads to a larger membrane capacitance and subsequently a lower range of crossover frequencies.

It is our biological hypothesis that the molecular changes that occur in the phenotypes lead to the downstream cytoskeletal changes reflected in the form of increased membrane ruffling associated with the adherent phenotype. Homophilic cell-cell adhesion could be a result of the NCAM expression and the detachment from the primary tumor could be a result of the differences in polysialation levels of NCAM. These differences in the phenotypic profiling of the variants can result in different manifestations of metastasis.

4. 5 Conclusion

This study of H69 phenotypic variants has shown that DEP has the ability to selectively sort cell types with subtle phenotypic differences. The phenotypic variation of the adherent cells detected by DEP is associated with downstream cytoskeletal changes reflected in the form of increased membrane ruffling as in the adherent SCLC phenotype compared to the suspension phenotype. Electrokinetic studies have shown that phenotypic differences can be identified using dielectrophoretic examination, leading to the possibility of cytometric devices for analysis, identification and monitoring of tumour heterogeneity. DEP separation chambers have been used to sort the phenotypes and the post culture observation of the fractions revealed that the cells collected by positive DEP exhibited adherent characteristics while the second fraction exhibited suspension characteristics. Having utilized DEP to detect differences in the suspensions and adherents, this method can also be used as a research tool to monitor the enrichment and changes when testing drug effects, or monitor the evolution of the tumour under different selection pressures.

4. 6 References

- 1) Becker, F.F., Wang, X.B., Huang, Y., Pethig, R., Vykoukal, J., and Gascoyne, P. R.C., 'Separation of human breast cancer cells from blood by differential dielectric affinity', *Proc. Natl. Acad. Sci.*, 1995, 92, pp. 860-864
- 2) Broche, L., Bhadal, N., Lewis, M., Porter, S., Hughes, M.P., and Labeed, F., 'Early detection of oral cancer – Is dielectrophoresis the answer?', *Oral Oncology*, 2007, 43, pp.199-203
- 3) Coley, H. M., Labeed, F.H., Thomas, H., and Hughes, M.P., 'Biophysical characterization of MDR breast cancer cell lines reveals the cytoplasm is critical in determining drug sensitivity', *Biochimica. et. Biophysica. Acta*, 2007, 1770, pp. 601-608
- 4). Stossel, T. P., 'On the crawling of animal cells'. *Science* 1993, 260:1086.
- 5) Myat, M., Anderson, S., Allen, L. A., Aderem, A., 'Marcks Regulates Membrane Ruffling And Cell Spreading', *Current Biology*, 1997, 7, pp. 611- 614
- 6) Ridley, A., 'Membrane ruffling and signal transduction'. *Bioessays.*, 1994, 16, pp. 321-327.
- 7) Ruoslahti E. , Giancotti F.G. , 'Integrins and tumor cell dissemination', *Cancer Cells.* , 1989, 1, pp. 119-126
- 8) Pethig, R. , and Talary, M. , 'Dielectrophoretic detection of membrane morphology changes in Jurkat T-cells undergoing etoposide-induced apoptosis', *Nanobiotechnology IET*, 2007, 1, pp. 2-9
- 9) Holmes, D., Green, N.G., Morgan, H., 'Microdevices for dielectrophoretic flow - through cell separation', *Engineering in Medicine and Biology Magazine, IEEE*, 2003, 85 ,2003
- 10) Gazdar, A.F. , Carney, D.N. , Russell, E.K. , Sims, H.L. , Baylin, S.B. , Bunn, P.A. Jr, Guccion, J.G. , Minna, J.D. , 'Establishment of Continuous Clonable Cultures of Small-Cell Carcinoma of the Lung Which Have Amine Precursor Uptake and Decarboxylation Cell Properties', *Cancer Res*, 1980, 40, pp. 3502-3507
- 11) Burt, J.P.H., Goater, A.D., Menachery, A., Pethig, R., and Rizvi, N.H., 'Development of microtitre plates for electrokinetic assays', *J. Micromech. Microeng.* , 2007, 17, 250-257
- 12) Wang, X., Becker, F.F., and Gascoyne, P.R.C., 'Membrane dielectric changes indicate induced apoptosis in HL-60 cells more sensitively than surface phosphatidylserine expression or DNA fragmentation', *Biochimica. et. Biophysica. Acta.* , 2002 1564, pp. 412-420

Chapter 5

Fabrication and Testing of Dielectrophoretic Tweezers

5.1 Introduction

The ability to position cells in an organized manner at addressable locations is becoming an important requirement for many areas of biological research. Biosensor technologies require precise positioning of biological cells on measurement electrodes to detect chemical stimuli caused by environmental changes [1]. The ability to artificially engineer bio-cellular networks is also gaining interest. For example, the ability to characterise the electrical activity of patterned neuron networks in-vitro is important because it provides a method to study communication pathways and the various mechanisms involved in memory formation [2].

It has also become important for cell biologists to introduce foreign DNA into a cell and study the gene expression for the purpose of gene therapy [3]. Transfection is the process used to introduce DNA into cells. The study of transfected cells requires the ability to differentiate and then isolate the cells that have taken up the external DNA construct from the cells that have not. The use of a fusion construct containing a fluorescent indicator is becoming increasingly popular as a detection tool for transfection and as a quantitative reporter of gene expression [4].

Several methods have been previously reported in the literature to achieve precise control over the positioning and separation of cells on a multi cellular and single cellular level. One of the most common methods for single cell manipulation is the use of a suction micropipette. The main disadvantage of this method is the lack of precise

control, which can result in membrane rupture and also cause significant disturbance to the surrounding fluid and cells during suction. Techniques such as optical tweezers [5], optoelectronic tweezers [6], magnetic forces [7], acoustic traps [8], and microfluidic chips [9] have previously been employed to manipulate particles. Optical tweezers require extensive modification to the microscope optical setup and the force generated for trapping and manipulation is relatively weak. The other methods mentioned do not provide the selectivity necessary for precisely handling individual cells. DEP-based technologies are very versatile for cell manipulation and separation and have been used for a wide range of applications [10].

The development of DEP tweezers described in this chapter was performed as part of the collaboration with the BioCurrents Research Center at the MBL, Woods Hole, for the specific task of isolating and relocating single cells that have taken up a fluorescently labeled DNA construct. Such tweezers were also envisaged to aid the research on artificially engineered 3D cell constructs described in chapter 6.

The use of DEP tweezers has previously been shown for the pickup and release of single cells. Several designs have been explored such as pin-plane electrode geometry [11], thin film electrodes on a glass capillary [12], dual disk sealed in a capillary [13] and a capacitively coupled electrode [14]. In this chapter an exposed twin-wire electrode system is described, shown in figure 5.1. This design allows for flexibility in the design process to achieve very precise control in the manipulation of a single cell in a dense group of cells. The technology needed for its manufacture is also easily available to biological laboratories. Thus, the DEP tweezers design was deliberately directed towards achieving highly targeted cell isolation using technologies that are readily available within an electrophysiology laboratory.

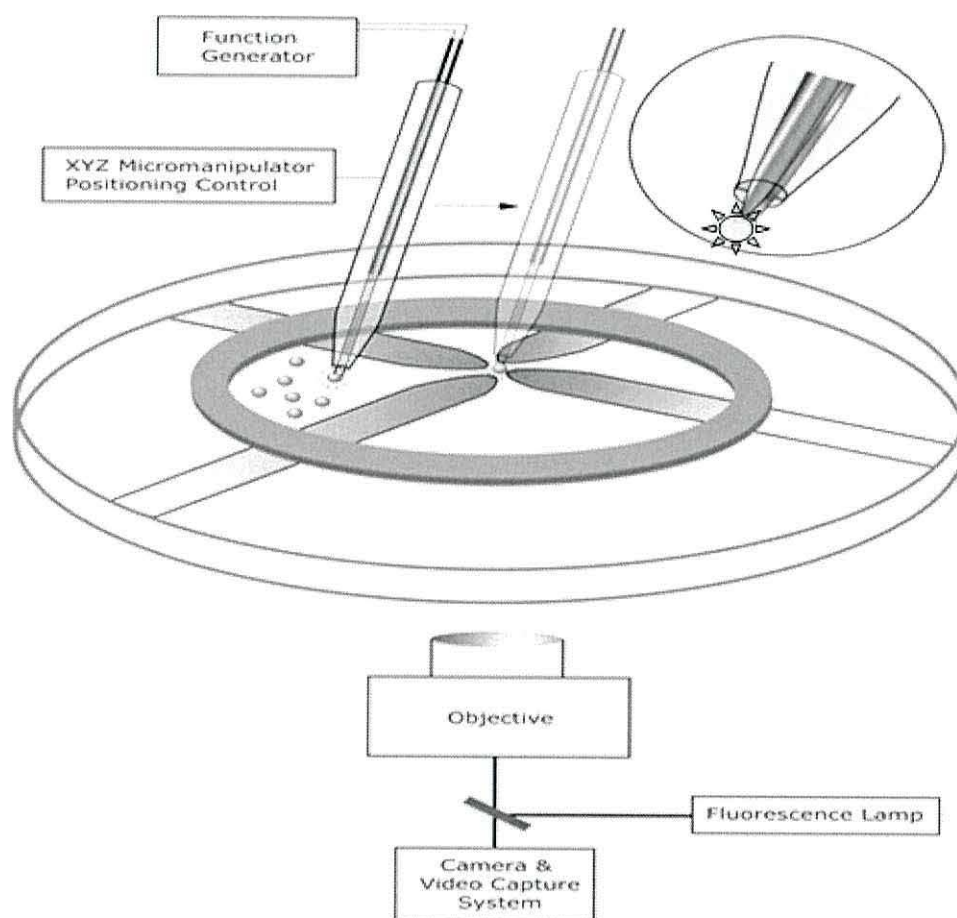


Figure 5.1: Schematic diagram of the cell positioning system.

The work for this chapter investigated the use of DEP forces towards developing a method for the selective removal of a target cell from other cells. This exploits the fact that gentle DEP forces can be applied to cells in suspension to manipulate them in a spatially regulated manner. The developed system was used to separate a cell expressing a protein of interest that was tagged to the green fluorescent protein (GFP). This cell isolation system utilizes DEP in combination with fluorescence detection.

In this chapter, the use of micro capillary based electrodes has been employed for the purpose of separating cells which have transiently incorporated the GFP constructs from the non-expressing cells. This electrode design generates a highly non-uniform electric field around the tip, thereby providing a method to relocate a single cell.

Electric field simulations have been used to optimize the electrode geometry and also to determine a suitable working voltage. The fluorescence based excitation of the GFP marker, was used to identify the cells to be isolated. The specific cells can then be manipulated and isolated to an addressable location for analysis or extraction.

Fluorescence activated cell sorting (FACS) can also be used for the separation of the transfected cells because of the presence of a fluorescent tag [15], but, it is an expensive method and not every laboratory has access to a FACS machine. The method proposed in this chapter offers many advantages for the trapping of transfected cells including early isolation, high selectivity and a distinct cost advantage. The expression of the gene product can be evaluated 24-48 hours after transfection and isolation at this early stage allows for the transfer of this target cell into a different environment for further analysis or enrichment.

The objective was to isolate gene expressing cells and for this it is necessary to be able to select cells expressing the incorporated gene product. In this work a construct which included a GFP marker gene, was used. In this work, DEP tweezers were used to manipulate cells in small sample volumes with a good amount of control and accuracy. The design, manufacture and experimental process involved in the precise positioning of the target cells using the two-wire DEP tweezers, was discussed. Simulations were performed to understand and optimize this design to achieve highly selective trapping of individual cells.

The work described in this chapter is a collaborative project with Dr Peter Smith of the Biocurrents Research center at the MBL, Woodshole.

Taking the simplistic view of a cell as a spherical homogeneous particle, the time averaged DEP force on the cell is given by

$$\mathbf{F}_{DEP} = \pi \varepsilon_m R^3 \text{Re}[CM] \left(\hat{x} \frac{\partial}{\partial x} (E_x^2 + E_y^2 + E_z^2) + \hat{y} \frac{\partial}{\partial y} (E_x^2 + E_y^2 + E_z^2) + \hat{z} \frac{\partial}{\partial z} (E_x^2 + E_y^2 + E_z^2) \right) \quad (5.1)$$

where r is the radius of the cell, ε_m is the absolute permittivity of the medium, (E_x, E_y, E_z) are the x, y, and z components of the electric field magnitude. CM is the Clausius-Mossotti factor, which describes the Maxwell-Wagner relaxation that occurs at the interfaces between dissimilar dielectrics such as the particle and medium. The magnitude and direction of the DEP force is given by the CM factor and the electric field non-uniformities.

The desired motion of an individual cell in a stationary fluid will arise when the applied DEP force overcomes the viscous drag force, gravity, substrate adhesion and inertia.

The drag on a spherical particle is given by:

$$\mathbf{F}_{Drag} = -6\pi\eta r \mathbf{v} \quad (5.2)$$

where η is the dynamic viscosity of the medium and \mathbf{v} is the instantaneous particle velocity.

Since cells are denser than their aqueous suspending media, the sedimentation force can given by:

$$F_{grav} = \frac{4}{3} \pi r^3 (\rho_p - \rho_m) g \quad (5.3)$$

where ρ_p and ρ_m are the densities of the particle and medium respectively and g is the gravitational constant. In the experiments and calculations performed in this chapter, the gravitational force can be neglected since the tip of tweezers is placed at approximately the height of the cell; hence, the cell is attracted towards the tweezers by floating along the surface of the substrate.

Assuming negligible inertia and cell-substrate interactions and other electrokinetic phenomena [16, 17], the expressions for the motion of a cell can be given by Newton's laws of motion [18]. According to Newton's law of motion, the rate of change in the momentum of a cell is directly proportional to the sum of the forces acting on the cell. Ignoring buoyancy force, the equation of motion for the particle can be given by

$$m \frac{dv}{dt} = F_{DEP} + F_{Drag} \quad (5.4)$$

In the above equations, the force terms are functions of spatial position.

5.2 Experimental Design and Methods

The cells used in the work described in this chapter were derived from an immortalized schwannoma cell line, HEI 193. Cells were cultured in Dulbecco's modified Eagle's medium (DMEM, Cellgro, Herndon, VA) containing serum-free N-2 Supplement (Gibco), 2 μ M forskolin (Calbiochem, San Diego, CA), 14 ng/ml of recombinant human glial growth factor (rhGGF2, Sigma), 50 μ g/ml gentamicin, 10% fetal bovine serum (FBS, Sigma) and 100 μ g/ml penicillin/streptomycin (P/S, Cellgro), and plated onto plastic dishes (75 mm). All cells were grown at 37°C in a 95% air/5% CO₂ atmosphere.

The cells were transfected with a construct which contained a Ca β subunit cloned into the pXOOM vector [19, 20]. In order to identify cells expressing the incorporated gene product, a construct was used which included a GFP marker gene. The cells were transfected in cultures grown in 75 mm² culture flasks with 57 μ l of the DNA construct and 75 μ l of Lipofectamine. The transfected cell lines show different levels of expression depending on the quantity of the plasmid introduced into the cell. This cell transfection procedure was supervised by Dr Mark Messerli at the MBL, Woods Hole.

Immediately prior to the DEP experiments, the adherent cells were detached from the bottom of the culture flask using trypsin, and the cells were then re-suspended and washed twice in the DEP medium. Dielectrophoresis solutions were prepared to different conductivities varying from 19 to 115 mS/m by addition of phosphate buffered saline solution to de-ionized water. The conductivities were measured using a YSI 3200 Conductivity Instrument. The solution was then adjusted to a pH of 7.4 by adding NaOH and the osmolarity was adjusted to physiological levels of around 300 mOsm/kg by adding sucrose and the osmolarity was measured using an Osmometer.

The electrodes to be used consisted of gold wires that were electrochemically etched [21]. Gold wire of diameter 25 μm was etched in 1 M aqueous solution of HCl with a 4V square wave at 2.5 kHz. The main considerations in the etching process were the tip radius (r) and the taper angle (θ) as shown in figure 5.2. By varying the immersion depths and the holding time in the etchant, a roughly hemispherical tip and a gradual taper along the wire could be achieved. The etching process was continuously monitored through a microscope.

These etched gold wires are inserted into theta glass capillaries (1.5 mm OD, 0.23 mm Wall, 0.17 mm Septum). The pipettes were pulled using a Flaming/Brown style micropipette puller (Sutter Instrument, Novato, CA). The pulling parameters were set based on the tip diameter and the taper angle required of the pulled pipette. Due to the limitations of the optical setup and the maximum spatial resolution achievable, the final dimensions of the tip of the pulled pipettes were subject to an error of around ± 1 micron.

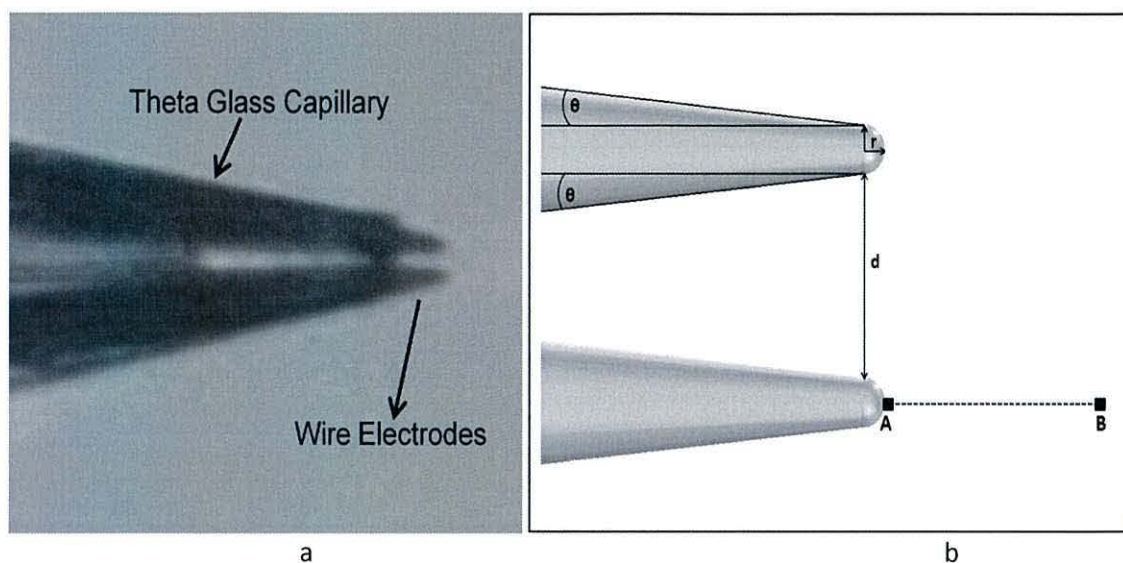


Figure 5.2: DEP tweezers (a) Consists of two etched wires inserted into a theta glass capillary. The tip of the etched wires is spaced roughly 4 microns apart and each wire has a tip radius of roughly $1\ \mu\text{m}$ (the aspect ratio of the image is not to scale). (b) Schematic showing the various design parameters.

The experiments were performed on an inverted fluorescence microscope (Zeiss Axioscope) equipped with a micromanipulator, and the electrodes were placed onto the micromanipulator at an angle of 45° to the horizontal. The microscope was housed within a heated chamber to minimize any thermal shock to the cells, and the experiments were monitored and recorded using a video camera setup. The cell manipulation was carried out on a substrate which was custom coated (MicroSurfaces Inc) with a dense layer of poly-ethyleneglycol (PEG) approximately 8 nm thick. The PEG coating was put down since it does not allow the adsorption of proteins, cells and other biomolecules, so providing a completely passive adhesion free surface for the experiments.

Initially, the substrate was uniformly wetted with $200\ \mu\text{l}$ of the DEP medium, and then the DEP tweezers were lowered into the medium. A $10\ \mu\text{l}$ sample of the cell suspension, at a density of 1×10^6 cells/ml, was carefully pipetted onto the substrate such that the spread of the cells upon settling was minimal. The cells were observed to settle onto the substrate in under 10 minutes, and the target cells were then located by

scanning the substrate and locating the cells exhibiting relatively high fluorescence intensity. The DEP tweezers were brought to approximately 20 microns of the centre of the target cell. The electrodes were then energized in order to trap the target cell between the twin-wire electrodes, and using the micromanipulator the target cell could be moved to a specific location approximately 5mm away from the other cells. The target cell could either be moved to a clear space on the substrate (in order to extract the cell using a micropipette) or positioned within a microelectrode array (for further DEP or electrorotation characterisation, for example).

To obtain a better understanding of the influence of the design variables, simulations were performed using the finite element method in COMSOL Multiphysics 3.3 Ltd. A 3D geometry model of the two identical wires was created. Each wire was defined as a cone with a taper angle (θ), the apex geometry of the electrode wire was defined as a hemisphere with a radius r and the spacing between the twin-wire electrodes was defined as (d). The magnitude and spatial profile of the DEP force are critical factors in determining the targeted manipulation of individual cells. Based on the manufacturing micro-geometry variables, a study was performed of the effect of varying each design parameter. The geometry was constructed such that the electrodes were located in the center of a cube ($100\ \mu\text{m} \times 100\ \mu\text{m} \times 100\ \mu\text{m}$). A Neumann boundary (normal derivative of the electric displacement was set to zero) conditions were set on the walls of the cube, whilst on the electrode surfaces Dirichlet boundary conditions were imposed. Potentials of zero and 1V(peak) were set for the first and second electrode surfaces, respectively.

5.3 Results and Discussion

5.3.1 Simulation

From equation 5.1 it can be seen that for a fixed biological system and suspending medium the variation of the gradient of the square of the electric field strength ($\nabla|E|^2$) is the parameter that will mainly influence cell movement. For a particular geometrical feature of an electrode, the spatial variation of the term $\nabla|E|^2$ will provide an indication of the effective DEP cell capture volume generated by that feature. The vector parameter $\nabla|E|^2$ is dependent on the applied voltage and the design geometry. To demonstrate the effects of the variable electrode geometry parameters simulations were carried out by varying the radius of the tip of the wire (r), spacing between the twin-wire electrodes (d), the angle of taper (θ) and the length of the protruded electrode (l). It was observed that the angle of taper and the length of the protruded electrodes do not have a significant effect on the optimization process within practical fabrication limits and as a result it has been excluded in the discussion below.

A logarithmic scale is employed in the plots to represent the variation of the magnitude of $\nabla|E|^2$ since this electrode geometry exhibits very sharp spatial variations of $\nabla|E|^2$. The simulations have been performed considering it is a static case of 1V peak.

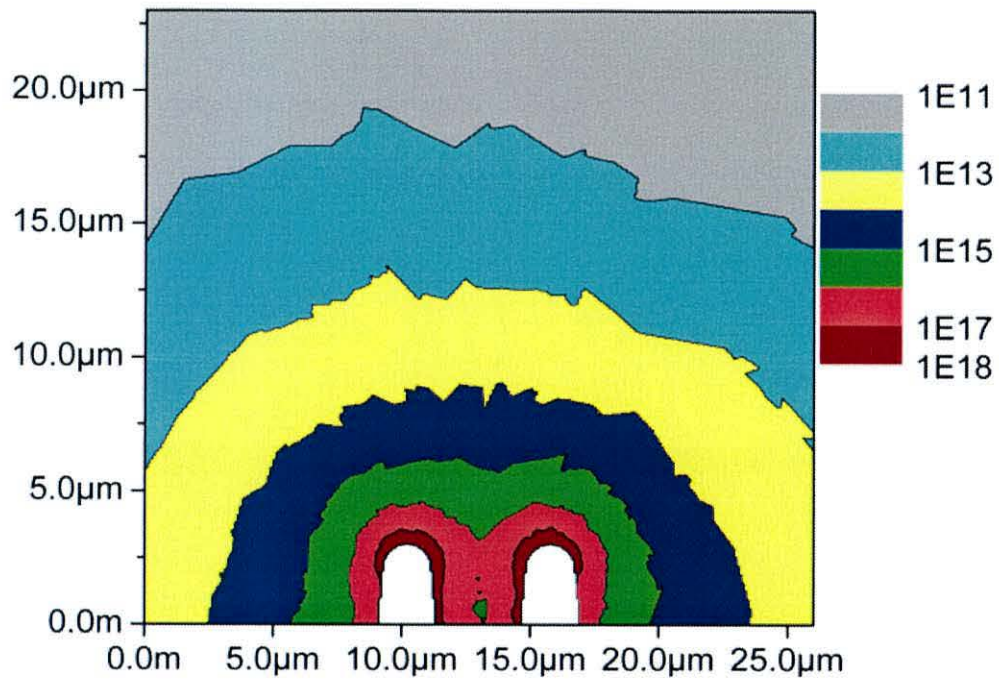


Figure 5.3: Contour plot of the magnitude of $\nabla|E|^2$ (V^2/m^3 , \log_{10} scale) for an applied voltage of 1V (peak).

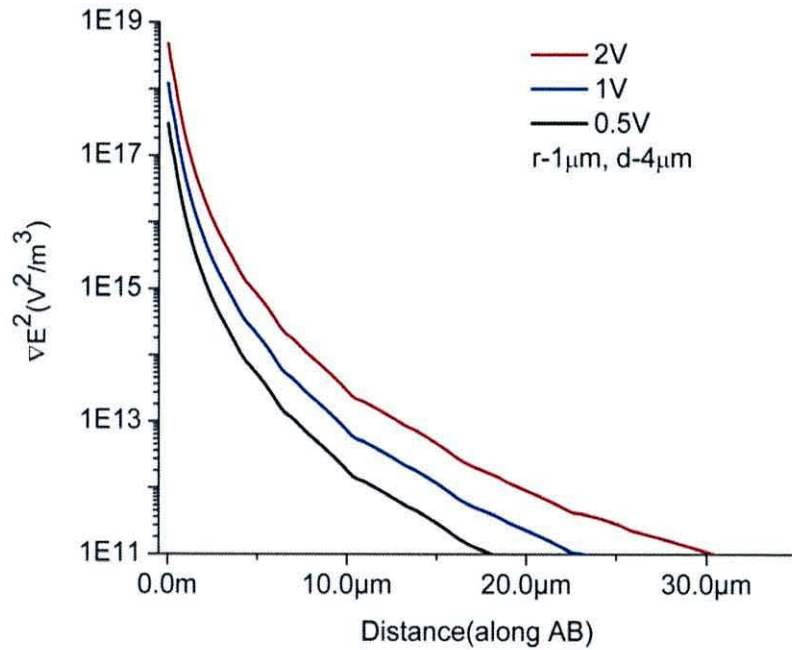


Figure 5.4: Plot of the variation of the magnitude of $\nabla|E|^2$ along AB (as defined in figure 5.2) for a constant tip radius and electrode spacing, as a function of applied voltage.

In figure 5.3 the magnitude of $\nabla|E|^2$ for a 2D cross section along the centre of the wire is shown. The radius of the tip of the electrode is set to $1\mu\text{m}$, the gap between the electrodes is set to $4\mu\text{m}$ and the voltage is set to 1V (peak). It can be observed that the $\nabla|E|^2$ contours are symmetrical with respect to the centre of the gap between the two wires. From the contour colour plot, it can be seen that the $\nabla|E|^2$ peak magnitude occurs at the apex of the wire electrodes and the magnitude falls off rapidly away from the electrodes.

In figure 5.4, when all the design parameters are fixed, the magnitude of $\nabla|E|^2$ is directly proportional to the square of the voltage. Therefore, by decreasing the voltage, the penetration field of the DEP force can be significantly reduced at the apex of the electrode wires and also distances further away.

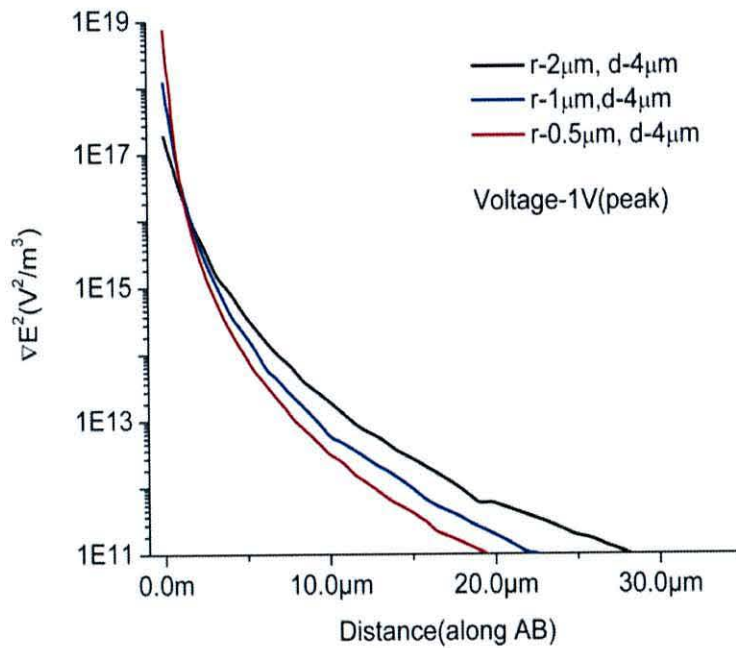


Figure 5.5: Plot of the variation of the magnitude $\nabla|E|^2$ along AB (as defined in figure 5.2) for a constant applied voltage and electrode spacing, as a function of tip radius (r).

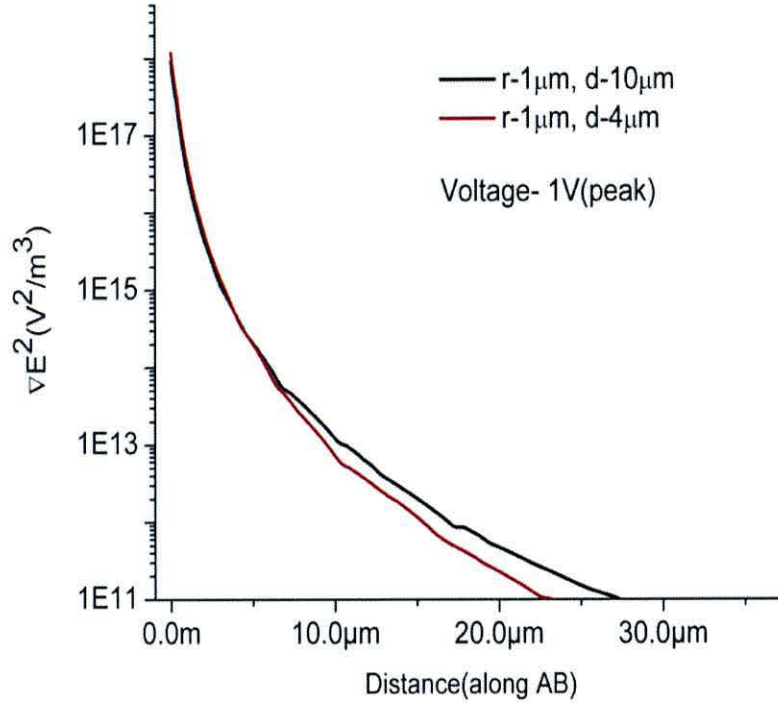


Figure 5.6: Plot of the variation of the magnitude of $\nabla|E|^2$ along AB for a constant applied voltage and tip radius and a variation of electrode spacing (d).

From figure 5.5, it is observed that variation of tip radius has a significant effect at the apex of the wires and at distances further along. A tip radius of $0.5 \mu\text{m}$ shows the largest $\nabla|E|^2$ magnitude at the apex and also exhibits the largest slope variation along AB. The $2 \mu\text{m}$ tip exhibits the lowest $\nabla|E|^2$ magnitude at the apex and the least slope variation. It can also be observed that the maximum values of DEP force at the apex scales non-linearly with decreasing tip radius.

The spatial variation of $\nabla|E|^2$ can also be controlled by varying the separation distance between the electrodes. In figure 5.6, curves are plotted for an electrode spacing of $4 \mu\text{m}$ and $10 \mu\text{m}$. With increasing separation, a drop in the magnitude of $\nabla|E|^2_{\text{max}}$ is observed at the apex and further along the curve a larger spreading of the field is observed. Upon comparing the effects of changing the two geometry parameters, it is clear that the difference in the drop of the magnitude of $\nabla|E|^2$ at the apex and at a

distance of 20 μm from the tip is more significant upon changing tip radius from 0.5 μm to 2 μm rather than the electrode spacing from 4 μm to 10 μm .

5.3.2 Experimental

Before attempting to manipulate the HEI-193 schwannoma cells, knowledge of their DEP behavior with the variation of solution conductivity was useful. In particular, it was important to predict the experimental conditions required to generate either positive or negative DEP movement of the cells. Cells were characterised to identify the crossover frequency for each phenotype by observing the direction of dielectrophoresis for electric field frequencies ranging from 10 kHz to 10 MHz. The crossover frequency was measured by interpolating the frequency at which the cells exhibited zero DEP motion. In brief, the suspended cells ($\sim 1 \times 10^5$ cells/ml) were subjected to a stationary non-uniform electric field using a quadrupole electrode setup shown in figure 5.7.

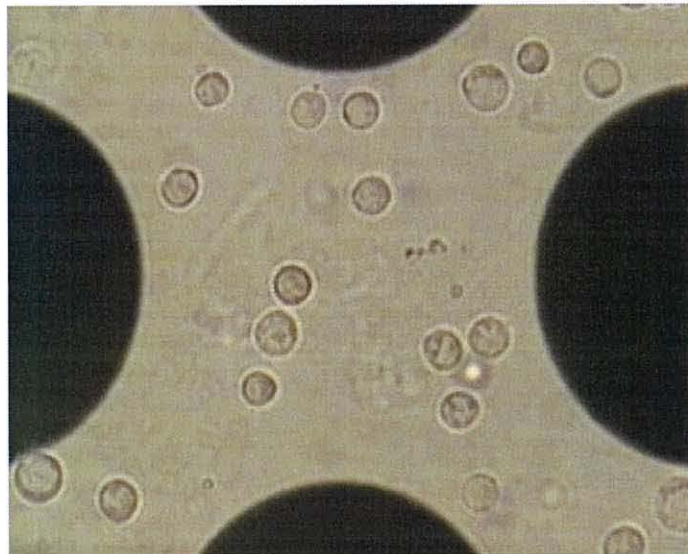


Figure 5.7: The semi-circular quadrupole electrode designs used in the DEP characterisation experiments. The non-uniform electric fields were produced by energizing adjacent electrodes with A.C. signals of potential difference between 2 and 3 Volts (peak).

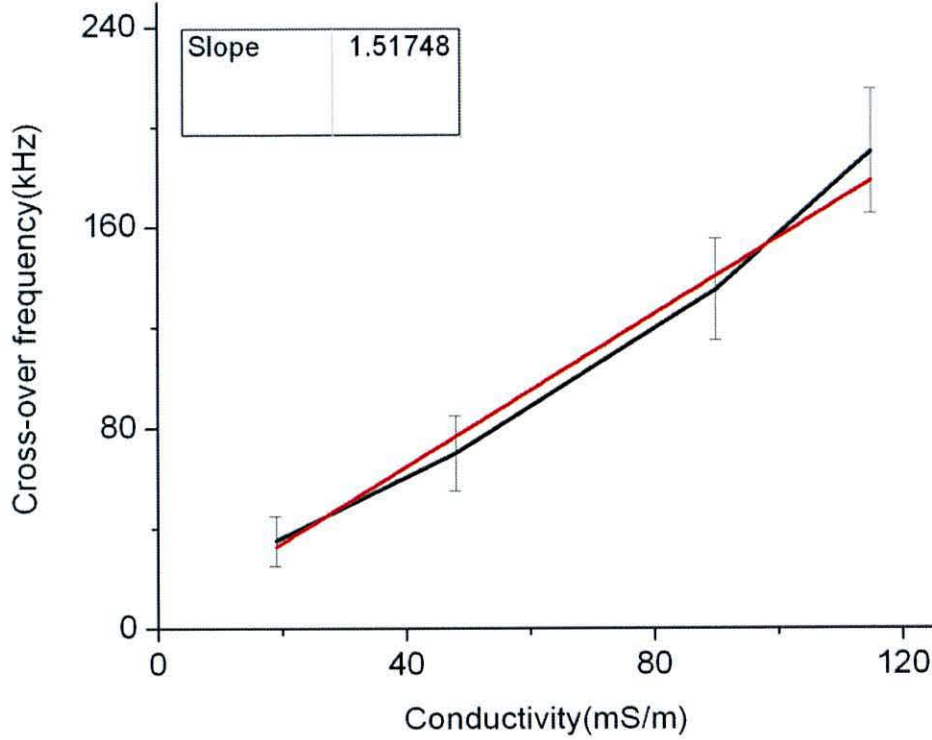


Figure 5.8: Plots of the DEP data for the HEI-193 cells. The lines represent the variation of the cross over frequencies vs. solution conductivity.

Based on the theory, a plot shown in figure 5.8 of cross-over frequency against solution conductivity should be linear (of the form $y = mx + c$), where m is the slope and c is the intercept. The membrane capacitance can then be calculated from equation [22].

$$C_{mem} = \frac{\sqrt{2} \times 10^{-6}}{2\pi r \text{slope}} \quad (5.5)$$

The average radius of the HEI-193 cells was measured to be $6(\pm 1.5) \mu\text{m}$. The membrane capacitance is calculated to be approximately 24 mF/m^2 . The polarisation factor depends on the complex permittivities of the cell and its suspending medium. In this work, the single-shell dielectric model as detailed chapter 2 is considered. In this model, the cell is considered to have a conducting cell interior surrounded by a poorly conducting cell membrane. This was used to determine the cell's Clausius-Mossotti factor. In equation 2.31, the measured value of 19 mS/m was used for the medium conductivity of the external suspending medium, the calculated value of 24 mF/m^2 was

used for the membrane capacitance and values of 1 S/m, 100 S/m² and 5.5x10⁻⁹m were assumed for the conductivity of the cell interior, conductance of the membrane and thickness of the membrane respectively [10]. The Clausius-Mossotti factor is calculated to be 0.93 for a frequency of 1MHz, from a single shelled model.

The DEP force is calculated from equations 5.1 and the values used correspond to the experimental conditions applied as shown in figure 5.9. The absolute permittivity of the medium is taken as 7×10⁻¹⁰ CV⁻¹m⁻¹. The $\nabla|E|^2$ magnitude at a distance of 20 micron from the tip of the tweezers, with a radius of the tip of the electrode $r \approx 1\mu\text{m}$, separation between the electrodes $d \approx 4\mu\text{m}$, is found out to be $0.22 \times 10^{12} \text{ V}^2/\text{m}^3$ from the simulations. Using the values listed above the calculated value for DEP force is calculated to be roughly 0.15 pN. For a spherical cell moving slowly in a fluid due to an external force, the fluid drag force acting on the cell is proportional to the drag factor $6\pi\eta r$ and the instantaneous cell velocities in the x, y and z directions. The instantaneous velocity immediately after the initiation of cell movement can be obtained by solving equation 5.4 as indicated in chapter 2.

$$v = \frac{F_{DEP}}{6\pi\eta r} \quad (5.6)$$

In order to calculate the drag coefficient, the dynamic viscosity(η) of water is assumed to be approximately 8×10^{-4} PaS at 30°C. The drag coefficient is calculated to be roughly 0.1×10^{-6} Ns/m for a cell of radius 7 microns. The calculated velocity from equation 5.6 yields a value of roughly $\approx 1.5 \mu\text{m}/\text{sec}$. In the experiment performed, shown in figure 5.9, the instantaneous cell velocities at the time of voltage application were observed to be $\approx 1 \mu\text{m}/\text{sec}$. The measured value is therefore found to roughly agree with the calculated value.

Trapping can be made more selective by limiting the DEP force to a practical minimum, but these adjustments should be made after consideration of the experimental noise in the setup. The design and optimization process should also take into account that, the

DEP force is proportional to the cube of the radius of the cell, as a result the design parameters, such as the radius of the tip and the gap between the electrodes, must be scaled proportionally. Another important consideration in the design process is the tip diameter of the pipette as increased tip diameters results in large fluid displacement, which in turn causes significant disturbance to the settled cells.

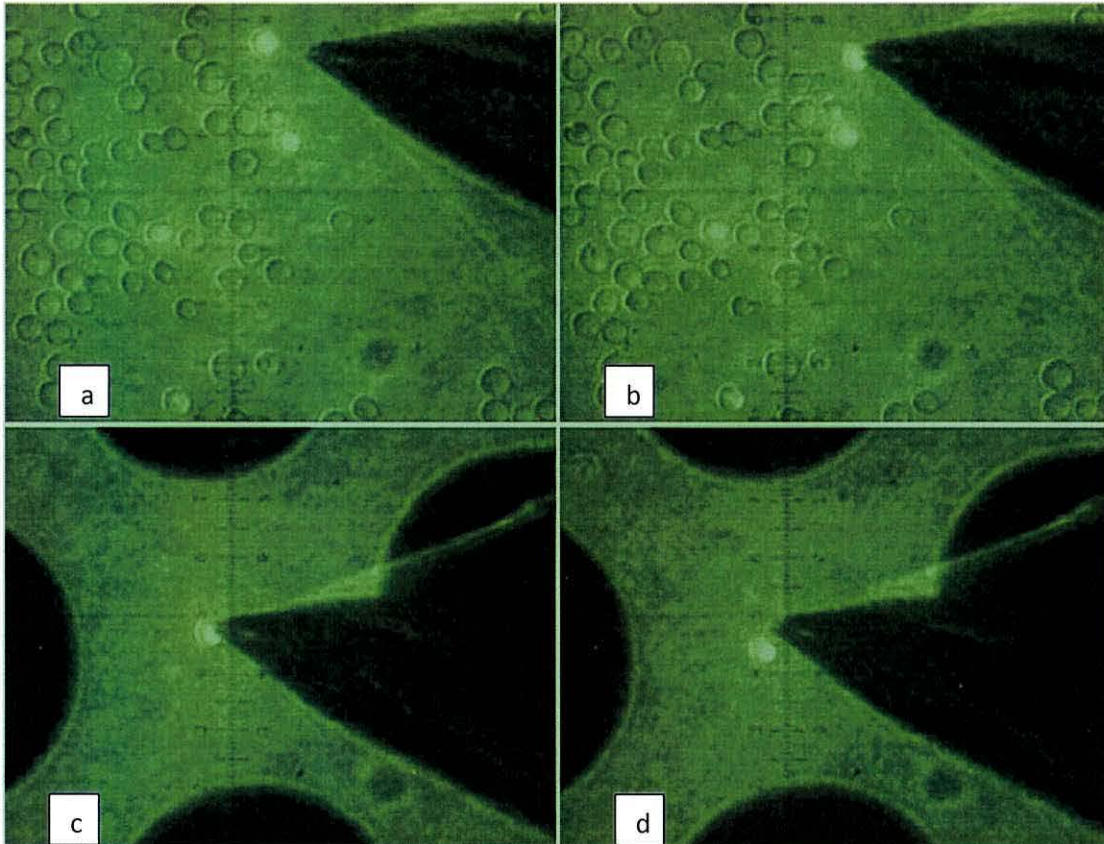


Figure 5.9: Images of cell Manipulation using a twin-wire electrode system, with the radius of the tip of the electrode $r \approx 1 \mu\text{m}$, and the separation between the electrodes $d \approx 4 \mu\text{m}$. The solution conductivity was 19 mS/m (a) The tip of the tweezers is positioned approximately $20 \mu\text{m}$ away from the centre of the target cell (diameter $\approx 14 \mu\text{m}$) (b) The electrode is energized at a frequency of 1 MHz and the cell is trapped around the high field region created around the tip of the etched wire (c) The trapped cell is positioned at the centre of a four electrode system. (d) The frequency is changed to 10 kHz in order to detach the cell and repel it towards a lower electric field intensity region.

In figure 5.9 a sequence of images demonstrates the ability of the twin-wire DEP tweezers to selectively manipulate a highly fluorescent transfected cell, determined using a fluorescence microscope. By changing between frequencies where HEI-193

cells shows positive DEP and negative DEP, the capture, positioning and release of the target transfected cell was demonstrated. A frequency of 1 MHz and a voltage of 1V (peak) was used to DEPally attract the target cell towards the two electrodes. Once the cell had been captured the voltage was lowered to 0.5V (peak) to limit cell damage upon exposure to high fields and to limit the effects of electrochemical cell adhesion to the electrode surface. By moving the micromanipulator, the trapped cell could be translated through the fluid at roughly 250 microns per second without escaping from the tweezers, over a distance of at least 5 mm. This suggests that the DEP holding force is large enough to overcome the hydrodynamic drag force. Once the cell was positioned in the required location the frequency was switched to 10 kHz to release the trapped cell through the action of negative DEP.

DEP cell separation techniques generally utilize the intrinsic bio-dielectric differences between different cell types to achieve their separation. The bio-dielectric differences were not used to achieve separation of the transfected and untransfected cells, since the dielectric differences were not easily quantifiable. The variability of GFP expression within the population of fluorescent cells is clearly visible in figure 5.9. Hence, the biological noise of the system limits us from utilizing the differences in the effective polarisability of the cells for sorting.

Across the range of conductivities from 19mS/m to 115mS/m the cross over frequencies were found to lie between 35 and 190 kHz. With increasing conductivity the interfacial electrical polarisability of the cell varies resulting in the DEP crossover frequency exhibiting a shift in the positive direction. This also has an effect on the magnitude of the repulsive and attractive force. Therefore by altering the conductivity of the suspending medium it is possible further optimize DEP trapping conditions. The experimental observations (not reported here) indicate increased undesired cell movement upon increasing ionic conductivity. This can be explained as an increase in

electrothermally driven fluid flow with the increase of solution conductivity. This effect is explained in detail in chapter 2.

In the case of the adherent HEI-193 cells, the effects of cell-substrate adhesive interactions on an unpassivated surface were found to be significant, making it very difficult to initiate cell movement on untreated substrates. These interactions could lead to deterioration in the performance of the device. The use of a passivating polyethylene glycol coating, as shown in this work, eliminates adhesive interactions.

It was found experimentally that applied voltages greater than 2 Volts (peak) and a tip radius that is lower than 0.5 microns resulted in rapid cell movement towards the electrode tips. This resulted in strong mechanical impact upon trapping and in most cases was found to cause bursting of the captured cell. From figures 5.4 and 5.5, the gradient of the square of the electric field intensity, and hence the velocity of DEP cell movement, exhibits sharp increases with increase in applied voltage and decrease in the electrode tip radius. The cell bursting could also be a result of large electrical stresses across the plasma membrane as described in chapter 3, and hence, it is critical that the generated field be minimized to limit the field induced stress across the plasma membrane. These effects should be less pronounced in non-mammalian cells such as plant, bacteria and yeast cells because of better mechanical integrity due to the presence of a cell wall.

5.4 Conclusion

A DEP based cell manipulator (tweezers) has been developed to separate and spatially manipulate individual cells of interest, such as the cells over expressing a protein tagged with GFP. The electrodes used in the DEP tweezers were electrochemically etched, and this allowed for good control of the geometric design parameters. This particular electrode tweezers offers many advantages such as high selectivity,

manufacturing ease, cell specific design. The isolation and lateral manipulation of single cells and the separation of transiently transfected cells has been effectively demonstrated with a success rate of 95%. The 5% failure was due to cells escaping at the time of translation from the pickup point to the point of release because of mechanical shock.

This method allows for early isolation and a distinct cost advantage over more conventional methods such as FACS. To obtain a better understanding of the influence of the design parameters and the applied voltage, simulations were performed using the finite element method. From the simulations it was deduced that varying the tip radius provides the most significant effect on both the maximum magnitude of $\nabla|E|^2$ observed at the apex of wires and also on the decay of the magnitude of $\nabla|E|^2$ with increasing distance from the apex of the wire.

The experimental results are found to correlate with the simulations after taking into account the biological heterogeneity and the manufacturing inconsistencies.

5.5 References

- 1) Martinoia, S., Bonzano, L., Chiappalone, M., Tedesco, M., Marcoli, M., and Maura, G., 'In vitro cortical neuronal networks as a new high-sensitive system for biosensing applications', *Biosensors and Bioelectronics*, 2005, 20, pp. 2071-2078
- 2) Pan, L., Xiang, G., Huang, L., Yu, Z., Cheng, J., Xing, W., and Zhou, Y., 'Automatic positioning and sensing microelectrode array (APSMEA) for multi-site electrophysiological recordings' *Journal of Neuroscience Methods*, 2008, 170, pp. 123-129
- 3) Xiao, F., Wei, Y., Yang, L., Zhao, X., Tian, L., Ding, Z., Yuan, S., Lou, Y., Liu, F., Wen, Y., Li, J., Deng, H., Kang, B., Mao, Y., Lei, S., He, Q., Su, J., Lu, Y., Niu, T., Hou, J., and Huang, M. J., 'A gene therapy for cancer based on the angiogenesis inhibitor, vasostatin', *Gene Therapy*, 2002, 9, pp. 1207-1213
- (4) Hack, J.N., Billups, B., Guthrie, B.P, Rogers, H.J., Muir, M.E., Parks N.T. and Kater, B.S., 'Green fluorescent protein as a quantitative tool', *Journal of Neuroscience Methods*, 2000, 95, pp. 177-184
- (5) Ashkin, A., Dziedzic, J.M., and Yamane, T., 'Optical trapping and manipulation of single cells using infrared-laser beams' *Nature*, 1987, 330, pp. 769-771
- 6) Chiou, Y.P., Ohta, T.A., and Wu, C.M., 'Massively parallel manipulation of single cells and microparticles using optical images', *Nature*, 2005, 436, pp. 370-372
- 7) Lee, H., Purdon, A.M. & Westervelt, R.M., 'Manipulation of biological cells using a microelectromagnet matrix', *Appl. Phys. Lett.*, 2004, 85, pp. 1063—1065
- 8) Neild, A., Oberti, S., Radziwill, G., and Jürg, 'Simultaneous positioning of cells into two-dimensional arrays using ultrasound', *Biotechnol. Bioeng.* 2007, 97, pp. 1335–1339
- 9) Yun, K.S. and Yoon, E., 'Micro/Nanofluidic Device for Single-Cell-Based Assay' *Biomedical Microdevices*, 2005, 7, pp. 35–40
- 10) Pethig, R., 'Dielectrophoresis: using inhomogeneous AC electrical fields to separate and manipulate cells', *Crit. Rev. Biotechnol.*, 1996, 16, pp. 331–348
- 11) Lee, K., Kwon, G.S., Kim, H.S., and Kwak, K.Y., 'DEP tweezers using sharp probe electrode', *Sensors and Actuators A*, 2007, 136, pp. 154–160
- 12) Hunt, P. T., and Westervelt, M.R., 'Dielectrophoresis tweezers for single cell manipulation' *Biomedical Microdevices*, 2006, 8, pp. 227–230
- 13) Ogata, S., Yasukawa, T., Matsue, T., 'DEP manipulation of a single chlorella cell with dual-microdisk electrode', *Bioelectrochemistry*, 2001, 54, pp. 33–37
- 14) Schnelle, T., Muller, T., Hagedorn, R., Voigt, A., and Fuhr, G., 'Single micro electrode DEP tweezers for manipulation of suspended cells and particles', *Biochimica et Biophysica Acta*, 1999, 1428, pp. 99-105

- 15) Chen, R., Greene, L.E., Collinsworth, G., Grewal, S.J., Houghton, O. , Zeng, H., Garnovskaya, M., Paul, V. R., and Raymond, R. J., 'Enrichment of transiently transfected mesangial cells by cell sorting after cotransfection with GFP', *Am J Physiol Renal Physiol*, 1999, 276, pp. 777-785
- 16) Chen, F.D. and Du, H., 'Simulation studies on electrothermal fluid flow induced in a DEP microelectrode system', *J. Micromech. Microeng.*, 2006, 16, pp. 2411–2419
- 17) Weiss, B., Hilber, W., Holly, R., Gittler, P., Jakoby, B. and Hingerl, K., 'DEP particle dynamics in alternating-current electro-osmotic micropumps', *Appl. Phys. Lett.*, 2008, 92, pp. 184101-184103
- 18) Li, H. and Bashir, R., 'On the Design and Optimization of Micro-Fluidic DEP Devices: A Dynamic Simulation Study', *Biomedical Microdevices*, 2004, 6, pp. 289–295
- 19) Jespersen, T., Grunnet, M., Angelo, K., Klaerke, D.A., and Olesen, S.P., 'Dual-Function Vector for Protein Expression in Both Mammalian Cells and *Xenopus laevis* Oocytes', *BioTechniques*, 2002, 32, pp. 536-540
- 20) Salvador-Recatalà, V., Schneider, T., and Greenberg, M.R., 'A typical properties of a conventional calcium channel β subunit from the platyhelminth *Schistosoma mansoni*' *BMC Physiology*, 2008, 8, pp. 1-11
- 21) Woo, H.D., Kang, H., and Park, M.S, 'Fabrication of Nanoscale Gold Disk Electrodes Using Ultrashort Pulse Etching', *Anal. Chem.*, 2003, 75, pp. 6732-6736
- 22) Pethig, R., Jakubek, L., Sanger, R.H., Heart, E., Corson, E., and Smith, P.J.S., 'Electrokinetic measurements of membrane capacitance and conductance for pancreatic β -cells', *IEE. Proc.-Nanobiotechnol.*, 2005, 152, pp. 189-193

Chapter 6

Assembly of 3-D Cell Structures using Dielectrophoresis

6.1 Introduction

Tissue engineering has gained significant interest in the last couple of years because of the ability to artificially engineer tissues to replace damaged organ tissues. The treatment involving tissue and organ replacement is still heavily reliant on obtaining suitable donors. This donor limitation has led to the development of alternative methods such as the use of stem cells and tissue engineering. Engineered skin, cartilage, blood vessels and bladders is currently being exhaustively tested as viable alternatives to donor replacement [1-3]. The use of micro-technologies is also becoming common as a means to producing these engineered tissues [4].

The engineering of artificial 3D cell constructs will also facilitate research into how cell-cell interactions and intercellular transport events evolve in three dimensional cell aggregations. Most *in vitro* studies of the electrophysiological properties of cells have employed 2D cell cultures and this is not the way cells exist in complex living organisms. The signaling mechanisms that take place in organs and tissues, which occur in three dimensions, are significantly different from those that take place in 2D cell cultures. Two examples are provided below.

Cells normally adhere to their neighbours and the substrate by means of adhesion complexes, also known as tight junctions, composed of transmembrane components connected to cytoplasmic proteins and the cytoskeleton. It is now thought that these complexes not only mediate adhesion but are also engaged in the transmission of

signals from the plasma membrane to the nucleus to regulate cell proliferation and differentiation. A second type of physical association between cells, the gap junction, forms a low resistance pathway allowing direct communication from one cytosolic compartment to another, transmitting both electrical and chemical information. These complexes have been proposed to be critical in coordinating the secretory activity of the islets of Langerhans [5, 6]. There are reported differences in the composition of cell-cell junctional complexes for cells forming three-dimensional, compared to those forming two-dimensional (monolayer), assemblies [7]. This lack of a three-dimensional attribute, as well as the cues that result from the physico-chemical properties of a normal *in vivo* extracellular matrix, are known to alter cell-cell signaling events of tumor cells, stem cells and differentiated cells [8-10], as well as gene expression [7]. The work described in this chapter formed part of a collaborative project with Dr Peter Smith of the Biocurrents Research Center at the MBL, Woods Hole. A long-term objective is to find evidence for self-organizing processes within three-dimensional assemblies of insulin secreting cells through for example, detection of synchronous electrical activity, calcium fluxes and insulin release. *In vitro* self-organisation of cells in an artificial three-dimensional construct has recently been described for spheroids composed of hen embryo neurons [11]. These spheroids were cultured using cells derived from hen embryo neuroepithelial tissue. The neuronal networks in these artificial spheroids behaved significantly differently from monolayer cultures, even to the extent that single spontaneous action potentials were recorded.

Artificially engineered cell assemblies also offer an alternative method to potentially study *in vitro* the effects of drugs in three dimensional cell clusters [12]. These studies might also be used as a model to perform drug based screening *ex vivo* and hence provide us with a better insight into the treatment of actual tumors.

Engineering of artificial cell constructs is mostly being done in extracellular matrices called scaffolds. Scaffolds are structures which are porous and allow the supply of nutrients and the removal of waste. They can be made from bio-materials or synthetic polymers. In this method the cells are seeded onto the scaffold and with time the cells start to migrate into the pores of the scaffold to form three dimensional structures. A number of scaffold materials such as hydrogels, porous calcium phosphate, and chitosan is being used by several groups [13, 14]. The main limitation of this method is the time required to obtain cell clusters of sufficient density from the initial sparse distribution of cells and it also does not allow achieving precise positioning and complex patterning.

In order to grow tissues with well defined architectures it is important that to be able to accurately control the assembly and architecture of the cell constructs. Dielectrophoresis provides us with the ability to manipulate large numbers of suspended biological matter in a spatially regulated manner [15].

The work in this chapter is focused towards determining the physical conditions necessary for the dielectrophoretic assembly of 3D cell clusters. The primary aim of this study is on understanding the electrophysiological properties of insulin-secreting cells (primary β -cells, as well as BETA-TC-6 and INS-1 insulinoma cells) as they transform from a monolayer cell culture to a three-dimensional construct that mimics localized structures (known as islets of Langerhans) that exist within the pancreas. We are extending the capabilities of electrochemical sensors and probes already developed in our laboratory [e.g., 16-18] and the method of DEP for the construction of these three-dimensional 'pseudo-islets' was employed. The long-term objective is to use these artificial cell structures to study cell-cell communication through junctional complexes and to understand how this controls the synchronous functioning of islets.

The 3D microelectrode geometry which was used in this chapter for cell aggregation was reported by Fatoyinbo *et al* [19] and it was used for rapid determination of dielectric properties of biological cells. The differences in cell aggregation between the well known quadrupole electrode geometry and the 3D electrode design were briefly compared.

The hope is this will lead to new cell-based assays for drugs, or the engineering of islet implants, to alleviate diabetes.

6.2 Simulations

For a fixed biological system and suspending medium the variation of the gradient of the square of the electric field strength ($\nabla|E|^2$) is the parameter that will mainly influence dielectrophoretic cell movement. The spatial variation of the magnitude of $\nabla|E|^2$ will determine the efficiency of dielectrophoretic patterning and hence it is important to simulate the effect of varying the design geometry. The overall aim of these simulations is to predict the behavior of the particles under non-uniform AC electric fields created using quadrupole and 3D electrode geometries. Using the simulations, a study of geometrical and design determinants which influence the experimental conditions were carried out. In general, negative DEP forces in thin film microelectrode devices will always repel particles away from electrode edges.

All the simulations have been performed considering it is a static case of 1V (peak). The colour plot in figure 6.1 shows the magnitude of the term $\nabla|E|^2$ simulated for the quadrupole electrode geometry. The changes in the direction of $\nabla|E|^2$ along a vertical plane is expressed by an arrow plot in the middle of two aligned opposite electrodes in a quadrupole arrangement, extended to a height of 250 microns above the surface of the electrodes. The boundary conditions are zero charge everywhere except on the

electrodes, where a voltage is applied. The adjacent electrodes are given a static potential difference of 1V (peak).

The vectors indicate the direction of cells undergoing negative DEP into the centre of the gap between the electrodes and it indicates that the cells will accumulate at the centre of the four electrodes. Even though it is possible to concentrate particles in the negative DEP mode using polynomial electrodes, the simulations show that the trapping forces are directed into the bulk of the fluid and not onto the surface of the substrate. Because of this the cell clusters tend to be very susceptible to slight fluid disturbances and as the cells begin to build up beyond a certain height they lose their structural integrity and hence the structures start collapsing. Thus, this electrode geometry is not very suitable to form well-built 3D structures.

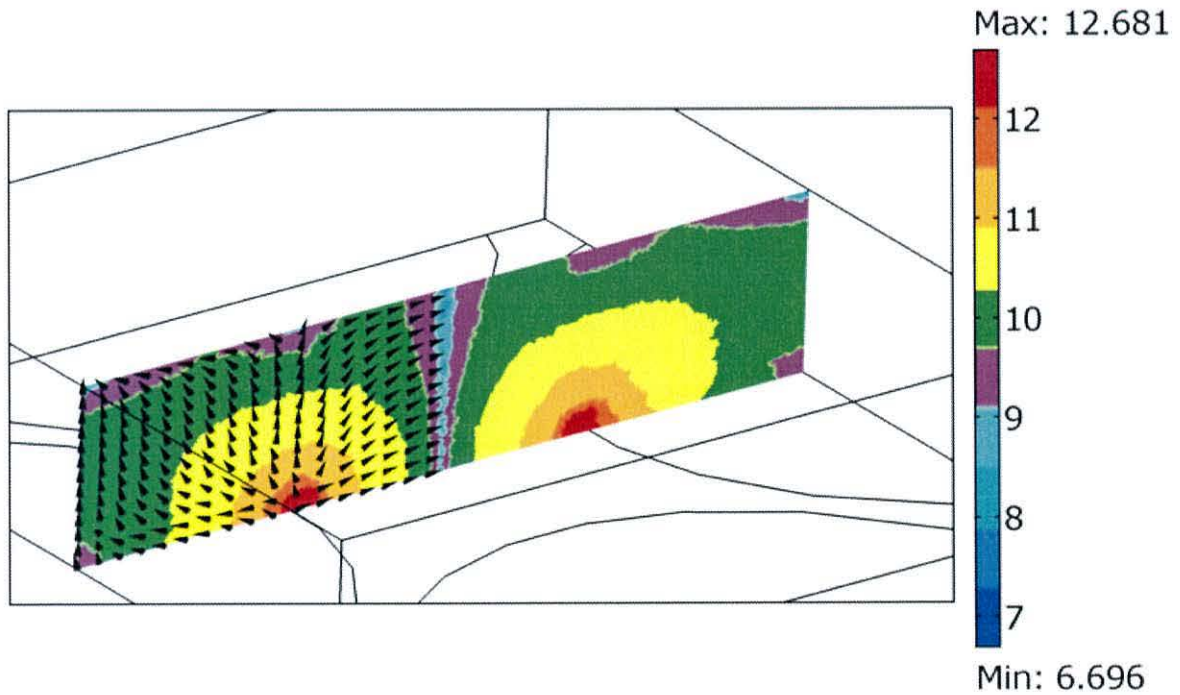


Figure 6.1: A section along a vertical plane in the middle of the two aligned electrodes showing the magnitude of $\nabla|E|^2$ (V^2/m^3 , \log_{10} scale). The arrows represent the direction of the Negative DEP force. The spacing between the two opposite electrodes is 400 microns.

In order to establish a dense cell construct with high structural integrity, an alternative electrode design was also investigated. This 3D electrode design contains a bottom and top electrode. The bottom electrode contains patterned circular breaks and the top

electrode is a thin conducting film. The schematic of the cell aggregation and layout is shown in figure 6.2.

The modelling described here is used to determine that for a fixed concentration of cells in the initial suspension, the overall size, shape and cell density of the cell construct is determined by the diameter and relative locations of the patterned holes and by the distance between the top and bottom electrodes. To demonstrate the effects of the electrode geometry parameters, simulations were carried out by varying the diameter of the patterned break (d), spacing between two adjacent circular patterns (s) and the height of the chamber (h). All the simulations were performed for a static case of 1 Volt (peak). The $\nabla|E|^2$ magnitude can be determined for different signal amplitudes by using the relationship that $\nabla|E|^2$ scales as a function of the square of the voltage.

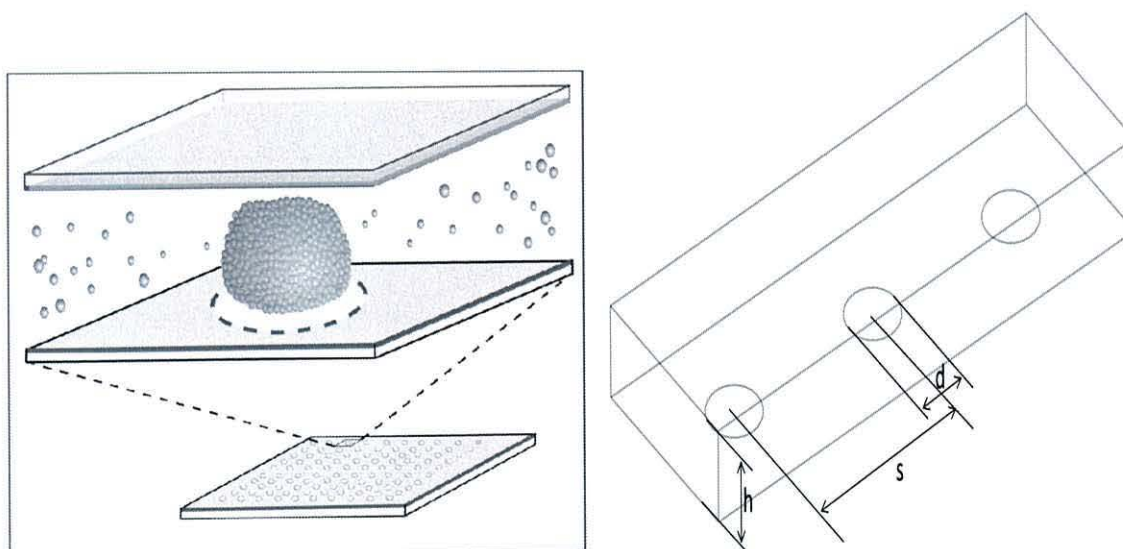


Figure 6.2: (a) Schematic of cells directed by negative DEP force to form an aggregate of cells. Other cells are pushed away into the bulk perfusate. (b) Schematic of a 3D electrode design showing the various design parameters that influence cell patterning.

It can be seen from figure 6.3; the $\nabla|E|^2$ magnitude plot repeats itself mid-way between the two patterned breaks and hence by controlling the spacing between adjacent electrodes, the density of the cell aggregation can be controlled as more cells around

the vicinity of the patterned hole will experience a significant DEP force. It is important to note that the magnitude of $\nabla|E|^2$ diminishes rapidly further away from the patterned electrode hole and hence the distance between the electrodes must be set to a dimension such that the cells are under the influence of a strong DEP force which causes it to move towards the patterned circular break, this is demonstrated in figures 6.3 and 6.4.

From figure 6.5, when the diameter of the patterned hole (d) is decreased to 100 microns, the peak magnitude of $\nabla|E|^2$ around the edges remains unchanged. The magnitude of $\nabla|E|^2$ is higher at the centre of the circular break, but further away with increasing x, y and z dimensions, the $\nabla|E|^2$ value diminishes more rapidly since the electric field non-uniformities do not extend as far as when the diameter is 200 microns. If the aspect ratio (height/ width) of the cell construct required is large, the reduction in diameter is a possible way of achieving it.

The height of the chamber (h) also has a significant effect which can be seen from figure 6.6. On comparing the change in height from 200 microns to 100 microns, we observe that the magnitude of $\nabla|E|^2$ around the electrode edges increases with decrease in the height of the two electrodes. The magnitude of $\nabla|E|^2$ immediately above the circular break and the $\nabla|E|^2$ magnitude further away is also larger; hence, by decreasing the height the holding and capturing force is also increased. However, this also holds a drawback by limiting the formation of larger cell constructs because the top electrode also acts as a physical barrier. The height of the chamber must therefore be calculated taking into account these considerations.

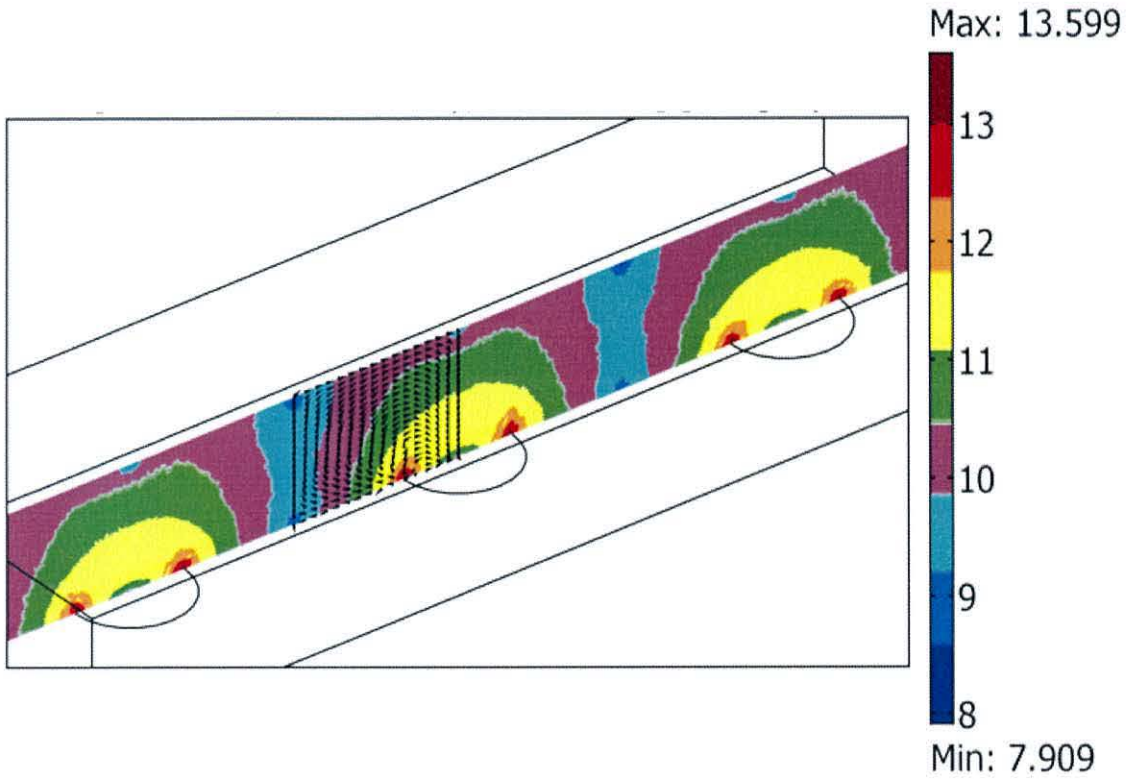


Figure 6.3: A plane along the middle of three patterned breaks showing the magnitude and direction of $\nabla|E|^2$ (V^2/m^3 , \log_{10} scale). The geometry parameters are $d=200\mu m$, $s=600\mu m$ and $h=200\mu m$.

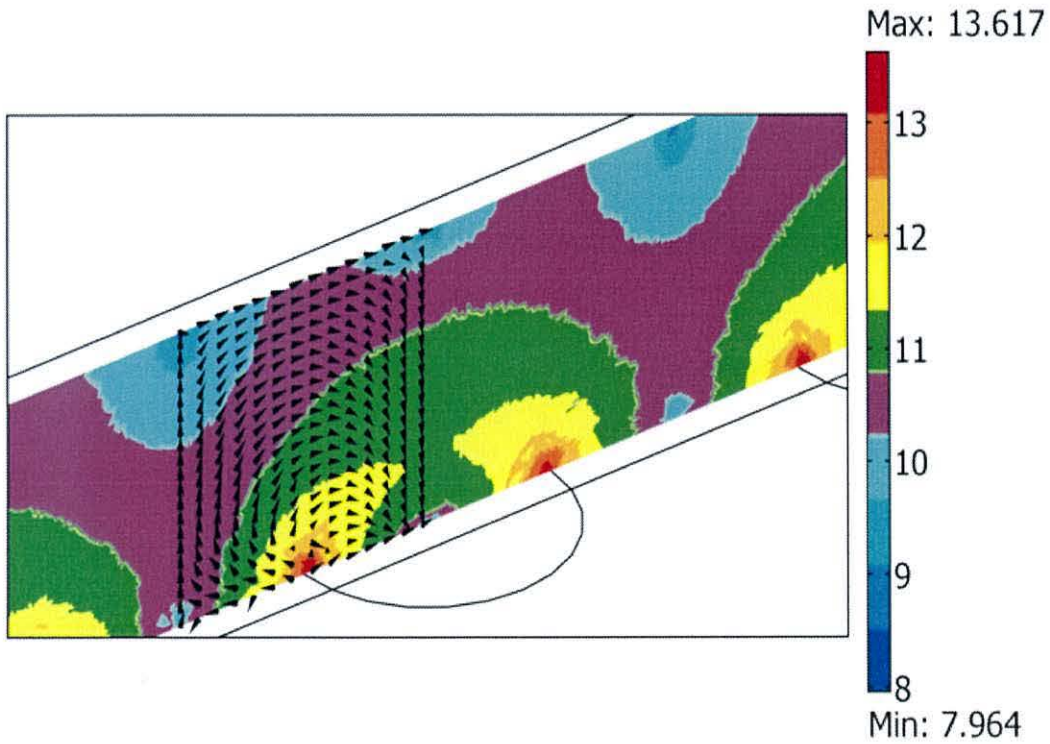


Figure 6.4: A plane along the middle of three patterned breaks showing the magnitude and direction of $\nabla|E|^2$ (V^2/m^3 , \log_{10} scale). The geometry parameters are $d=200\mu m$, $s=400\mu m$ and $h=200\mu m$.

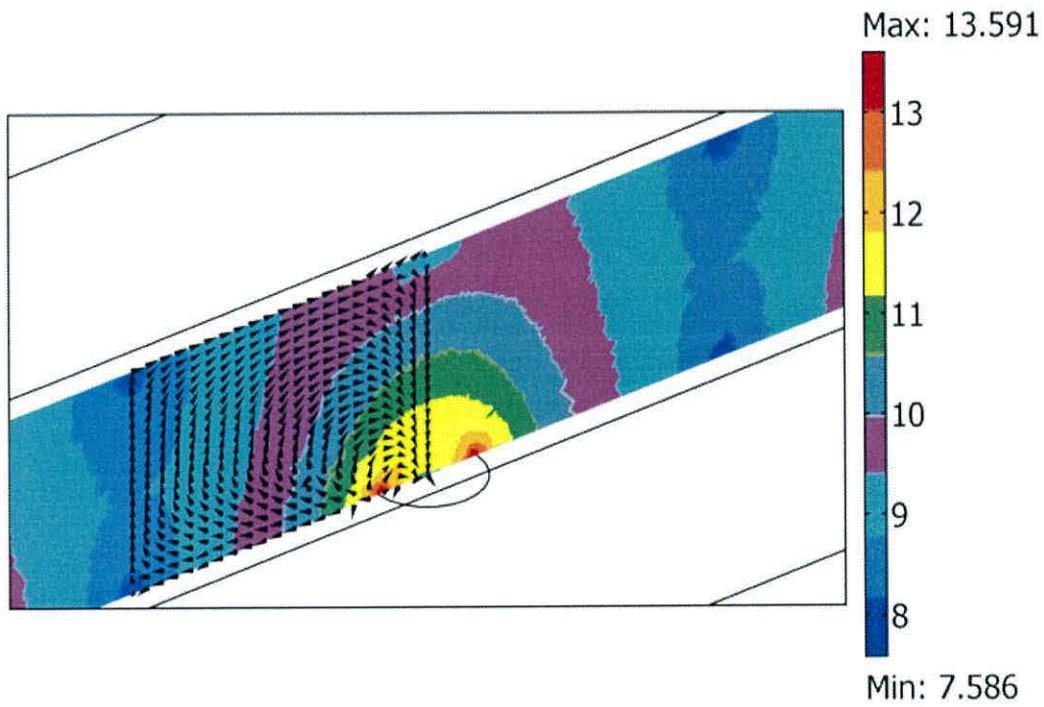


Figure 6.5: A plane along the middle of three patterned breaks showing the magnitude and direction of $\nabla|E|^2$ (V^2/m^3 , \log_{10} scale). The geometry parameters are $d=100\mu m$, $s=600\mu m$ and $h=200\mu m$.

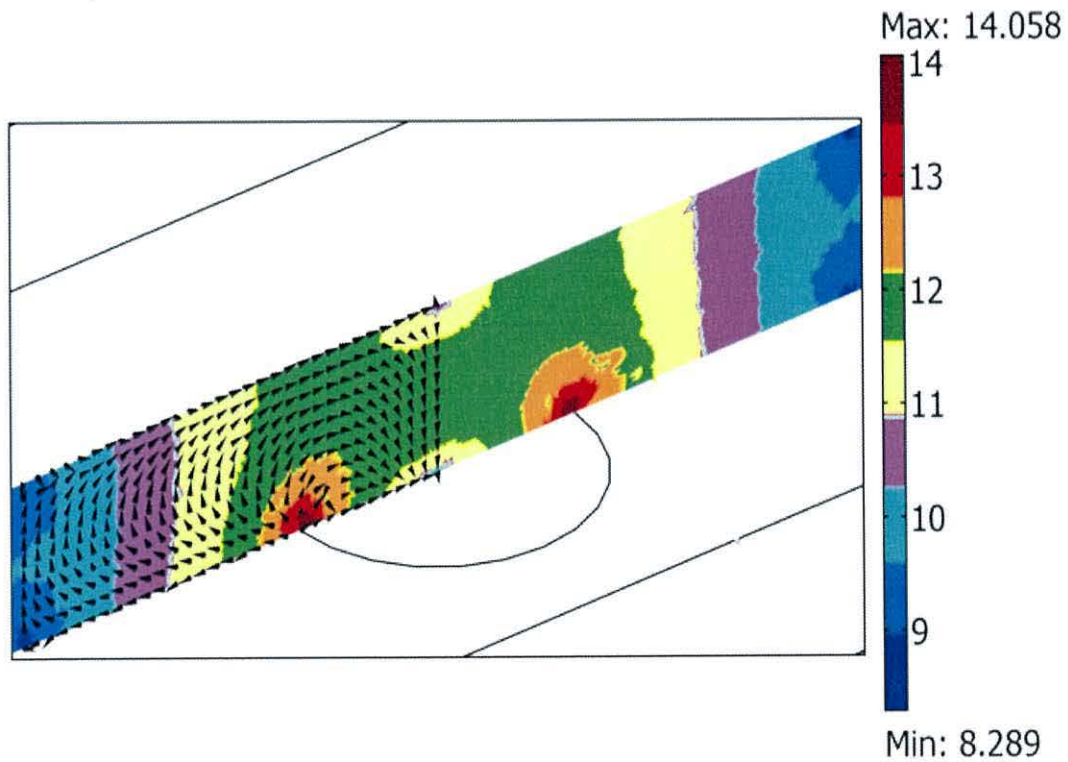


Figure 6.6: A plane along the middle of three patterned breaks showing the magnitude and direction of $\nabla|E|^2$ (V^2/m^3 , \log_{10} scale). The geometry parameters are $d=200\mu m$, $s=600\mu m$ and $h=100\mu m$.

6.3 Devices and methods

6.3.1 Device manufacture

The DEP chamber shown in figure 6.7 comprises of two ITO patterned microscope slides spaced $220\mu\text{m}$ apart. The spacer was made by spin coating PDMS onto the ITO slides and then by peeling away the central section in order to create the chamber and encased in poly-dimethylsiloxine (PDMS). 1 mm diameter holes were drilled into the top glass slide to form fluidic inlet and outlet ports. The inner surfaces of the slides were coated with electrodes of indium tin oxide (ITO) of thickness $\sim 110\text{nm}$ and specific resistance $\sim 10\Omega/\text{sq}$. The continuity of the ITO layer of the top slide was disrupted by a 10×10 array of holes. The holes are arranged in rough correspondence to a 1536 microtitre plate format.

Each hole, of diameter $200\mu\text{m}$ and spaced $600\mu\text{m}$ apart, was fabricated by machining away the ITO layer, down to the glass substrate, using a pulsed excimer laser technique [20]. Fabrication was performed using a S8000 Excimer laser micromachining system. We employed a 248 nm excimer laser and a fluence of roughly 1.5 J cm^{-2} . A process called image projection was used, where the image on the mask (in this case a 2mm diameter circle) was projected through a lens of magnification 10x onto the ITO substrate. The mask was kept static, while the work piece was moved to create a 10×10 array of $200\mu\text{m}$. These holes create repeated patterns of electric field non-uniformities in what otherwise would have been a uniform field between the capacitor-like plates of the DEP chamber. Cells located in a region of field non-uniformity will experience a DEP force of magnitude proportional to the product of the local field and the field gradient.

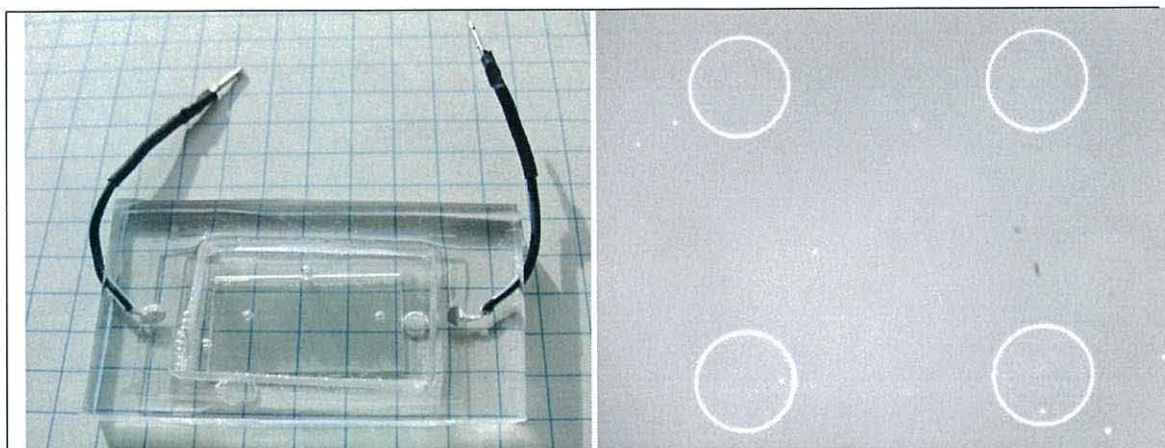


Figure 6.7: (a) The DEP chamber (left) consisted of two ITO-coated microscope slides, spaced 220 μm apart, encased in poly-dimethylsiloxine (PDMS). 1 mm diameter holes were drilled into the top wall and were used as fluidic ports. (b) Shows four of the 10x10 array of 200 μm diameter laser machined into the ITO layer of the top electrode.

6.3.2 Cell Preparation

The biological system that we used for testing the quadrupole electrode geometry consisted of tumor cells derived from an immortalized schwannoma cell line, HEI 193. The HEI 193 cell culture and preparation for the DEP experiments is described in chapter 5.

The INS-1 and BETA-TC-6 cells (rat and mouse insulinoma β -cells, obtained from ATCC, Manassas, VA) were cultured using standard procedures [21] summarized here. The cells were grown in RPMI 1640 medium (Invitrogen) supplemented with 11 mM glucose, 10 mM HEPES, 10% heat-inactivated fetal calf serum, 2 mM L-glutamine, 1 mM sodium pyruvate, 50 μM β -mercaptoethanol, and 100 $\mu\text{g/ml}$ penicillin–streptomycin. A humidified incubator was used and maintained at 37°C with 5% CO_2 , 95% air. Immediately before the experiments, the cells were dislodged from the culture vessels by trypsinization, and washed twice in the media to be used in the DEP and electrorotation measurements (see below).

Cell suspending solutions of physiological osmolarity were prepared for electrorotation and DEP experiments. Solutions of three different conductivities were prepared for the

electrorotation studies. A solution of conductivity 11.8 mSm^{-1} contained 2mM glucose, 5.5 mM Hepes buffer, and was adjusted to 300 mos by adding 96 gL^{-1} sucrose. The pH was adjusted to pH 7.4 using NaOH, and the final conductivity was obtained by adding 0.1M KCl. For the other preparations a stock solution was prepared, comprising: 140 mM NaCl; 5.4 mM KCl; 2.5 mM CaCl_2 ; 0.5 mM MgCl_2 ; 11 mM glucose and 5.5 mM Hepes buffer. A solution of conductivity 104 mSm^{-1} was prepared by adding 8 mL of this stock solution to 92 mL double-distilled water, plus 8.47 g sucrose to give 300 mos. A 55 mSm^{-1} solution was prepared by doubling the dilution of the stock solution and adding 10.39 g/L sucrose to balance the osmolarity. The conductivities were measured at $22 (\pm 0.5) ^\circ\text{C}$, to within $\pm 0.25\%$, using a YSI 3200 Conductivity Instrument (probe constant $K = 1.0/\text{cm}$).

6.3.3 Nanosensor Preparation

6.3.3.1 PEBBLEs Preparation

A long-term objective of this work is to monitor the electrophysiological properties of insulin-secreting cells (primary β -cells, as well as BETA-TC-6 and INS-1 insulinoma cells) in real-time, as they are formed into three-dimensional constructs using the DEP procedure described here. A potentially promising method for minimally invasive intracellular monitoring of key biological components (e.g., potassium, oxygen, calcium and pH) would be to incorporate nanosensors, rather than free dyes, directly into the artificial constructs at the time of their formation. To this end, the use of fluorescent nanosensors termed PEBBLEs (Probes Encapsulated By Biologically Localized Embedding') [22, 23], was investigated. These sensors, based on polyacrylamide, cross-linked decyl methacrylate, and silica-based sol-gel nanoparticle fabrication technologies, have been characterized in aqueous solution and also tested in intracellular surroundings. Each matrix can be used to encapsulate specific dyes,

ionophores, or enzymes to produce spherical sensors of the order 100 nm in diameter. Following proven protocols [22, 23], an acrylamide-based nanosensor to monitor extracellular pH, and another based on sol-gel encapsulation of an oxygen-sensitive platinum porphyrin dye, was investigated.

In the experiments to incorporate these nanosensors into the DEP-assembled cell aggregations, 2mg/ml of filtered, washed and air-dried PEBBLEs were added to the cell suspensions before admission into the DEP chamber. The glucose concentration in the suspending medium was increased to 10 mM, by adding 0.18gm glucose plus 97ml double-distilled water to 3ml of the electrorotation stock solution, and adjusting the osmolarity to 300 mos by adding 92.2 gm/Lsucrose. The conductivity of this medium was 51.5 mS/m. Negative DEP was used to condense a suspended mixture of cells and fluorescent nanosensors into an array of three-dimensional cell constructs.

6.3.3.2 Functionalised Silica Nanoparticles

The use of silica nanoparticles for the application and testing of an extracellular sensor for pH was also undertaken. This was carried out for the measurement of extracellular pH of artificially constructed tumours. It has been reported in the literature that tumours cause acidification of the extracellular media [24] and hence this study can be a very useful to understanding this process. These silica nanoparticles were surface modified to adhere to the fluorescein indicator and to the plasma membrane, as shown in figure 6.8. Atomic Force Microscopy (AFM) was used to determine the size of the nanoparticles and it was found to be roughly 100 nm in diameter. This study was carried out in collaboration with Amit Basu's group at Brown University.

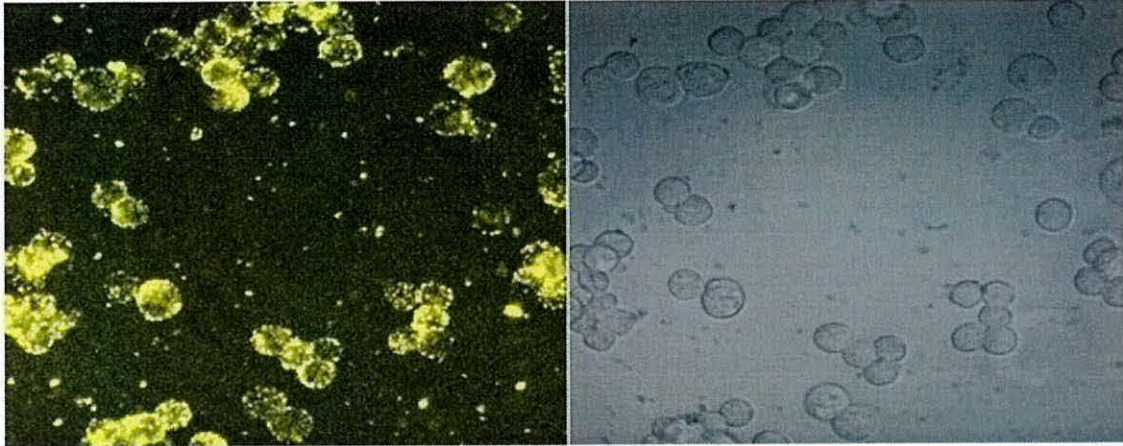


Figure 6.8: Short term exposure of 30 minutes to the fluorescein conjugated nanoparticles provides localization on the cell membrane

6.4 Results and discussion

The new 3D electrode design was initially tested using a polystyrene bead suspension. A saline solution with a conductivity of 8mS/m was used and the AC voltage frequency and magnitude was fixed at 1 MHz and 10 V (peak) respectively. At this frequency the polystyrene beads are found to experience a fairly strong negative DEP force. The voltage used was set to 10 V (peak). As seen from figure 6.9, the particle densities are fairly low and it is possible to increase the size of these cell clusters by merely increasing the particle density in the fluid. Upon energizing the electrodes the beads were found to follow the trajectory shown by arrows in previous simulations. DEP-induced particle clusters were found to form within 1½ minutes, as shown in figure 6.9.

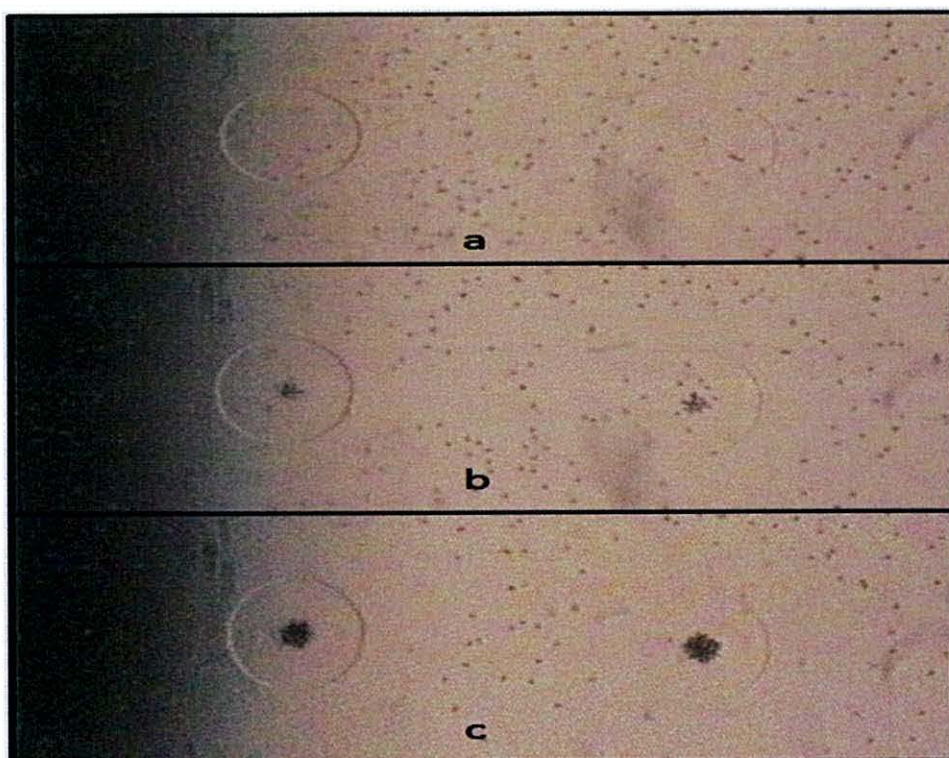


Figure 6.9: Aggregation of 4.50 micron polystyrene beads in a chamber with patterned ITO electrodes at the bottom and a plain ITO electrode on the top separated by a distance of roughly 220 microns. (a) Image captured after loading of the bead suspension (b) 40 seconds later (c) 1min 25secs later.

Before attempting to manipulate the insulinoma cells into three-dimensional constructs by DEP, knowledge of their electrokinetic behavior in electrolytes of known conductivity was required. In particular, it was important to predict the experimental conditions required to generate either positive or negative DEP movement of the cells. This information was derived using a contact-free method known as electrorotation, and was performed as described in previous work on INS-1 cells [25]. In brief, the suspended cells ($\sim 2 \times 10^5$ cells/ml) were subjected to a rotating electric field, and their electrorotation responses were visualized using a Zeiss Axioskop and recorded at 30 frames/sec for later analysis on a TV monitor. The diameter of the cells could be determined to an accuracy of $\pm 0.3 \mu\text{m}$. The mean values obtained for the cell radius r , and the frequency f_{pk} at which the anti-field electrorotation rate was a maximum, are shown in figure 6.10. The best linear fit values were obtained using Origin, OriginLab.

The average radius of the INS-1 cells ($n = 91$) was determined to be $5.28 (\pm 0.69)$ microns, and $5.07 (\pm 0.64)$ microns for the BETA-TC-6 cells ($n = 97$).

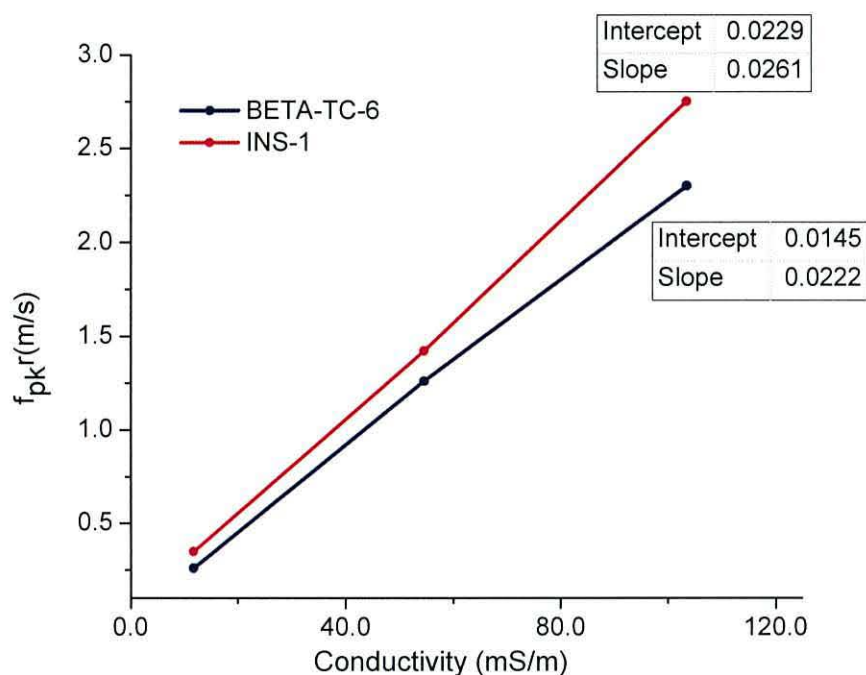


Figure 6.10: Plots of the electroration data for the INS-1 and BETA-TC-6 cells. The lines represent the variation of the peak rotation rate vs. solution conductivity.

Based on the relevant theory and experimental conditions [25], a plot of $f_{pk} r$ against solution conductivity should be linear (of the form $y = mx + c$) and of slope m given by

$$m = \frac{1}{\pi C_m} \quad (6.1)$$

with an intercept c given by

$$c = \frac{mrG_m}{2} \quad (6.2)$$

In these equations C_m is the capacitance per unit area of the cell membrane, and G_m is the total effective membrane conductance. This total conductance comprises contributions arising from the passive conduction of ions on the surface and across the membrane [25].

From equation 6.1, with slope values m of 26 and 22 $\text{m}^2\text{S}^{-1}\text{s}^{-1}$ given in figure 6.10, membrane capacitance values of 12.2 and 14.5 mFm^{-2} are derived for the INS-1 and BETA-TC-6 cells, respectively. This result for the INS-1 cells falls at the upper end of the range of values of 10.65 (± 2.1) and 10.23 (± 2.1) mFm^{-2} obtained in previous electrorotation studies [25]. Membrane capacitance values correlate closely with the extent to which the area of an otherwise smooth membrane surface is increased as a result of the presence of membrane folds and proturbances, such as blebs and microvilli. The larger capacitance values obtained in this present work can therefore be interpreted as the cells having a more complex surface morphology. This possibly reflects that the cells used in the previous work [25] were harvested from a relatively old culture (number of passages greater than 20), whereas the cells used in this present study were obtained from passages 5-7 of a fresh culture. Repeated passaging of insulin secreting cells is known to correlate with a loss of vesicle fusion [22]. This would be expected to correspond with a less 'detailed' membrane surface. The BETA-TC-6 cells used in these studies appear to exhibit a more complex membrane surface morphology than the INS-1 cells. Based on the intercept values of 0.023 and 0.015 ms^{-1} given in figure 6.10, together with the average radius values of 5.28 (± 0.69) and 5.07 (± 0.64) μm , from equation 6.2, values for the total effective membrane conductance of 340 (± 45) and 274 (± 35) Sm^{-2} are obtained for the INS-1 and BETA-TC-6 cells, respectively. The conductance values observed for the INS-1 cells overlaps that of 261 (± 85) Sm^{-2} obtained previously for this cell type [25]. From this data the DEP responses expected for the INS-1 and BETA-TC-6 cells can be derived, based on the smeared-out sphere model to describe the dielectric

polarisability of a cell [26]. Examples of this are shown in figure 6.11 to cover the full range, 10-120 mS/m, of the suspending medium conductivity used in this studies.

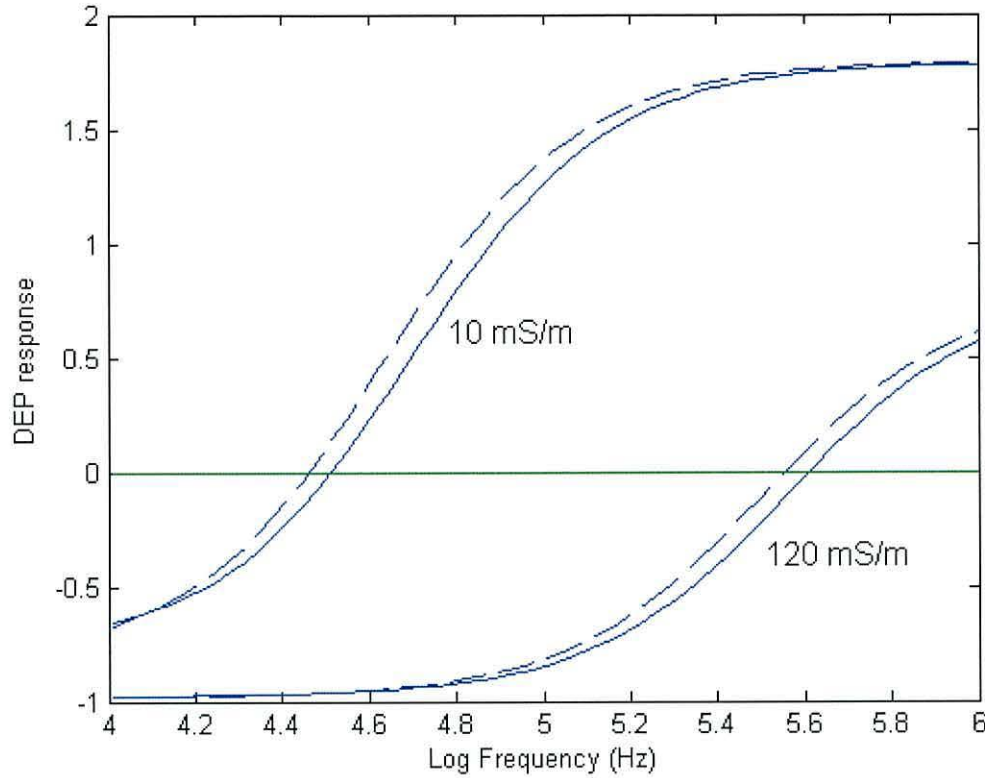


Figure 6.11: The dielectrophoretic responses derived for INS-1 cells (solid-lines) and BETA-TC-6 cells (dotted-lines), for two conductivity values of the suspending medium, using the *smear-out sphere* model of a cell [26]. Parameters used in this model included: radii values of 5.28 and 5.07 μm ; membrane capacitances of 12.2 and 14.5 mF/m^2 ; membrane conductances of 340 and 274 S/m^2 , derived for the INS-1 and BETA-TC-6 cells, respectively.

The results shown in figure 6.11 indicate that for an electric field frequency of 10 kHz, using isotonic suspending media conductivities of 25~75 mS/m, the INS-1 and BETA-TC-6 cells should be repelled from the ITO-holes by negative DEP. At frequencies around 100 kHz the cells should experience a weak or no DEP force, whilst for frequencies around 1-10MHz they should be attracted to the edges of the ITO-holes by positive DEP. Examples of this behavior are shown in figures 6.12 and 6.13. In figure 6.12, the action of a 10kHz, 14Vpk-pk, signal applied to cells suspended in a medium of conductivity 54.7 mS/m is shown to result in the cells being repelled from the ITO-

hole edges, either into the bulk fluid between the holes or, more importantly, into densely packed cell aggregations within the bulk fluid regions defined by the perimeters of the ITO-holes.

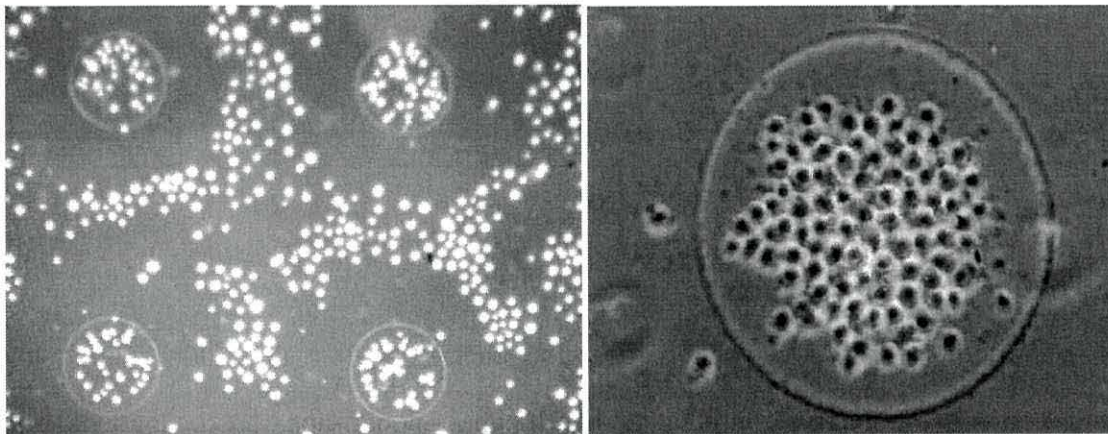


Figure 6.12: (Left) An image, taken through the top of the DEP chamber, of INS-1 cells ($\sim 5 \times 10^5$ cells/ml) directed by negative DEP away from the edges of four ITO-holes into the bulk perfusate, either outside or within the hole perimeter boundaries. (Right) BETA-TC-6 cells ($\sim 10^6$ cells/ml) directed by negative DEP into a densely packed assembly beneath a hole perimeter. Confocal microscopy revealed that this aggregate was $\sim 75 \mu\text{m}$ in height, corresponding to 7~8 stacked layers of cells. For each image the conductivity of the suspending medium was 54.7 mSm^{-1} , and a 10kHz, 14V pk-pk, signal was applied.

In figure 6.13, two sets of microscopic images provide evidence that the simple ITO-hole geometry can be used to manipulate cells located within the perimeters of the holes by both positive and negative DEP. The ability to push cells together and then pull them apart, repeatedly if desired, had previously been demonstrated using quadrupole electrodes [26], but the effect shown in figure 6.13 of cells being extracted from other cells was not expected. This result indicates that the simple ITO-hole geometry might also provide the means to selectively sort cells, according to their dielectric phenotype, before they are directed into cell aggregations.

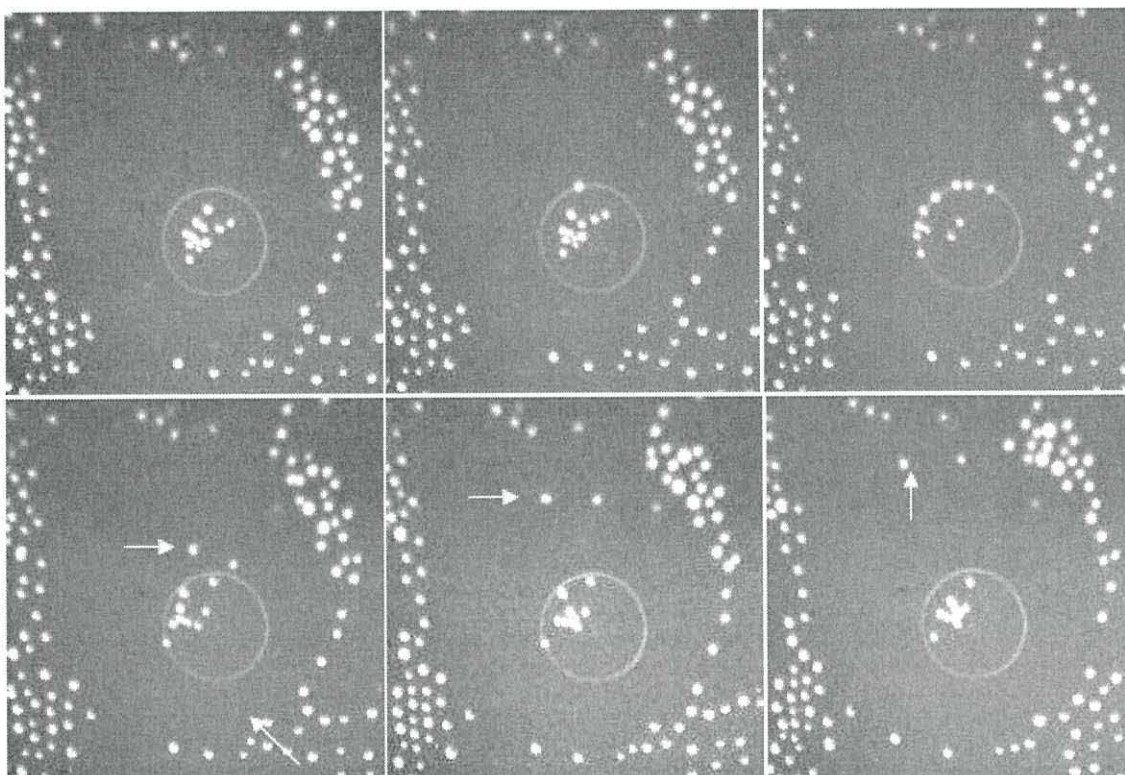


Figure 6.13: (Top) Sequence of three images of INS-1 cells ($\sim 2 \times 10^5$ cells/ml) being attracted to an ITO-hole edge by positive-DEP using a 15MHz, 14V pk-pk, signal. (Bottom) On changing the signal frequency from 15MHz to 1 kHz, the cells are then pushed away from the perimeter by negative-DEP. Two cells (arrowed) have escaped from the ITO-hole perimeter into the surrounding bulk fluid.

As shown in figure 6.14 it was also found that the excess cells, distributed in the bulk fluid between the ITO-holes, could be removed by flowing fluid through the DEP chamber whilst maintaining the integrity of the cell assemblies. With the negative DEP force in operation, the cell aggregations remained in place, even under conditions of very high fluid flow rates and mechanical agitation (including accidental dropping!) of the DEP chamber. However, as shown in figure 6.14, the cell aggregations did not survive the effect of a passing fluid-air meniscus. These results suggest that it would be possible to pass a gel forming solution through the DEP chamber, so as to encapsulate the cell aggregations in, for example, a porous hydrogel matrix that permits the passage of nutrients and by-products to and from the cells.

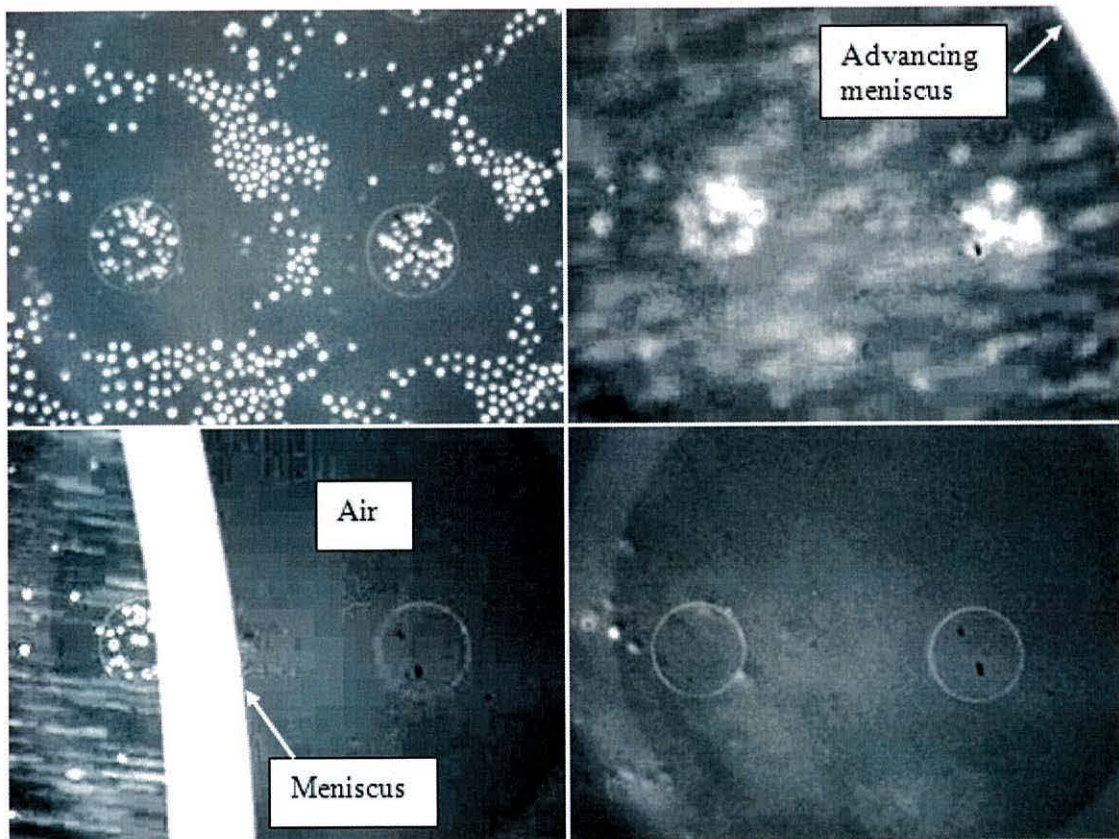


Figure 6.14: Microscopic images taken as the bulk fluid is removed from the DEP chamber, whilst maintaining a negative DEP force generated by a 10 kHz, 14V pk-pk, and signal. BETA-TC-6 cells held beneath the ITO-holes by negative DEP remain in place, even for high fluid flow rates, but are removed as the fluid-air meniscus advances (from right to left) past them.

Experiments were also performed to demonstrate that fluorescent PEBBLE nanosensors could be embedded into the cell assemblies, and used as real-time monitors of such parameters as pH and dissolved oxygen levels, shown in figure 6.15. The nanosensor particles were mixed with the cells prior to their admission into the DEP chamber.

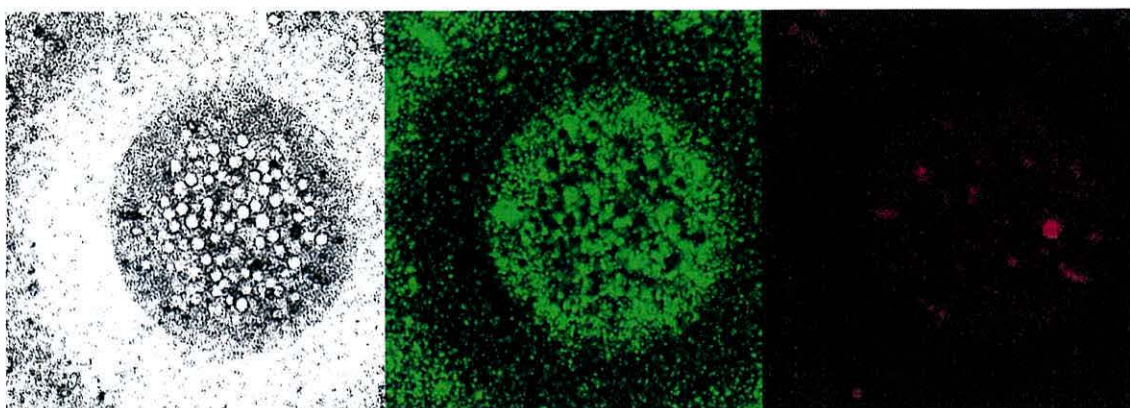


Figure 6.15: Shows images obtained using a Zeiss LSM-510, multiphoton confocal microscope, taken at a plane 60 μm below the top of a cell+PEBBLE assembly. These images demonstrate that the PEBBLE nanosensors were distributed throughout the cell aggregations. Furthermore, confocal microscopic examinations have shown that some aggregations were approximately 150 μm in diameter, 120 μm in height, and contained around 1000 cells. It is therefore possible to produce artificial cell constructs of the same size and cell density as a typical islet of Langerhans.

Because these experiments are done in a chamber the issue of accessibility and extraction of these cell aggregates is of concern. A low temperature gelling agar was used to immobilize the clustered cells. The process of extracting the thin film (220 microns) of agar was complicated as it disintegrated upon removal, because of poor mechanical strength. The concentration of agar (1%) in the DEP media had to be kept low, so that the viscosity increase upon addition of agar does not significantly dampen dielectrophoretic motion.

With collaborators at the MBL, Woods Hole, we are in the process of developing more accessible chambers in order to overcome this problem. We have also undertaken other tests using alternative electrode geometries such as the quadrupole electrode geometry.

In order to establish a comparative study, cell clustering experiments using quadrupole electrodes was carried out. These electrodes have been used extensively in the past for dielectrophoretic characterization and electrorotation experiments. In this particular

electrode setup, four coplanar thin film electrodes with no top plate were used. In figure 6.16, the electrodes are energized such that the adjacent electrodes have a peak value of 7 V and a frequency of 10 kHz for medium suspending conductivity of 48 mS/m. Using the quadrupole electrodes it was not possible to develop cell clusters which were more than 3 to 4 cells high because the cell aggregations begin to loose their structure and eventually start collapsing. Unlike the 3D electrode design, the cell cluster formations begin to loose their structural integrity and instead of the cells layers piling up as a stack, it begins to spread horizontally.

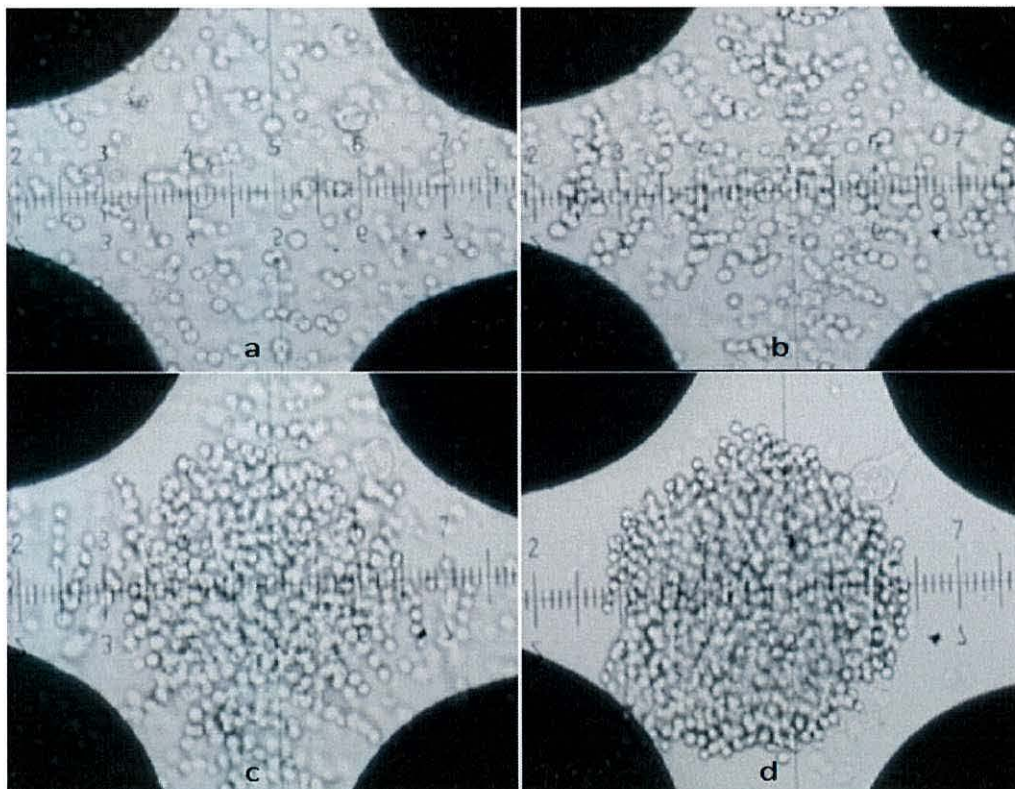


Figure 6.16: Schwannoma cell aggregation using polynomial quadrupole electrode geometry. (a) Initial cell distribution (b) 50 secs later; (c) 2 mins later; (d) 8 mins later

The localization of fluorescein conjugated nanoparticles was also carried out using the quadrupole electrode design shown in figure 6.17. Fluorescein is pH sensitive and hence it enables us to detect possible changes in the extracellular space. The cells were exposed to the fluorescent nanoparticles for a short period of time (30 mins).

When schwannoma cells were exposed to fluorescein conjugated nanoparticles for this short time period, the nanoparticles appeared to localise on the cell membrane.

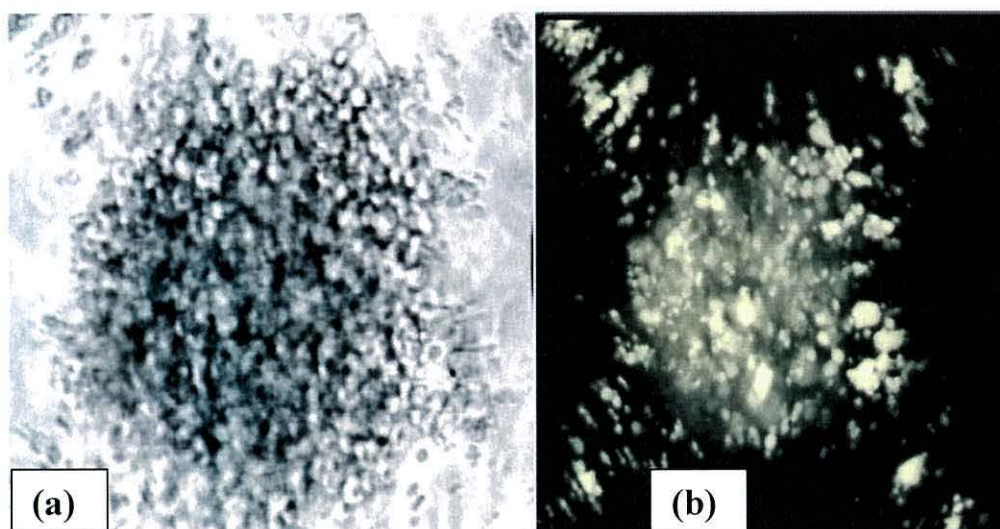


Figure 6.17: Quadrupole electrodes used to form an artificial cell cluster incubated with nanoparticles (a) Brightfield image. (b) Visualized using a 488 nm excitation laser.

Although the quadrupole electrode geometry offers an alternative for loosely packed, low height cell aggregations, this geometry would not be suitable for developing densely packed cell aggregates which maintain their structural integrity. A laminated three-dimensional electrode well design has been reported [27, 28] for characterising the DEP behaviour of cells during the influence of different drugs. This electrode design could conceivably be used to create 3D cell clusters, but this has yet to be accomplished or reported.

6. 5 Conclusions

The DEP chamber used in these experiments consisted of a very simple geometry, namely that of a capacitor formed by two parallel glass slides of 220 μm separation, each coated with conducting indium tin oxide (ITO). The ITO coatings were ~ 110 nm thick, and thus transparent. The uniform electric field that would otherwise be produced between the two electrodes was disrupted by 100 holes machined into and

through the top ITO coating. Each hole was of 200 μm diameter and spaced 600 μm apart as a 10x10 array. The footprint of this array is compatible with that of a 1536 microtitre plate, and thus amenable to optical interrogation using automated plate-reading equipment. This was an important consideration because of our long-term objective to use fluorescent nanosensors to monitor cell physiological activities in real-time. The decision to machine holes of roughly the same diameter as the electrode separation ($\sim 220\ \mu\text{m}$) was aided by theoretical modeling of the electric field distortion created by their presence in one of the electrode planes. The negative DEP forces generated by this field non-uniformity was found to be sufficiently strong to condense suspensions of BETA-TC-6 and INS-1 cells into three-dimensional cell constructs of roughly the same size and cell density as the pancreatic structures, known as islet of Langerhans, that regulate insulin levels in the blood. These constructs formed under the upper slide, where the ITO holes had been machined away, and protruded down into the perfusate. Furthermore, with the DEP force maintained, these three-dimensional multicell constructs were found to be robust enough to withstand mechanical shock and fluid flow forces. This could permit their encapsulation using a gel forming solution. Another important finding was that fluorescent PEBBLE nanosensors, to be used as non-intrusive, real-time, probes of extracellular key biological species, could readily be incorporated into these artificial cell constructs.

The simple electrode geometry described here was also found to permit controlled manipulation of the cells by both positive and negative DEP, and the ability to achieve this was aided by acquisition of the dielectric properties of the cells, in terms of their membrane capacitance and conductance, by means of electrorotation measurements.

Taken together, the results of this and the previous study [25] provide a new methodology for addressing questions related to cell-cell communication, vesicle fusion and insulin release. The DEP formation of pseudo-islets of Langerhans allows the

exploration of the nature and time scale of junctional complex formation, particularly gap junctions, and their role in islet activity coordination. The ability to co-localize the PEBBLEs within the cell aggregates also advances a novel method to observe changes in the extracellular activity of metabolites or ions during physiological responses.

Localization of fluorescein conjugated nanoparticles was carried using a quadrupole electrode design. Fluorescein is pH sensitive and hence enabling the detection of pH changes in the extracellular space.

6.6 References

- 1) Stock, A.U. and Vacanti, P.J., 'TISSUE ENGINEERING: Current State and Prospects', *Annu. Rev. Med.*, 2001, 52, pp. 443–51.
- 2) Spector, M., 'Biomaterials-based tissue engineering and regenerative medicine solutions to musculoskeletal problems', *Swiss Medical Weekly* 2006, 136, pp. 293–301
- 3) Cen, L., Liu, W., Cui, L., Zhang, W., Cao, Y., 'Collagen tissue engineering: development of novel biomaterials and applications' *Pediatr Res.*, 2008, 63, pp. 492-496
- 4) Khademhosseini, A., Langer, R., Borenstein, J., and Vacanti, P.J., 'Microscale technologies for tissue engineering and biology', *P.N.A.S.*, 2006, 103, pp. 2480–2487
- 5) Bertram, R., Previte, J., Sherman, A., Kinard, T.A., and Satin, L.S., 'The phantom burster model for pancreatic beta-cells', *Biophys. J.*, 2000, 79, pp. 2880-2892
- 6) Bertram, R., and Sherman, A.: 'Dynamic complexity and temporal plasticity in pancreatic β -cells', *J. Biosci.*, 2000, 25, pp. 197-209
- 7) Balda, M. S., and Matter, K., 'Epithelial cell adhesion and the regulation of gene expression', *Trends Cell Biol.*, 2003, 13, pp.310–318
- 8) Zamir, E., Katz, B.Z., Aota, S., Yamada, K.M., Geiger, B., and Kam, Z., 'Molecular diversity of cell-matrix adhesions' *J. Cell. Sci.*, 1999, 112 (11), 1655-1669
- 9) Mueller-Klieser, W., 'Three-dimensional cell cultures: from molecular mechanisms to clinical applications', *Am. J. Physiol*, 1997, 273 (4), pp.C1109-C1123
- 10) Weaver, V.M., Lelievre, S., Lakins, J.N., Chrenek, M.A., Jones, J.C.R., Giancotti, F., Werb, Z., and Bissell, M.J.: 'Beta 4 integrin-dependent formation of polarized three-dimensional architecture confers resistance to apoptosis in normal and malignant mammary epithelium', *Cancer Cell*, 2002, 2 (3), pp.205-216
- 11) Uroukov, I.S., Ma, M., Bull, L., and Purcell, W.M., 'Electrophysiological measurements in three-dimensional in vivo-mimetic organotypic cell cultures: Preliminary studies with hen embryo brain spheroids', *Neurosci. Lett.*, 2006, 404, pp.33-38
- 12) Willerth, M.S., Sakiyama-Elbert, E.S., 'Approaches to neural tissue engineering using scaffolds for drug delivery', *Advanced Drug Delivery Reviews*, 2007, 59, pp. 325-338
- 13) Cen, L., Liu, W., Cui L., Zhang, W., Cao, Y., 'Collagen tissue engineering: development of novel biomaterials and applications' *Pediatr Res.*, 2008, 63, pp. 492-496
- 14) Drury, L.J., Mooney, J.D., 'Hydrogels for tissue engineering: scaffold design variables and applications' *Biomaterials*, 2003, 24, pp. 4337–4351

- 15) Sebastian, A., Venkatesh, G.A. and Markx, G. H. 'Tissue engineering with electric fields: Investigation of the shape of mammalian cell aggregates formed at interdigitated oppositely castellated electrodes', *Electrophoresis* 2007, 28, pp. 3821–3828
- 16) Porterfield, D.M., Corkey, R.F., Sanger, R.H., Tornheim, K., Smith, P.J.S., and Corkey, B.E., 'Oxygen consumption oscillates in single clonal pancreatic β -cells (HIT)', *Diabetes*, 2000, 49, pp.1511-1516
- 17) Jung, S.K., Trimarchi, J.R., Sanger, R.H., and Smith, P.J.S., 'Development and application of a self-referencing glucose microsensor for the measurement of glucose consumption by pancreatic β -cells', *Anal. Chem.*, 2001, 73, pp.3759-3767
- 18) Smith, P.J.S. and Trimarchi, J.R.: 'Noninvasive measurement of hydrogen and potassium ion flux from single cells and epithelial structures', *Am. J. Physiol.*, 2001, 280, pp.C1-C11
- 19) Fatoyinbo, H.O., Hoettges, K.F., Hughes, M.P., 'Rapid-on-chip determination of dielectric properties of biological cells using imaging techniques in a dielectrophoresis dot microsystem', *Electrophoresis*, 2008, 29, pp. 3–10
- 20) Burt, J.P.H., Goater, A.D., Menachery, A., Pethig, R., and Rizvi, N.H., 'Development of microtitre plates for electrokinetic assays', *J. Micromech. Microeng.*, 2007, 17, pp. 250-257
- 21) Farfari, S., Schultz, V., Corkey, B.E., and Prentki, M.: 'Glucose-regulated anaplerosis and cataplerosis in pancreatic β -cells', *Diabetes* 2000, 49, pp. 718-726
- 22) Brasuel, M., Kopelman, R., Aylott, J.W., Clark, H., Xu, H., Hoyer, M., Miller, T.J., Tjalkens, R., and Philbert, M.A., 'Production, characteristics and applications of fluorescent PEBBLE nanosensors: Potassium, oxygen, calcium and pH imaging inside live cells', *Sensors & Materials*, 2002, 14 (6), pp. 309-338
- 23) Koo, Y.L., Cao, Y., Kopelman, R., Koo, S.M., Brasuel, M., and Philbert, M.A., 'Real-time measurements of dissolved oxygen inside living cells by organically modified silicate fluorescent nanosensors', *Anal. Chem.*, 2004, 76 (9), pp. 2498-2505
- 24) Stubbs, M., Mcsheehy, R.M.J., Griffiths, J.R., Bashford, L., 'Causes and consequences of tumour acidity and implications for treatment', *Molecular Medicine Today*, 2000, 6, pp. 15–19
- 25) Pethig, R., Jakubek, L., Sanger, R.H., Heart, E., Corson, E., and P.J.S. Smith, P.J.S., 'Electrokinetic measurements of membrane capacitance and conductance for pancreatic β -cells', *IEE. Proc.-Nanobiotechnol.*, 2005, 152, pp. 189-193
- 26) Huang, Y., Hölzel, R., Pethig, R., and Wang, X.B., 'Differences in the AC electrodynamics of viable and non-viable yeast cells determined through combined dielectrophoresis and electrorotation studies', *Phys. Med. Biol.*, 1992, 37 (7), pp. 1499-1517
- 27) Hubner, Y., Hoettges, K.F., Kass, G.E.N., Ogin, S.L. and Hughes, M.P., 'Parallel measurements of drug actions on Erythrocytes by dielectrophoresis, using a three-dimensional electrode design', *IEE Proc.-Nanobiotechnol.*, 2005, 152, pp. 150-154

28) Hoettges, K. F., Hubner, Y., Broche, L. M., Ogin, S. L., Kass, G.E.N., and Hughes, M.P, 'Dielectrophoresis-Activated Multiwell Plate for Label-Free High-Throughput Drug Assessment', *Anal. Chem.*, 2008, 80, pp. 2063-2068

Chapter 7

Conclusions and Future Work

7.1 Conclusions

The work in this thesis is based around the theme of Lab-on-a-chip electrokinetic systems. Unlike conventional bio-analytical instruments, the reduction in size of analysis tools helps us approach biological particles from a micro perspective which in turn provides a deeper insight into cellular processes. The reduction in size also makes these devices highly portable, efficient in terms of speed of operation and the reduced costs of reagent volumes required, and often more affordable as a result of using the mass production methods developed by the microelectronics industry.

The main objectives of this thesis were to develop efficient DEP processes for utilization in the biological realm. The work presented here was mainly focused on the optimization of DEP devices and methods for cell separation and aggregation. This included the refinement and development of integrated microfluidic and micro electrode technologies. The refinement and optimization of the various methods described in the chapters was carried out using a finite element simulation tool. The simulations were carried out to better understand the complex electrical and fluidic forces encountering the cells, in order to manipulate them in a precise manner.

In chapter 2, the relevant theory of dielectrophoresis, electrorotation, fluid dynamics and other AC electrokinetic phenomena were outlined, together with a brief discussion of the finite element method simulation process along with methods of enhancing its accuracy.

In chapter 3 the critical electrical parameters that need to be followed to prevent electroporation and cell bursting, were discussed. By understanding these parameters DEP experiments can be carried out with minimal cell destruction. The application of strong electric fields can result in structural changes of the cell membrane which in turn leads to increased permeability.

In chapter 4, DEP separation of the Small cell lung cancer (SCLC) variants was achieved based on their phenotypic differences. For the SCLC cells it was observed that the two different phenotypes exhibited very subtle DEP differences from each other. The subtle differences were attributed to changes in membrane capacitance caused by membrane texturing. This observation was validated with electron micrograph images obtained of the two cell types. Because of subtle differences, separation of these two phenotypes had to be carried out at very low flow rates (50nl/sec) and at frequencies very close to the DEP cross-over-frequency. The voltage applied was kept to a minimum to lessen electric field stresses.

In chapter 5, a two-wire DEP based tweezers was developed to isolate and spatially manipulate individual target cells. The target cells were cells over expressing a protein tagged to the green fluorescent protein (GFP). Simulations were carried out to optimize the geometric design parameters. This particular design allows for selective isolation of single cells and the separation of transiently transfected cells.

In chapter 6, three-dimensional cell aggregations were carried out using the quadrupole electrode geometry and 3D electrode geometry. The 3D electrode geometry was found to permit controlled manipulation of the cells using negative DEP. The cell constructs were created in order to better understand the effects of cell-cell interactions and intercellular transport events in three dimensional cell aggregations. The biological test system consisted of BETA-TC-6, INS-1 insulin secreting cells and schwannoma

tumour cells. The three-dimensional cell constructs were roughly the same size and cell density as the pancreatic structures known as islet of Langerhans that regulate insulin levels in the blood. The ability to co-localize nano-ionic sensors within the cell aggregates to observe changes in the physiological responses was demonstrated.

7.2 Future Work

From a theoretical perspective, a future research objective would be to better understand the electrostatic interplay between polarized particles. Another interesting topic for investigation would be the mechanism behind the instability causing the spinning of cells around the DEP cross-over-frequency, observed around the electrode edges in a stationary field.

From the work in chapter 3 and previous studies, it is well understood that electroporation can sometimes lead to irreversible cell destruction. However, this process can also be controlled using millisecond, microsecond and nanosecond pulses, such that it is reversible. This method can then be used to transport substances such as DNA and drugs into the cells, while ensuring cell viability. In the future, understanding gained from the study in this thesis can be used to help optimise the process of electroporation by effectively combining the ability to accurately position cells using dielectrophoresis and the effect of pulses and other arbitrary waveforms to help induce effective reversible and transient membrane perforations.

The applications of electroporation (EP) can be applied to many areas of biological research. The understanding gained from *in vitro* testing can be applied to *in vivo* applications such as electrically assisted chemotherapy. This method can also be used to effectively introduce foreign genetic material to help microbiologists better understand cellular process and create cell hybrids. When there are two contacting cells,

and under specific conditions, delivery of electric pulses can lead to membrane fusion. Fusion results in the union of both cells within a single enclosed membrane and this can then be used to produce genetic hybrids for producing antibodies.

In chapter 4, separation of a volume of 200 μ l of mammalian cells took approximately 1 hour, which is a considerable amount of time for them to be suspended in the DEP media. In order to increase throughput, a couple of possibilities are mentioned below: In the work described in this thesis we have employed a single frequency sinusoidal voltage to achieve DEP phenotypic separation. For subtly different cell types where the cross-over frequencies of the two cell types are very close, the commonly used single frequency method is not extremely efficient. Dual or multiple frequency applications might be able to provide increased flexibility and therefore enhance separation capability of the device. Separation of narrowly different cell types could also benefit from having electrodes patterned on the top and bottom of the fluidic chamber, in order to achieve higher cell capturing.

The work carried out in chapter 5 will benefit from the development of a setup which will combine DEP tweezers with a micro-suction apparatus. In the current setup it is not feasible to easily extract the cell from the dish used to perform DEP. The introduction of a suction apparatus will allow for the dielectrophoretically trapped cells to be transferred into a dish containing physiological media. This tweezers design can also be explored for the purpose of single cell electroporation.

One of issues relating to the cell clustering work described in chapter 6 was the extraction of the cell constructs from the chamber after aggregation. In the future, alternative electrode designs and cell encapsulation gels should be explored to facilitate easy extraction of the cell clusters. The encapsulation gels can be diversified to include physiological materials such a collagen and other biologically inert materials such as polyethylene glycol hydrogels.

List of publications

Journal

- 1) Menachery, A., and Pethig, R., 'Controlling cell destruction using dielectrophoretic forces', IEE Proceedings Nanobiotechnology, 2005, 152, pp. 145-149
- 2) Burt, J.P.H., Goater, A.D., Menachery, A., Pethig, R., and Rizvi, N.H. 'Development of microtitre plates for electrokinetic assays', J. Micromech. Microeng. 2007, 17, pp. 250-257
- 3) Pethig, R., Menachery, A., Heart, E., Sanger, R.H., and Smith, P.J.S., 'Dielectrophoretic assembly of insulinoma cells and fluorescent nanosensors into three dimensional 'pseudo-islet' constructs', IEE Proceedings Nanobiotechnology, 2008, 2, pp. 31 - 38
- 4) (In preparation) Menachery, A., Messerli, S.M., Messerli, M., Pethig, R., and Smith, P. J. S., 'Design and Experimental considerations for the isolation of single target cells using dielectrophoretic tweezers'

Conference

- 1) Goater, A.D., Burt, J.P.H., Morris, D.J., Menachery, A., Matthews D.R., and Summers, H.D., 'Laser micromachining of optical biochips', Proceedings of SPIE 6459, 2007
- 2) Morris, D.J. Goater, A.D., Menachery, A., Burt, J.P.H., Matthews, D.R., Summers, H.D., Pope, I., Vojnovic, B., Njoh, K.L., Chappell, S., Errington, R., and Smith, P.J., 'Development of an optical biochip for the analysis of cell environment sensitivity', Proceedings of SPIE 6441, 2007
- 3) Summers, H.D., Matthews, D.R., Errington, R.J., Njoh, K.L., and Smith, P.J., Goater, A.D., Burt, J.P.H., Rizvi, N.H., Menachery, A., and Morris, D.J., 'Semiconductor light-emitting devices with in-built bioreaction chambers', Proceedings of SPIE 6441, 2007
- 4) Menachery, A., Chappell, S., Errington, R.J., Morris, D., Smith, P.J., Wiltshire, M., Furon, E., Burt, J.P.H., 'Dielectrophoretic characterization and separation of metastatic variants of small cell lung cancer cells', NSTI Nanotechnology Proceedings, 2008
- 5) Menachery, A., Messerli, S.M., Huyett, P., Lewis, R., Pethig, R., Smith, P.J.S., 'Dielectrophoresis as a method of isolating single cells based on their fluorescence' Gordon Conference on Bioelectrochemistry (Poster)
- 6) Messerli, S.M., Graham, D.M., Messerli, M.A., Menachery, A., Pethig, R., and Smith, P.J.S., 'Measurement of Hydrogen Ion Activity in The Intercellular Space of Schwannoma Tumors', Biophysical Society, 2009 (Poster)